Helicopter Hover CFD Simulations: An Investigation of Various Far-Field Boundary and Initial Conditions via DLR's Legacy Block-Structured FLOWer CFD Solver

Alexios Nicolas PHILIPPOU

2404257

Submitted in fulfilment of the requirements for the Degree of

MEng Mechanical Engineering with Aeronautics

University of Glasgow

2024

Abstract

The DLR FLOWer block-structured CFD solver which solves the Reynolds Averaged Navier-Strokes equations is employed in this paper in order to undergo an investigation of the effect of different far field boundary conditions and initial conditions of the HART II helicopter rotor in hover. A dual time stepping scheme is employed in the transient simulations to observe flow field evolution from an initial state. Parametric studies on the density residual convergence tolerance criteria and potential turbulence models are also explored to ensure an optimal compromise between accuracy and computational efficiency which were considered important due to the short period of the study and the high computational demand of hover simulations. It was concluded that a model described in recent literature tested on different domains of varying mesh densities and downstream far field boundary locations is more robust and can aid helicopter rotor hover simulations converge at a faster rate. This means that domains with shorter far field distances from the source of disturbance can be used with this new boundary condition, to decrease computational costs and therefore time.

Acknowledgements

I would like to express my deepest gratitude to Gunther Wilke, my project supervisor, for their guidance and expert advice throughout this research project. Their encouragement and insights have been pivotal to the project's success. I additionally extend my thanks to my fellow colleagues at the Braunschweig DLR site, whom also made me feel a part of the team there. Lastly, this study would not have been the same without the unwavering love, understanding and encouragement from my parents, Mary and Nicolas Philippou and my sister, Dorothy Philippou. Their support has been my cornerstone in this challenging yet rewarding journey.

Contents

1 Introduction

Stationary hover is one of the most crucial flight conditions for a helicopter. It enables them to undergo a range of missions that require precise control, and the ability to operate in diverse environments through this flight condition. In this regard, this flight condition makes helicopters versatile vehicles which mark them as essential assets for a multitude of industries including aviation, defence emergency, services, and more. Many researchers, such as those at the German Aerosapce Center (DLR), have developed CFD solvers to accurately simulate the air flow around helicopters in this flight condition amongst others to aid in the understanding of the complex flow phenomena which occur. One of their solvers, FLOWer, is a widely utilized block-structured CFD solver for rotor applications and is the solver that is to be used in this research. Specifically, this investigation aims to address the limitations associated with the current far-field conditions that are implemented in the FLOWer source code, such as the source-sink boundary condition and introduce and test new models recorded in recent literature. The investigation hopes to shed light into the robustness of each model, and draw conclusions regarding which models can be employed on smaller domains where the far field locations are closer to the source of disturbance. The smaller the domain that can be used, the lower the computational cost and therefore time needed to converge solutions.

The high fidelity CFD simulations of hover is potentially the most challenging flight regime of a helicopter rotor but also the most attractive as this is where the major advantages of rotor vehicles emerge. It is also especially important to study, as it one of the most power consuming flight regime of helicopters. This is a challenging regime to simulate due to a two main reasons. Firstly, due to the needs of fine grids particularly in the wake region in order to preserve the trailing vorticies and therefore an accurate representation of the blade-vortex interactions. In comparison to forward flight, where flow is oncoming on the domain, these blade-vortex interactions are less pronounced. As such, there is vivid complexity within the flowfield around a helicopter rotor which is due to the strong vortical effects of the previous blade's rotation. These vorticies that trail off the blade pass closely to the oncoming blade, causing an adverse source of downwash of varying strength along the blade's span and in turn change the lift and torque experienced. Additionally to the effects on the blade span, these vortical structures age into the downwash of the rotor, causing turbulent mixing of the flow as vorticies join together and diffuse with time, leading them to have a strong influence on the contraction of the wake. Acknowledging that capturing these effects are fundamental to accurately predict a physical representation of a helicopter hover flow field and therefore its performance, this study focuses upon the second cause that can have adverse effects on the performance of the rotor, the boundary condition.

The boundary condition has the important task to deal with oncoming flow which attempts to escape the domain. This boundary condition needs to be robust enough to accurately resolve and flush out these vortical structures that come into contact with it from the downwash of the rotor.

There is a lot of computational effort required to expel the initial flow artifacts such as the initial chaotic starting vortex when initialized with quiescent flow out of the domain's edges before reaching a steady state, and as such having a boundary condition which can manage to keep a physical representation of the flow is preferable. This is particularly important, as the flow field that develops on the boundary, physical or not, can have adverse effects on the flow field that develops around the blade. Some nonphysical hover-state phenomena that will be seen include a blocking effect at the downstream boundary, which in turn cause the rotor to experience greater lift and to seem as if it is in-ground effect. The initial condition can also have an effect on the time taken to reach the statistically steady state of the simulation, as some models explored in this paper can aid in reducing the magnitude of initial starting vortex as well as the time taken to flush it out of the domain.

Three main boundary conditions and two initial conditions are tested with different computational domains of varying far field boundary location distances amongst other parameters like mesh density. The three main conditions with their own characteristics are the Froude source-sink [9], the far field boundary and initial condition based on characteristic flow, and finally Jia's modified Spalart model based on a jet function [10]. Whilst offering advancements over classical far field boundary conditions, the Froude based source-sink boundary condition has associated constraints that otherwise hinder the accuracy of rotor simulations. Particularly, one example being the assumption of the contraction of the rotor wake by the square root of 2 which introduces challenges for capturing realistic flow. To overcome these limitations, this research suggests integration of different far field boundary and initial conditions which have been documented in scientific literature in recent years such as the model proposed by Jia, all of which are covered in the following literature review. All of the models to be investigated have a common goal to reduce the computational time to convergence of rotor hover simulations overall increasing the computational efficiency. This can be done through introducing models that approximate the wake of the flow as initial and boundary conditions such that the computational domain as a whole can potentially decrease in size. Throughout these studies, the state-of-the art of time depended Navier-Strokes simulations of rotors in hover have been considered, such as the study done by Chaderjian [4] which emphasises the lessons learned over the past decade on the effects of high-order spatial accuracy and grid resolution in predicting accurate performance.

2 Literature review

In rotor CFD simulations, there are two parts to consider when referring to the boundary condition. One part is the physical boundary condition, and the other is the numerical boundary condition. Physical boundary conditions are related to the actual physical behaviours and properties of the flow at the boundaries of the domain, and attempt to replicate the physical scenario occurring at this location. Numerical boundary conditions on the other hand are related to the computational aspects of solving the fluid flow equations. They are mathematical formulations implemented to ensure numerical accuracy and stability of the simulations. Some examples of these are the Dirichlet, Newumann, and Robin Boundary conditions. In the case of this investigation and of the associated theory below, the focus is upon only the physical boundary condition.

2.1 General rotor simulations farfield boundary and initial conditions

To accurately assess the flow field around a helicopter and the rotor loads in a hovering state via CFD simulations, it is essential to investigate the conditions applied in the far-field, ensuring that they accurately resemble their physical counterparts. Particularly, the far-field boundary conditions play a vital role, as they directly attempt to model how the flow is expected to act when it interacts with this area of the computational domain. Similarly the initial condition is of importance as it describes the flow-field at the beginning of the simulation which is hoped to give a close solution to the final one. This chapter covers two key boundary and initial conditions that have been implemented and tested over years and could therefore be described as 'traditional' far field conditions. One is the classical far-field condition based off of characteristic flow, and the other is the source-sink model, based off of simple momentum theory.

2.1.1 Farfield Boundary and Initial Condition

Traditional far-field conditions have their focus on creating a theoretically unbounded computational domain, making sure that the environment being simulated accurately mimics a flow field that is infinite. Generally, the procedure of imposing this type of boundary consists of specifying free stream conditions such as density, velocity, and pressure, specifically for the boundary. This kind of approach allows the rotor's down wash and surrounding interaction with the flow field to be modelled into an approximate open-air environment. It is important to note that for this far-field boundary condition to work properly, it must be allocated far enough from the source of disturbance, in a region where the flow is meant to resemble free stream conditions. This distance that the boundary location must be located varies for different simulation types. For example for a fixed airfoil, a study done by Meghana Athadkar [2] concluded that the far field boundary condition must be placed at least 10 chords upstream and 15 chords downstream of the airfoil to yield reliable results.

2.1.2 Froude source-sink

On the other hand for rotor simulations, a popular way to prescribe the inflow and outflow at far-field boundaries is the source-sink boundary condition that was initially proposed by Froude in 1889 [9]. Froude invented the earliest concept of the actuator disc, which consisted of a permeable disk with a uniform pressure increase across it's top and bottom surfaces. This disk represents a rotor or propeller with an infinite rotational speed within a parallel uniform flow. In terms of momentum theory, this is typically called the one-dimensional theory since it includes the momentum balance in only a single direction along the axis of rotation of the rotor. This model consisted of a potential sink located at the center of the rotor hub to attract flow from the entire computational domain which is initialized with quiescent flow, as first proposed by Srinivasan et. al [20], from all of the far-field boundaries apart from the outflow boundary. In other words, the inflow is pointing towards the point sink from almost all of the boundaries. Figure 1 clearly illustrates a 2D version of this proposed model. Using 1D momentum theory and the source-sink model within the domain, the rotor inflow velocity W_{in} can be found with the following equation:

$$W_{in} = -\frac{V_{tip}}{4}\sqrt{\frac{C_T}{2}}\left(\frac{R}{d}\right)^2 \tag{1}$$

With V_{tip} being the rotor tip speed, C_T is the coefficient of thrust, R is the rotor radius, and $d = x^2 + y^2 + z^2$. This inflow velocity is determined by the outflow velocity, as the net flow in and out of the domain must be zero. The outflow velocity, derived from the 1D momentum theory can be specified as:

$$W_{out} = -2V_{tip}\sqrt{\frac{C_T}{2}} \tag{2}$$

The coefficient of thrust is:

$$C_T = \frac{T}{(1/2)\,\rho\,\pi\,R^2\,V_{tip}^2} \tag{3}$$

For the outflow boundary condition, density and the three velocity components are extrapolated from the interior of the domain, while pressure is fixed to the freestream value. This results in the mass outflow compensating for the mass inflow. As alluded from the theory, the downstream radius of the outflow is given by $R/\sqrt{2}$. On the contrary, the inflow boundary condition has its prescribed density fixed to the freestream value, and the three velocity components are evaluated by equation (1). Pressure at the inflow boundary can be found via the isentropic relation between freestream and boundary flow field. The advantage of this boundary condition is to reduce the

effect of the finite far field distance within the computational domain. But if the grid sizes are sufficiently large the differences between computations with the Froude condition or without are small.

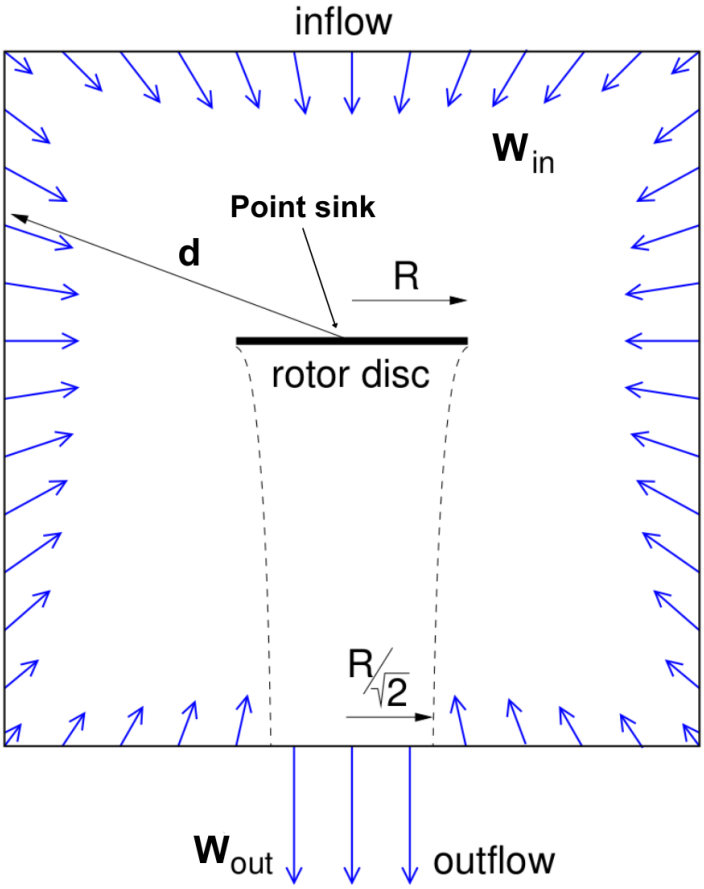

Figure 1: Froude's Source-Sink Model

2.2 Contemporary far-field boundary and initial conditions

Ever since the rise of the Froude and the traditional Fairfield boundary conditions, new models have been recorded in recent literature which aim to be more computatinally efficient. Additionally, these models aim to bring the farfield boundaries closer to the source of disturbance, i.e. the rotor, such that a much smaller computational domain can still converge and simulate accurate representations of what would be expected in the physical world. This chapter introduces these newer models, talks about their history, and explains the physics behind them.

2.2.1 Wang's vortex tube model

In order to predict the aerodynamic characteristics of a helicopter rotor in vertical descent, Wang [23] proposed an analytical approach based on a truncated vortex tube model for the rotor's wake for use in the vertical flight regime. This regime spans from the hovering state to the vortex-ring state to the turbulent windmill state. This is the first step beyond the disk momentum theory, incorporating some sense of the rotor wake as a vortical system [13]. The key concept from his idea was that rather having the conservation of circulation in an ideal flow, he assumed a linear decay of circulation of trailing vortices in the real wake. He additionally assumed that the transport velocity of the trailing vortices to be directly proportional to the distance required for the circulation to decay to zero. A large circulating flow is generated by this truncated vortex tube which enters through the rotor disk at the top of the domain and exits through the bottom. In his paper he discusses the truncated vortex tube's underlying physics and demonstrates their equivalence to momentum theory. From this model, experimental time-wise mean induced velocities averaged over the rotor disk area were successfully reproduced over a wide range of decent rates, with the region of wake breakdown associated with the turbulent wake flow vortex ring condition included.

The reason as to why the vortex tube was taken to be truncated was due to one of Wang's assumptions. He decided, based on physical observation, that the wake does not continue indefinitely downstream, but instead truncated itself at a certain distance, declared H. In equation (4), you can clearly see how circulation linearly decreases to zero along the tube in his model. The parameter z is the axial distance normal to the rotor disc area, Figure 2 aids in the comprehension of the reference frame. The vortex strength Γ can also be related to the thrust coefficient as follows:

$$\Gamma(z) = \Gamma_0 \left(1 - \frac{z}{H}\right) = -2\frac{V_{i,hov}}{\bar{V}_t}\left(1 - \frac{z}{H}\right) \tag{4}$$

where $V_{i,hov} = -V_{tip}\sqrt{C_T/2}$ and $\bar{V}_t$ is the normalized speed at which the vorticity is transported down the wake. The derivation of the relation of vortex strength to the hovering induced velocity can be found in the Appendix of Perry [13].

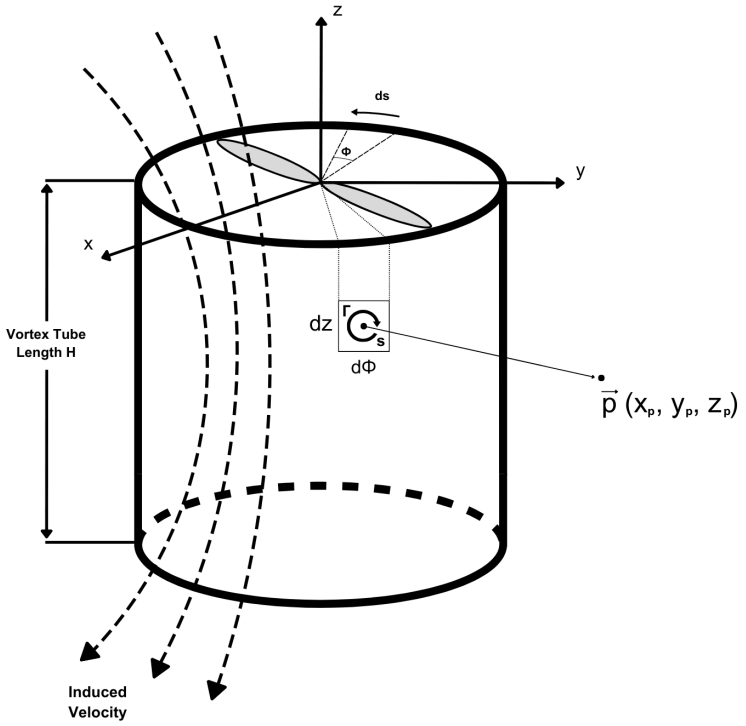

Figure 2: Wang's schematic of the truncated Vortex Tube Model

In more detail, the rotor wake in the paper was represented truncated vortex tube of constant radius R and of continuously distributed vorticity aligned with the tube circumference with an axial spatial density. Consider an infinitesimal vortex element at a point declared $\vec{s} = (Rcos\phi, Rsin\phi, z)$ on the surface of this vortex tube. The vortex element has a strength Γ per unit length and in accordance with the Biot-Savart law the element $\Gamma d\vec{s}$ generates an infinitesimal induced velocity $d\vec{v}$ from the perspective of an observer point $\vec{p} = (x_p, y_p, z_p)$. The induced velocity at the observer point can be calculated by the summation of all the vortex element's infinitesimal induced velocities on the surface of the vortex tube($r = R$), in other words, through the integration along the axial and azimuthal directions:

$$\vec{v}(p) = \iint \frac{\Gamma dz}{4\pi} \frac{d\vec{s} \times \vec{d}}{|\vec{d}|^3} \tag{5}$$

Due to the fact that the induced flow calculated by (5) is axially symmetric, the vector can be decomposed into axial and radial velocity components. By performing the cross product present in equation with the distance $\vec{d}$ from the segment of a vortex $d\vec{s}$ to the observer point derived from Figure 2 as:

$$\vec{d} = \vec{p} - \vec{s} \quad \text{and} \quad d\vec{s} = -R\sin\phi d\phi\, i + R\cos\phi d\phi\, j$$

And by normalizing all coordinates by the rotor disk radius R:

$$\bar{x}_p = \frac{x_p}{R} \quad \bar{z}_p = \frac{z_p}{R} \quad \bar{x} = \frac{x}{R} \quad \bar{z} = \frac{z}{R}$$

The axial and radial velocity components due to the vortex tube of linearly decreasing circulation from (4) at the observer point, normalized by the hovering induced velocity, can be written as:

$$\bar{v}_r(p) = \int_0^{\bar{H}} \int_0^{2\pi} \frac{1}{2\pi \bar{V}_t} \frac{\left(1 - \frac{\bar{z}}{\bar{H}}\right)\left[(\bar{z}_p - \bar{z})\cos\phi\right]}{\left[\bar{x}_p^2 + 1 - 2\bar{x}_p \cos\phi + (\bar{z}_p - \bar{z})^2\right]^{1.5}} \, d\phi \, d\bar{z} \tag{6}$$

$$\bar{v}_z(p) = \int_0^{\bar{H}} \int_0^{2\pi} \frac{1}{2\pi \bar{V}_t} \frac{\left(1 - \frac{\bar{z}}{\bar{H}}\right)\left[1 - \bar{x}_p \cos\phi\right]}{\left[\bar{x}_p^2 + 1 - 2\bar{x}_p \cos\phi + (\bar{z}_p - \bar{z})^2\right]^{1.5}} \, d\phi \, d\bar{z} \tag{7}$$

An additional assumption that was made for climbing and descending flight was that the length of the truncated wake was related to an overall transport velocity of filaments of vorticity down the wake, V_t. This relationship is proportional, meaning that a longer truncated tube to represent the wake correlated to a higher overall transport velocity.

$$\bar{H} = k_H \bar{V}_t \tag{8}$$

Specifically, this overall transport velocity is the summation of the rotor translational (free-stream speed) and the self-induced velocity of vorticity.

$$\bar{V}_t = \bar{V}_v + k(\bar{H})\bar{v}_i \tag{9}$$

Substituting and rearranging this relationship for the rotor upward axial velocity $\bar{V}_v$, and by substituting the self induced velocity $\bar{v}_i$ with it's equivalence derived by Wang [23] the following equation is obtained:

$$\bar{V}_v = \frac{\bar{H}}{k_H} + \frac{k_H \, k(\bar{H}) \, A'}{\bar{H}^2} \left(\sqrt{\bar{H}^2 + 1} - 1\right) \tag{10}$$

where the parameters k_H, $k(\bar{H})$, and A' are determined empirically from experimental results conducted by Wang. The optimal values for these parameters are as follows:

$$k_H = -3 \qquad A' = 1.62 \qquad k(\bar{H}) = 1 - 0.4\left[\exp -(\bar{H}/2)^2\right] \tag{11}$$

With equations (6) and (7) the induced axial and azimuthal velocity solutions for the entire flow field can be obtained. With these evaluated at the far-field domain due to a specified overall thrust, they can be implemented as the far-field boundary conditions. Additionally, if the thrust of a certain rotor is known prior to a simulation, the equations can also be used to specify an initial condition to aid in the acceleration of convergence, instead of employing the traditionally applied quiescent flow field initialization. In fact, Choi [5] concluded that using the truncated vortex tube model rather that quiescent flow as an initial condition reduces convergence time by half without loosing accuracy. A Python prototype of the model can be seen in in Figures 3 to 4.

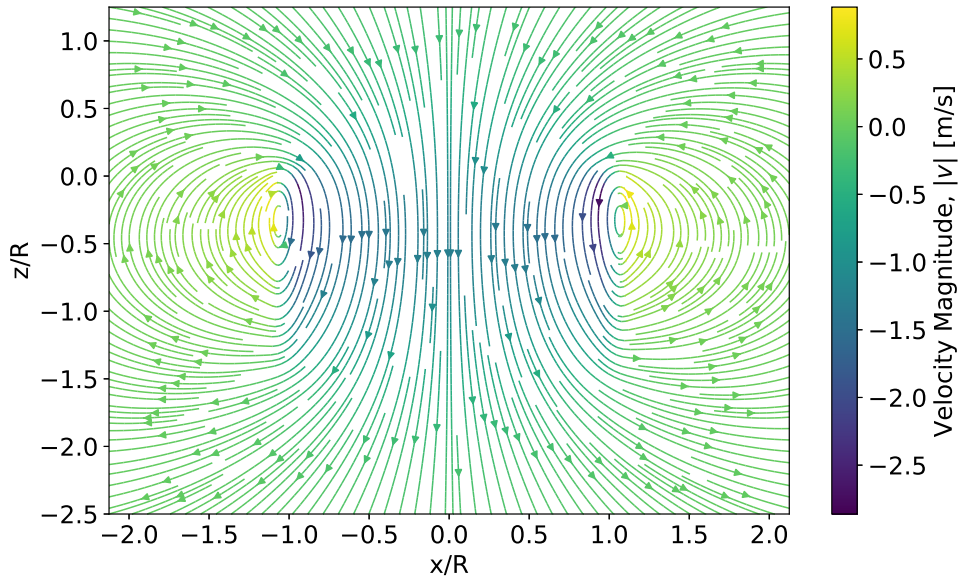

Figure 3: Python prototype of Wang Model - Velocity magnitude contour plot with streamlines

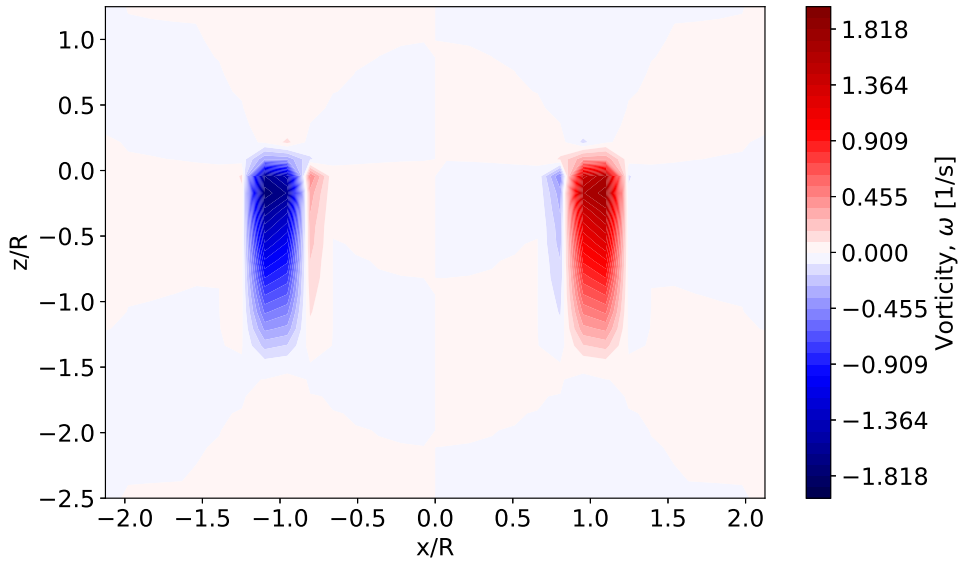

Figure 4: Python prototype of Wang Model - Vorticity contour plot

2.2.2 Jia's modified version of the Spalart model

Although the vortex tube model previously discussed seems reasonable, Jia disagreed and believed that a tube of finite length is much less potent than a model discussed by Spalart, and as such conducted an investigation. With the aims to produce a good model for the far-field flow of a helicopter simulation in hover that can be used as initial and boundary conditions, many CFD codes use the actuator-disk sink model, such that simulations costs can be reduced via reduction in transient time and computational domain size. This model, discussed by Spalart [17], leads to $1/r^2$ decay of velocities down the wake, but simulations do not support this decay nor the direction of flow outside the wake. About a decade later, Spalart introduced a new analytical model [19] which included a static function implied by Stewart [21]. This model is different to the classical actuator-disk derived model as the velocities decay with $1/r$ and are directed in the opposite direction of thrust everywhere.

This new analytical model still had some issues. To troubleshoot them, Jia decided to modify this new proposed model by Spalart as it was prone to a singularity at the origin at $x = y = z = 0$ as the original model was not intdented for use at small r, and had some issues in the calculations of the velocities in spherical components as $\theta \to \pi$. The modifications included a change in the mathematical formula of the empirical jet function, which removed the issue yet maintained the overall shape of the function, and an addition of a constant to the denominators of the spherical velocity component equations. The details of these modifications can be found in Jia's paper [10]. The three Cartesian components of velocity within the domain are given by:

$$u_x = u_r \frac{x}{\sqrt{x^2+y^2+z^2}} - u_\theta \frac{z}{\sqrt{x^2+y^2+z^2}} \frac{x}{\sqrt{x^2+y^2}} \tag{12}$$

$$u_y = u_r \frac{y}{\sqrt{x^2+y^2+z^2}} - u_\theta \frac{z}{\sqrt{x^2+y^2+z^2}} \frac{y}{\sqrt{x^2+y^2}} \tag{13}$$

$$u_z = u_r \frac{z}{\sqrt{x^2+y^2+z^2}} + u_\theta \frac{\sqrt{x^2+y^2}}{\sqrt{x^2+y^2+z^2}} \tag{14}$$

Where u_r and u_θ are the velocities in spherical components:

$$u_r = \frac{-A}{r_m}\sqrt{\frac{T}{\rho}}\left[f_m(\theta_m) + \tan\left(\frac{\theta_m}{2}\right)\left.\frac{\mathrm{d}\theta_m}{\mathrm{d}\theta}\right|_{\theta_m}\right] \tag{15}$$

$$u_\theta = \frac{A}{r_m}\sqrt{\frac{T}{\rho}}\tan\left(\frac{\theta_m}{2}\right) f_m(\theta_m) \tag{16}$$

Here, $r_m = r + 3R$ and represents the addition of the constant for the removal of the singularity which is subject to tweaking. Also, $A = 0.027$ is an empirical constant. Note that:

$$r = \sqrt{x^2 + y^2 + z^2} \tag{17}$$

The modified empirical jet function, f_m, is given as:

$$f_m(\theta) = 1 - exp\left(-\left[\frac{\cos\theta/2}{\sigma/2}\right]^2\right) \quad \text{with} \quad \sigma = 0.135 \tag{18}$$

Finally the modified value of θ, denoted θ_m, is given by:

$$\theta_m = \arccos\left(\frac{z}{\sqrt{max(0, x^2 + y^2 - R^2)} + z^2}\right) \tag{19}$$

Through this investigation, by employing these equations as boundary and initial conditions as a way to inject an approximate representation of the wake underneath a rotor, some interesting conclusions were made. Compared to the freestream initial condition, it was found that the new far-field model based initial condition can rapidly establish low-speed rotor induced flow and reach convergence of thrust and torque to a statistically steady state at a faster rate. This new far-field model based initial condition also effectively flushes out the initial chaotic starting vortex that is inevitable when beginning simulations with freestream conditions and in turn prevents the oscillations of thrust that occur due to the blade-vortex interaction. As a far-field condition, it was concluded that there is no evident decrease in convergence time of torque and thrust, but the wake can develop much more rapidly compared to the freestream boundary condition due to the specified velocity at the boundary. Overall, it was concluded that this boundary condition and initial condition may be beneficial to simulations of rotor in hover. A Python prototype of this model can be seen in Figure 5.

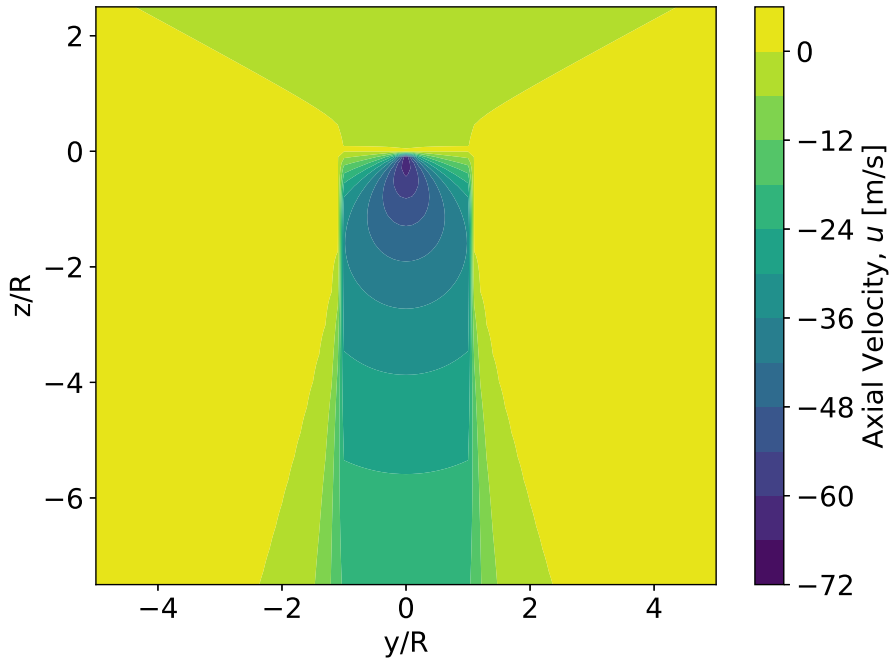

(a) Axial Velocity Plot

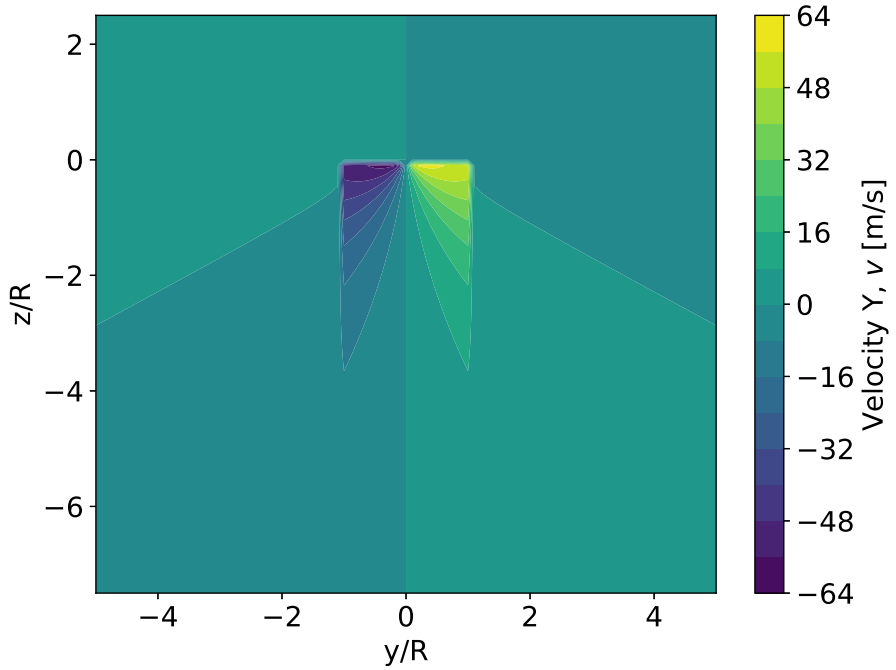

(b) Y Velocity Plot

Figure 5: Python Prototype of Jia model flow field initialisation view

3 Numerical method

In this chapter, details of the numerical and experiemntal methods employed will be discussed in detail. This includes details of FLOWer CFD solver, the rotor choice for the investigations, the grid system choice, and finally the fundamental solver settings used.

3.1 Details of FLOWer CFD environment

As a general introduction to this section, the block-structured flow solver FLOWer, developed by DLR, solves the compressible 3-D Reynolds averaged Navier-Stokes equations for rigid bodies in arbitrary motion and is the numerical code used in this investigation. A finite-volume method with second order upwind or central space discretization is used to solve the equations. Cell centered and cell vertex formulations are available for space discretization, but cell centered are considered for these studies. Cell centered metric is well suited for this investigation, as it provides high robustness and is well suited for parallel applications. The discrete equations are integrated directly using a backward Euler LU-SGS method [14]. To accelerate convergence for steady computations, the FLOWer code features several techniques, including local time stepping, implicit residual smoothing and multigrid acceleration. More in depth information regarding the time and space discretization are available in the following subsections. Additionally the Chimera technique is available in FLOWer, and enhances the flexibility of handling complex geometries and independently moving bodies. Various turbulence models are available, ranging from eddy viscosity to full differential Reynolds stress models. In this study of unsteady simulations, the implicit dual time stepping technique is employed for both monocoque and chimera meshes.

For time accurate computations the implicit dual time stepping method is employed. It could be argued that steady simulation type would be preferable, as convergence could be reached at a faster rate. In reality, hover is a state in which there is a constant transient nature to the flow field, where trailing vorticies are inconsistently interacting with the rotating blade and ageing tip vorticies. Due to the interest in the evolution of the flow field from its initial state from the boundary and inital conditions, transient simulations would output more physical results. As such, it was believed that the dual time stepping method would be the preferable choice of simulation type.

FLOWer is also capable of calculating flows on moving grids (translation and rotation) under steady and unsteady flow conditions. In this case, the compressible Reynolds-averaged Navier-Stokes equations are solved, transformed into a body fixed rotating reference frame. In this reference frame, the equations are formulated in terms of absolute velocities. For a hovering rotor, the periodicity of the flow field solution is used to reduce the computational domain. This means that only one quarter of the computational domain needs to be considered. This technique requires that special boundary conditions be applied at the periodic grid surfaces with which the

flow information are transferred from the rear to the front grid boundaries and vice versa. The boundary condition at the blade surface is the no-slip condition with the adiabatic wall. This boundary condition zeroes all the components of the velocity vector in the rotating frame at the body surface. In the inboard plane boundary, near the axis of rotation (hub surface), the DLR code uses the invicid solid wall condition. With this condition only the component of the velocity normal to the wall is zeroed; consequently the flow is forced to be parallel to the hub surface.

The computer used in this investigation was the CARA HPC (Computer for Advanced Research in Aerospace High Performance Computer) owned by DLR. It "has 2280 nodes and is equipped with AMD EPYC processors, each with two AMD EPYC processors and 32 computing cores, 112 nodes each with two AMD EPYC processors and 64 computing cores, and 10 nodes each with four NVIDIA A100 GPUs. The system is water-cooled and has a power consumption of up to 1.2 megawatts. The storage components are divided into 16.5 petabytes of hard disk drive (HDD) and 0.6 petabytes of solid state drive (SSD). CARA has a maximum computing power of 3.2 quadrillion operations per second." [8]

3.2 Rotor choice

The rotor chosen for this boundary and initial condition investigation is the HART II rotor. This rotor has been a main subject especially for many code validation studies [16], also associated with the German Aerospace Center (DLR). In fact, it's investigation was a project of the US Army, DLR, NASA Langley, ONERA and the German-Dutch Wind Tunnels (DNW). As such, it was believed to be a good candidate for this study. A summary of the key geometric characteristics can be found in Table 2 of [16]. It could be argued that only investigating a single rotor for this study to be insufficient to draw substantial conclusions regarding the validity of the success of the new boundary and initial condition and rotors of more elaborate design should be considered. But in fact, this study focuses upon the concept of an actuator disk and a simple rotor such as the HART II is substantial to serve as this. Also it could be argued that the entire fuselage of the helicopter should be simulated as part of the boundary condition study. This is also true to a certain extent, but can be the focus of future studies based upon this work.

The next step after deciding which rotor to simulate was to choose an appropriate angle of attack which would be suitable for the simulations to prevail. Provided internally by DLR, wind tunnel data was interpolated via a radical basis function with a substantially large regression coefficient to plot the rotor Figure of Merit (FM) polar as seen in figure 6. A large regression coefficient was chosen in this interpolation method to get a smooth plot over the entire range of θ as the original data points would not produce a smooth polar. It is important to note that in wind tunnel experiments, results are prone to wind tunnel re-circulation and blade elasticity, which can be the leading cause of these jagged polar plots. A CFD study on rigid versus elastic blades

associated with DLR [3] suggested that by modeling the elasticity results match experimental values more closely, but for this actuator-disk based study of the far field conditions, elasticity was disregarded. Additionally, an interesting study of a boxed rotor by the DLR is referenced in [27], where it was concluded that re-circulation and vibrations increase with increasing thrust in a finite test hall. When deciding the angle of attack to be used in the simulations to follow, the FM polar was studied, and it was concluded that at a θ of 9.5, there is sufficiently high thrust without any local stall. This angle would be a good compromise starting point, where flow is able to evolve at a sufficient rate to expedite the simulation to the hovering state with the associated high level of thrust, but not stall the blade. Therefore this angle of 9.5 was chosen for the simulations to follow, where the expected FM from the interpolated experimental data is 0.678.

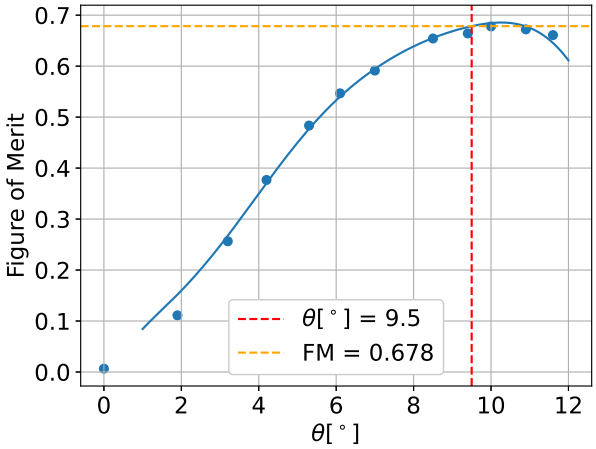

Figure 6: Figure of Merit Polar for the HARTII rotor from interpolated experimental data

3.3 Grid system choice

As with any CFD studies, it is crucial to discuss the grids used within the simulations. This fundamental element of CFD simulations can have a significant influence over the reliability and accuracy of any numerical results produced. Particularly in helicopter hover flow fields, intricate vortex dominated flow patters dictate the way of behaving of aerodynamic phenomena and as such, the choice of the computational grid becomes of great importance. All meshes discussed in this section were generated via DLR's internal meshing software, named G^3.

With the main task to implement a new boundary and initial condition to the FLOWer CFD solver, a substantial amount of the studies were performed on coarser meshes. Granted the inherently transient nature of the flow field of a helicopter in hover in conjunction with the limited time of the placement, it was decided that the New Model's concept (Jia's modified version of the Spalart model) would be best proven on the coarser meshes first, yielding results faster. When the concept was proven to work, it was then pushed onto finer meshes to produce higher fidelity results and draw more legible conclusions. A combination of both monocoque

and chimera/overset meshes were used in this study with both coarser (L2) and finer (L1) mesh versions. As a point of initial reference when attempting to create the meshes, previous studies of helicopter rotors performed within the FLOWer CFD solver were investigated. A validation study of some of DLR's simulation setups which included a helicopter rotor in hover [26], Fig.3, alluded that L2 produces good results and that L1 gets even closer to experimental values for the study of a 7A rotor. The coarsest monocoque mesh, L2, that was generated for this study closely resembles the L2 mesh of the referenced study, with a very similar mesh geometry.

The exact details of the meshes used can be found in the grid Table 1, including number of cells and downstream boundary locations. The associated snapshots of the meshes displayed on their coarsest setting, can be seen in Figures 7, 8, 9, and 10, which show the mesh isometric view, blade O-O topology cross-sectional view, blade topdown view, and blade back view accordingly for both monocoque and chimera setups. The chimera grids were generated in a similar manner, but had higher cell density compared to their monocoque counterpart. The key difference in the geometry of the monocoque and chimera grids investigated was the shape. It can be seen that the monocoque grid has a cylindrical shape with a slight curve along it's longest axis, converging near the top and bottom of the domain with it's maximum point along the rotor's rational plane. On the other hand, the chimera grid has enclosed within a more simple cylindrical shape. This was done on purpose, to see the effect of the boundary conditions on different computational domain geometries.

When designing the grids, a few key points were kept in mind. Firstly, ensuring that grid density was high in crucial regions where high gradients are expected was considered. This meant keeping the density high in regions near solid surfaces such as the rotor surface. By doing so, it would ensure adequate grid resolution particularly in the boundary layer where the adverse velocity changes occur and where the complex wake structures that trail off interact with the blade in rotation. Secondly, attempting to keeping cell aspect ratio small was also considered, as high cell aspect ratios can cause distortion and inaccuracies in capturing flow features. This was particularly difficult with the monocoque mesh as the nature of the quarter-cylindrical section containing the blade would allude to cells growing in the far-field with much higher aspect ratios. This can be seen in the upper and lower regions of the plane view of the domain in Figure 7. If more cuts were to be introduced to reduce this aspect ratio, the cells horizontally outwards of the blade's plane of motion would then increase in their aspect ratio. As such a compromise between these two regions was made. The lower and upper regions of the farfield domain were allowed to have a high aspect ratio, as the most complicated flow phenomena occur near the blade itself and this region would be preferable to have less distortion.

Another closely related consideration, was cell skewness. Although keeping the orthogonality high in a block structured solver would be preferable to pursue numerical stability and convergence, the nature of the geometry of the computational domain did not allow for this. It can be

seen from the planal view of the monocoque Figure 7 of the mesh that cells are skewed throughout the domain, but near the region of most importance, the blade, cells tend to have a much more reasonable skewness. This was also a design choice, to ensure that no vast interpolation errors that could adversely affect the development of the wake were generated. These issues are mostly solved when looking at the Cartesian-like background mesh that surrounds the blade region in the chimera setup. The simulations results to follow show that this high grid density, even distribution, low cell skewness and aspect ratio chimera mesh, does indeed perform better than the monocoque counterpart. It is important to note that in order to reduce the overall number of cells, the chimera domain employed conservative hanging grid nodes away from the rotor, in the cross over region of high grid to low grid density.

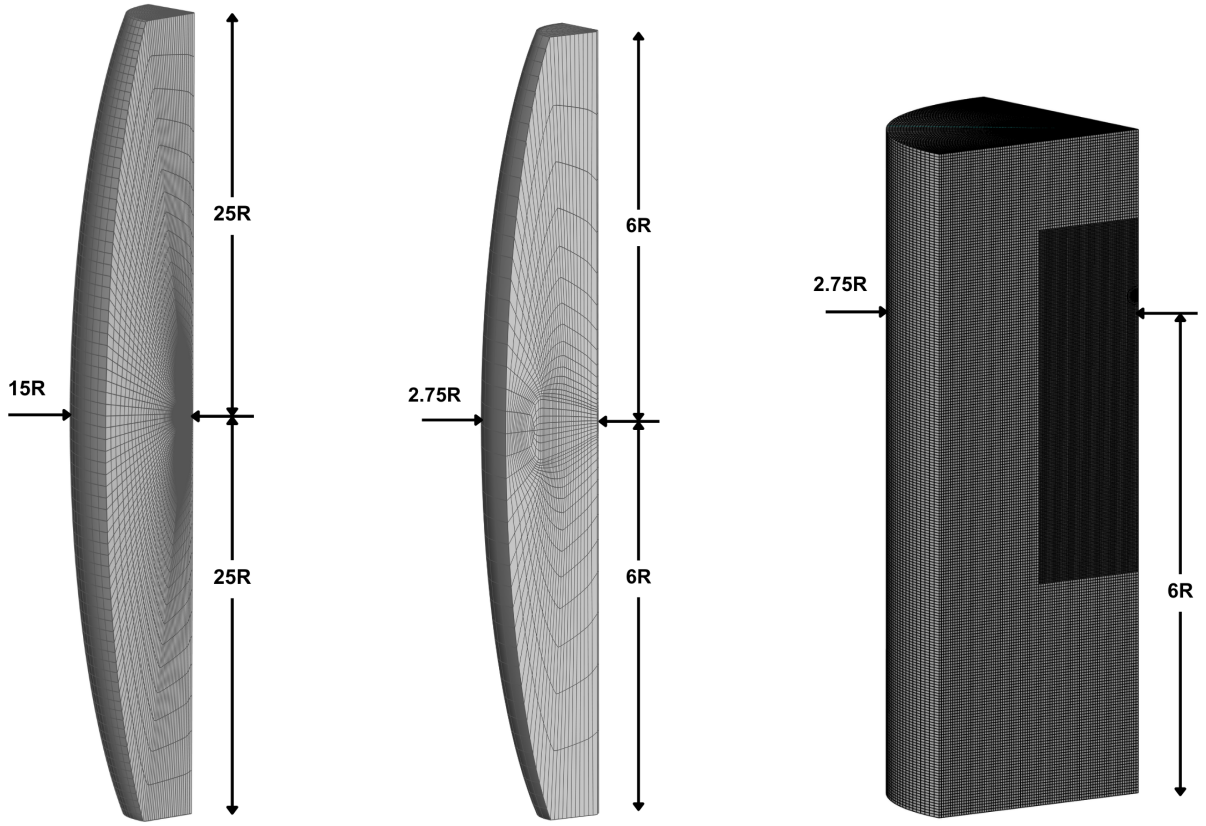

(a) M R25 (b) M R6 (c) C R6

Figure 7: Overall computational domains in 3D isometric view

Grid Acronym	M2 R25	M1 R25	M2 R6	C2 R6	C1 R6
Type	Monocoque	Monocoque	Monocoque	Chimera	Chimera
Level	2	1	2	2	1
Downstream boundary location in terms of (R)	25	25	6	6	6
Total No. of Blocks	160	160	128	184	1472
Total No. of points	5.00E+05	3.42E+06	4.54E+05	3.40E+06	2.50E+07
Total No. of cells	3.60E+05	2.84E+06	3.28E+05	3.00E+06	2.24E+07

Table 1: Grid Details

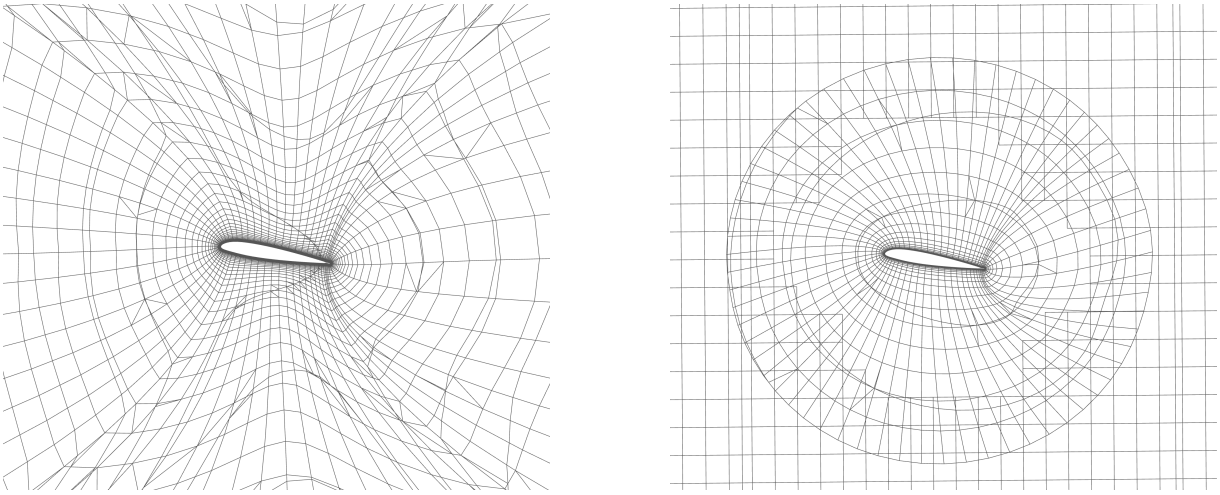

(a) Monocoque (b) Chimera

Figure 8: Blade cross-sectional view of two mesh types used

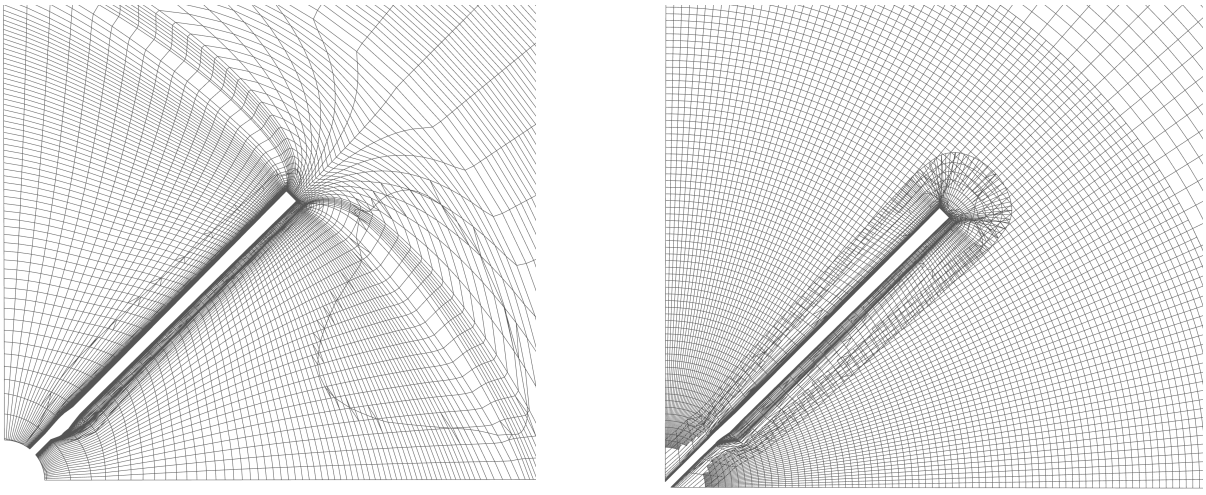

(a) Monocoque (b) Chimera

Figure 9: Blade top-down view of two mesh types used

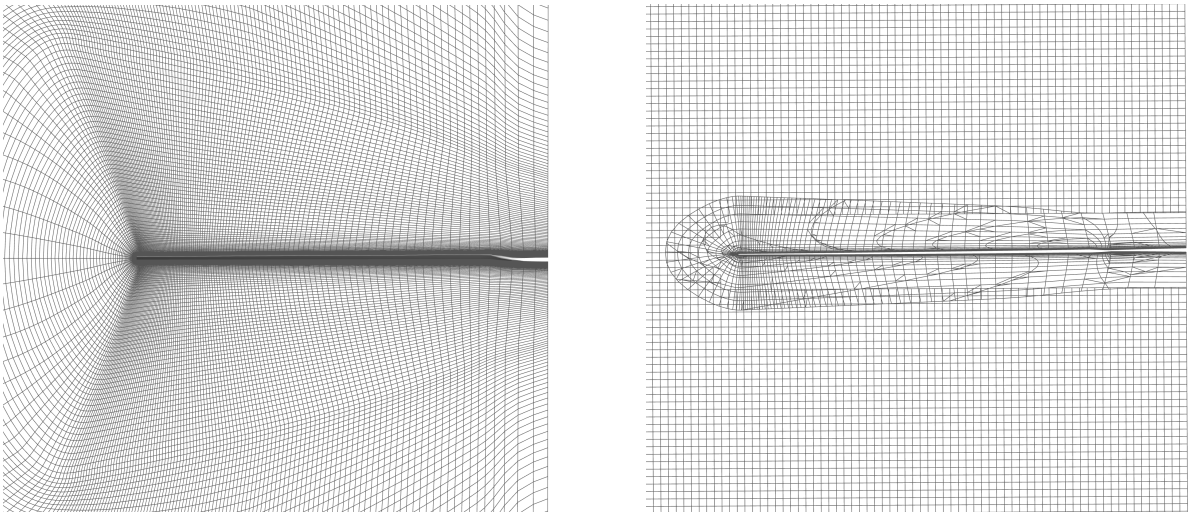

(a) Monocoque (b) Chimera

Figure 10: Blade back view of two mesh types used

3.4 Fundamental solver settings

In this section the fundamental solver settings that are used throughout all the simulations to prevail are listed, and are summarised in the associated Table 2. A justification of the settings is also provided, ranging from the time and space discretization techniques to the vortex correction modifications.

This paragraph elaborates upon the choice of the finite volume upwind scheme. There have been a large number of higher order methods and strategies that have developed to meet the high demands for a computational fluid dynamics solver to accurately simulate vortex-rich flows such as those of helicopter rotors. A study done by G. Wilke, which focal point was the investigation of 3rd and 4th order accurate upwinds schemes for helicopter rotors in hover and decent flight concluded that a 4th order accurate upwind scheme with the additional modification proposed by G. Wilke prevails over the existing strategies in place [25]. The upwind scheme used is the FMCT (4th order accurate compact Monotonic Upstream-Centered Scheme for Conservation Laws) scheme for structured meshes, as stated by Yamamoto et. al. [1] and is coupled with the SLAU2 (Modified Simple Low-Dissipation Advection Upstream Splitting Method [15]) upwind scheme [11]. The combination of the FMCT scheme with the AUSM-based SLAU2 scheme aids in the capturing of complicated flow structures ranging from unsteady supersonic jets, to vortex-dominated helicopter wakes. This is also due to the nature of the robustness of the SLAU2 scheme, which brings together the pressure and mass flux of an all-speed AUSM-family scheme enabling it to perform as desired for a wide range of Mach numbers. Another advantage of the SLAU2 scheme is that it is known to have low-dissipation properties. The additional modification proposed by G. Wilke [25] also is stated to further decrease the numerical dissipation by removing the minmod limiters in the FMCT scheme and replacing them with van Albada type limiters. This is because the minmod limiters although relatively robust, were also reasonably dissipate. A study done by Sweby [22] looked into many forms of upwind limiters and concluded that a limiter with less dissipation was the van Albada limiter.

Moreover, dual time stepping is employed. The pseudo-time integration technique was chosen to be the backward Euler LU-SGS (Lower-Upper Symmetric Gauss-Seidel) scheme [28]. This scheme is designed to efficiently solve the system of linear equations that come from the discretization of the Navier-Strokes equations. It is an implicit time-marching method, which means it considers both the future and current time steps to advance the simulation further in time. It is known to be a stable and efficient scheme since it factorizes the discretized system of equations into upper and lower triangular matrices. This is an advantage for the simulations to prevail, as unsteady simulations can tend to keep a sense of instability due to growing errors. The scheme is widely used in aerospace and mechanical engineering fields for predicting transient fluid flows via CFD software. Acknowledging that the order of the implicit time stepping technique fundamentally influences the stability and accuracy of a numerical simulation, it was decided to apply second order to this scheme, regardless of the increase in the computational

resources required per time step. This would ensure the scheme would be less dissipative as well. As for the relaxation/dissipation parameter for the implicit LU-SGS scheme, a value of 0.8 was selected which is a trade off for better computation speeds rather than robustness. Overall, this scheme offers a reasonable compromise between accuracy and computational efficiency, especially in unsteady flow cases.

The base turbulence models that were considered for this study were the Spalart-Allmaras (SA) 1-equation turbulence model [18] and the 2-equation Menter SST k-ω model [12]. After a turbulence model investigation which will be expanded upon in the following chapters, the SA model was chosen. It is known that some turbulence models can create a kind of 'numerical diffusion' which smears out a vortex core artificially. Additionally to these turbulence models and low order finite differencing techniques of the pressure and convection terms of the Navier-Strokes equations, inadequate grid distribution and density may also be a cause of this numerical diffusion [7]. Understanding that these parameters can have adverse effects on the development of a physical flow field solution, especially a vortex dominated flow such as a helicopter down wash, it was decided that a vortex correction technique for the SA model could be employed to aid in the reduction of numerical diffusion documented in literature. This technique is a modification of the production term to account for the stabilising effect of solid body rotation within the vortex core, as described my Dacles-Mariani [6] in the wing tip vortex flow prediction study.

Simulations of a helicopter rotor from a quiescent flow field can be computationally demanding while the initial flow field settles into an expected hovering state. Due to this, it was decided to set the thrust of the rotor for the first five rotor revolutions of the simulations to the approximate expected value during hovering state derived from simple momentum theory. This was performed to expedite the simulation to its final state. It is also important to note that adequately small time step sizes were chosen for both grid resolution simulations as described in the fundamental solver settings Table 2.

Temporal Intergration scheme for main and turbulence equations	Backward Euler LU-SGS [28]
Order of implicit dual time stepping scheme	2
Relaxation/dissipation parameter for implicit LU-SGS scheme	0.8
Space discretization scheme for main equations	Finite Volume + Upwind Scheme
Finite Volume upwind scheme	SLAU2 with Albada limiter [25]
Order of spatial accuracy of upwind scheme	4
Cell discretization scheme	Cell-centered
Turbulence Models	Spalart-Allmaras (SA) [18]
Vortex Correction Modification for SA Model	Dacles-Mariani et al. [6]
Reference tip mach number for hover	0.6423
Reference rotor radius (grid units)	2
Ideal gas constant ($m^2s^{-2}K^{-1}$)	287.1
Temperature at upstream infinity (K)	290.55
Static pressure at upstream infinity (Pa)	101237
Ratio of specific heat capacities	1.4
C_T set for first 5 rotor revolutions	7.99E-03
Time step size for level 2 simulations in (s)	5.56E-03
Time step size for level 2 simulations in ($^\circ$)	2
Time step size for level 1 simulations in (s)	2.78E-03
Time step size for level 1 simulations in ($^\circ$)	1

Table 2: Fundamental CFD simulation settings used

4 Results and Discussion

In this chapter the results and discussion of three main sections will be presented. These sections include two parametric studies performed for the selection of the convergence criteria and the turbulence model to employ for the following boundary and initial condition investigations. A test matrix summarizing the information of the tests performed can be seen in table 3. All simulations mentioned were performed with the fundamental settings associated with the previous section, table 2.

Test Type	Case	Grid	Turbulence Model	Boundary Condition	Initial Condition	Conv. Tolerance
Convergence Criteria Investigation	1	M2 R25	SA	Froude	QuiscentFlow	1E-06
	2					1E-05
	3					1E-04
	4					1E-03
Turbulence Model Investigation	5	M2 R6	SA	Froude	QuiscentFlow	1E-06
	6		SA (0 Coef)			
	7		SST			
	8	M2 R25	SA	Froude	QuiscentFlow	1E-06
	9		SA (0 Coef)			
	10		SST			
	11	M1 R25	SA	Froude	QuiscentFlow	1E-06
BC and IC condition Investigation	12	M2 R25	SA	Froude	QuiscentFlow	1E-06
	13			Standard	QuiscentFlow	
	14			New Model	New Model	
	15	M2 R6	SA	Froude	QuiscentFlow	1E-06
	16			Standard	QuiscentFlow	
	17			New Model	New Model	
	18	C2 R6	SA	Froude	QuiscentFlow	1E-06
	19			Standard	QuiscentFlow	
	20			New Model	New Model	
	21	C2 R6	SA	New Model	QuiscentFlow	1E-06
	22	C1 R6	SA	Froude	QuiscentFlow	1E-06
	23			Standard	QuiscentFlow	
	24			New Model	New Model	

Table 3: Complete test Matrix

4.1 Convergence criteria investigation

When considering CFD simulations, it is important to consider the measure of the unbalance, or the fluctuation in the conservation equations. For example momentum, mass, energy, and in the case of this investigation, the density. Keeping the density residual tolerance low, and consistently achieving that number throughout an unsteady computation will often indicate a more accurate solution. The smaller the unbalance achieved, the closer the simulation adhered to the physical conservation laws, which is particularly important when considering the unsteady computation of a helicopter rotor where flow dynamics and transient behaviours are critical.

Acknowledging that helicopter rotor simulations can be inherently computationally demanding due to their complicated transient flow structures, an appropriate density residual tolerance was to be selected. A tolerance which is to be a reasonable compromise between enhanced accuracy and efficiency, so that results can be produced quickly and accurately. In order to select an appropriate density residual for the computations of the boundary conditions, an investigation was carried out where the unsteady computation of a helicopter rotor in hover using the M2 R25 domain (see grid Table 1). A total of four different density residual tolerance levels were explored, ranging by three orders of magnitude from 1E-03 to 1E-06. All other settings remained constant, as observed in the constant settings Table 2.

The figures included in Figure 11 show the coefficient of thrust and Figure of Merit plotted against the number of revolutions for this investigation. Additionally, Figure 12 shows the density residual history against the number of inner iterations for each density residual tolerance, which at first glance alludes that all the tests achieved convergence at different numbers of inner iterations. It can be clearly observed that the C_T and FM plots produced by the tests using density residual tolerances of 1E-03 and 1E-04 are oscillating substantially. In particular, using a tolerance level of 1E-03 yields the largest oscillations with amplitudes inconsistently ranging between 0.2 to 0.5 over the evolution of the number of revolutions of the simulation. The line of 1E-04 exhibits results of a much less oscillatory nature, where the values of C_T and respectively FM are observed to oscillate around a much flatter base line, especially after the initial five to ten revolutions where the flow field is settling into its hovering state from quiescent flow, indicating a more stable, accurate solution where flow structures are resolved to a higher fidelity in comparison to the 1E-03 test case.

Considering the results produced by the tolerance level of 1E-05, it can be seen that the two plots in figure 11 closely adhere to the baseline of the 1E-04 graph, as if it is tracing it. This hints that with this higher fidelity tolerance, the stability issues are further mitigated and therefore providing a more numerically accurate simulation. Acknowledging that simply looking at the coefficient history of the simulation is not quantitatively enough to accept simulation results as reliable, the velocity flow field contour plots of the two test cases 1E-04 and 1E-05 were plotted at 25 revolutions and can be observed in Figure 13. Through these plots, it is visible

that there are artifacts associated with the 1E-04 data where the dashed lines representing the contour levels are tracing a rough boarder with steep changing gradients, whilst the 1E-05 data set is showing a smoother contour plot. These smoother contours more closely represent what an expected velocity flow field near a hovering rotor blade would look like. The trend of the rougher 1E-04 contour lines attempts to follow the contours of the finer 1E-05 data set, but fails to do so particularly near the blade top and on the lower left region of the flow field presented. As such, it was decided that a tolerance level of 1E-4 was not substantial to capture the accuracy of the solution required.

A final test case was considered with a density residual tolerance of 1E-06, which can also be observed plotted in the aforementioned figures. The results of this test case when considering the coefficients monitored in Figure 11 show strong consistencies with the 1E-05 test case, as they overlap each other, also suggesting a tightly and consistently converged solution. The flow field comparison of the 1E-06 against the 1E-05 case was also observed but not presented here, and showed strong consistencies in the contours of one another. When observing the density residual history against the number of iterations in Figure 12, it can be concluded that the 1E-06 test case does require 0.75·(1E+06) more iterations to reach its convergence tolerance in comparison to the 1E-05 test case. It can also be observed that both these tests reach their convergence criteria and maintain the solution residual tolerance as the simulations continue to advance in time.

From performing this analysis and looking at the residual history, coefficient history, and developed velocity flow field contour plots, it was concluded that using a density residual tolerance of 1E-06 would provide satisfactory solution accuracy. Additionally to accuracy, the results with the 1E-06 test case are also more stable, which is crucial in unsteady simulations, hindering the ability of numerical instabilities to grow and giving a better representation of the associated complex physical phenomena.

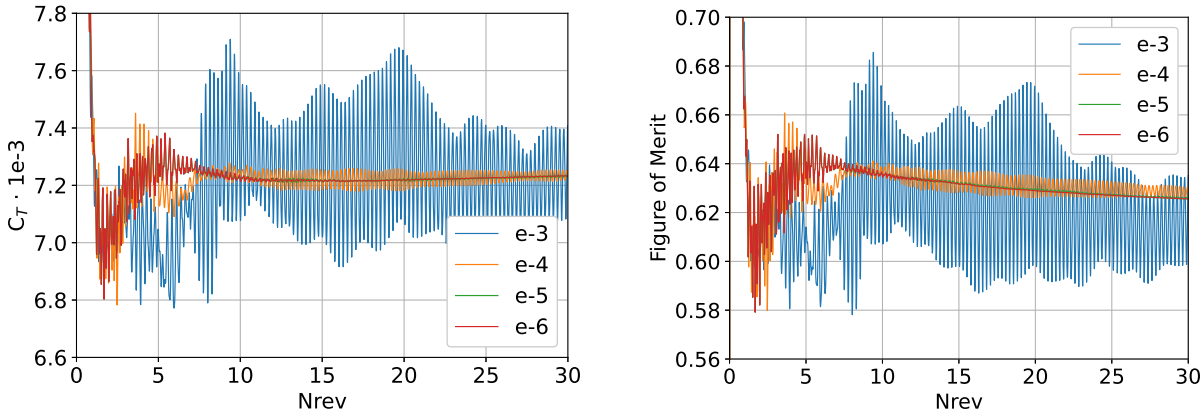

(a) Coefficient of thrust

(b) Figure of Merit

Figure 11: Density residual convergence criteria investigation results

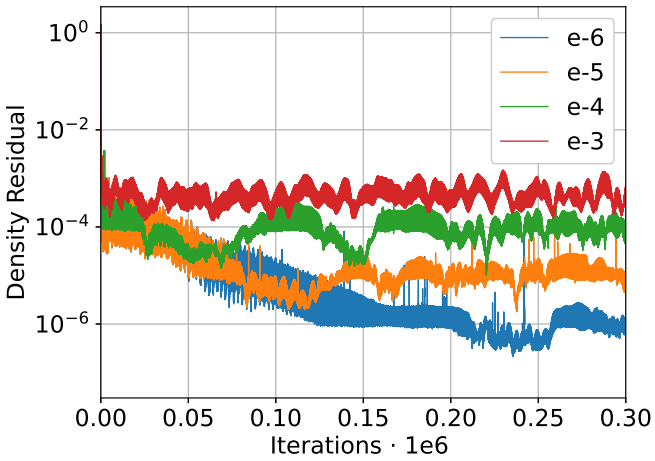

Figure 12: Density residual against iterations for convergence criteria investigation

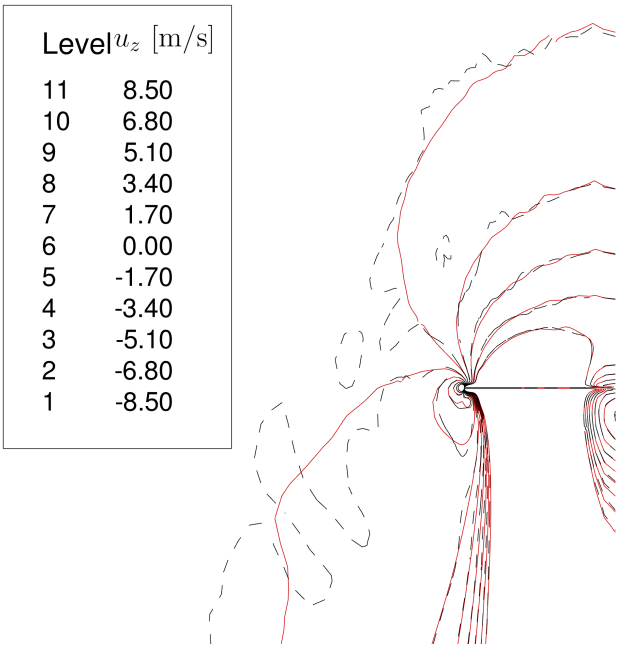

Figure 13: Axial velocity contours for 1E-05 (red) and 1E-04 (dashed black) density residual tolerance tests

4.2 Turbulence model investigation with Froude boundary

Prior to beginning boundary condition simulations, a parametric study was conducted to aid in the understanding of how different turbulence models predict the flow fields, particularly near regions of adverse pressure gradients such as the trailing and interacting vorticies near the blade tip. An investigation of such is of importance as the selection of the turbulence model for specific simulations such as a helicopter rotor in hover can be detrimental to the accuracy of the results acquired. Two turbulence models were investigated, the Spalart-Allamaras one equation turbulence model [18] and the 2003 Menter SST k-ω model [12]. Additionally, a variation of the SA model was investigated were some of the coefficients of the equations were tweaked according to recent scientific literature which will be referenced in this chapter. The transient simulations described in this section were performed with the M2 R25, M2 R6 domain, and the M1 R6 domain (Table 1), with all other parameters kept constant as described in the constant settings table (Table 2).

Initially, the first model investigated was the Spalart-Allmaras one equation transport turbulence model [18] that is often used for aerospace applications due to its simplicity and reduced computational cost. A recent publication by Zimmermann [29], which looked into transonic shock buffets over airfoils investigated the SA turbulence model constant parameters using the FLOWer and the TAU DLR CFD solvers. It was observed that there were improvements in predicting the airfoil buffet characteristics by making the model constant, c_{b2} equal to zero (calibrated value from literature is 0.622). This constant is part of a non-linear term on the diffusion term of the SA model, which is supposed to provide accurate spreading of the wake profile. This alludes that in adverse pressure gradients, this model variation has the potential to perform more accurately. An investigation within DLR also suggested that this modification of the SA model lead to accurate capturing of the helicopter rotor tip vorticies, and as such was chosen to be investigated in this study. In fact, Dr. Wilke also stated that SA converges better and is approximately 15% faster than Menter SST for hover flight state.

The Mentor SST k-ω (2003) two equation model, which is an enhancement of the original SST k-ω model, was looked into. This model is known to attain a higher degree of accuracy when observing flow physics with regions of strong adverse pressure gradients, complex boundary layers, and separation. The main difference between the original SST k-ω model and the Mentor (2003) version, is that the Mentor SST model integrates the best features of the standard model in the near-wall region and the k-ε model in the far field. The combination of these two results in an enhancement of the accuracy of the prediction of the onset and the flow state under adverse pressure gradients. These two models, the Mentor SST and the SA, are implemented into the FLOWer source code and as such are described as they are found in their corresponding literature references.

Simulation results are presented in Figures 14, 15 16, which show the coefficient of thrust and

the Figure of Merit history in terms of rotor revolutions, and the density residual history in terms of iterations respectively. It is important to note the scale differences between the two graphs of each of these figures when performing an analysis. This scale choice was chosen due to the variations of the coefficients and values attained along the y-axes of the graphs and the inconsistent number of revolutions performed for each simulation on the x-axes of the graphs. Observing Figure 14, it is evident that on both domains, the SST k-ω model is showing higher levels of thrust and as such a higher Figure of Merit in Figure 15 compared to the other models. Although, looking into the density residual history, it can be observed that the SST model is not properly converging to the specified tolerance of 1E-06 within the same number of inner iterations, but instead lingers around 1E-05. This may be the cause of the oscillatory nature of the coefficient of thrust history and as such the oscillatory nature of the Figure of Merit as seen in the plots. The simulations of the 6R domain were attempted to be pushed beyond 200 revolutions, but it is evident that the SST model is stopped at approximately 90 revolutions. This is due to the difficulty of converging the two equation model due to its more complicated physics described in its equations. It is also evident that the modified SA model is performing at a marginally higher accuracy for both domains granted the higher thrust and Figure of Merit compared to the original SA model.

Acknowledging the robustness of the original SA model, a simulation was run on the finer level M1 R25 domain to observe how the model would perform compared to the coarser mesh turbulence model tests. This can be seen labeled as 'SA - Level 1' in purple. It is evident that on this finer mesh, the SA model does indeed reach higher values of C_T and therefore FM compared to the original SA and the modified SA on the coarser level simulation domains. As the convergence and coefficient histories should be related to their corresponding flow fields, the three main tests performed with the coarser M2 R25 domain had their vorticity flow fields investigated. These vorticity contour plots of the trailing blade tip vorticies can be observed in Figure 17 and additionally, the same plot of the finer M1 R25 domain SA model study in Figure 18. It can be suggested from Figure 17 that the SST model provides the greatest vortex preservation due to its nature of preserving adverse pressure gradients compared to the other two one-equation models on the M2 domains. The orange region seen in the modified SA model plot is larger than that of the original SA model, showing that this modification aids in vortex preservation in adverse pressure gradients. The M1 R25 domain study of the standard SA model shows that with a finer domain, the SA model has substantial vortex preservation. If a study of the SST k-ω model was performed on the M1 domain, it would also likely show better flow preservation.

In conclusion, the Mentor SST k-ω model was disregarded for boundary condition studies as its two equation nature is more computationally demanding as seen from the convergence histories, regardless of the better vortex preservation alluded from the flow fields. With regards to the two SA turbulence model variants, although the modified SA model is observed to be performing

marginally better, the original SA model was chosen as this was also the unmodified model used in Jia's boundary condition investigation study [10]. Regardless, this study was interesting to research and perform as it shed insight into the importance of turbulence models in complex three dimensional flow fields such as that of a helicopter rotor in hover.

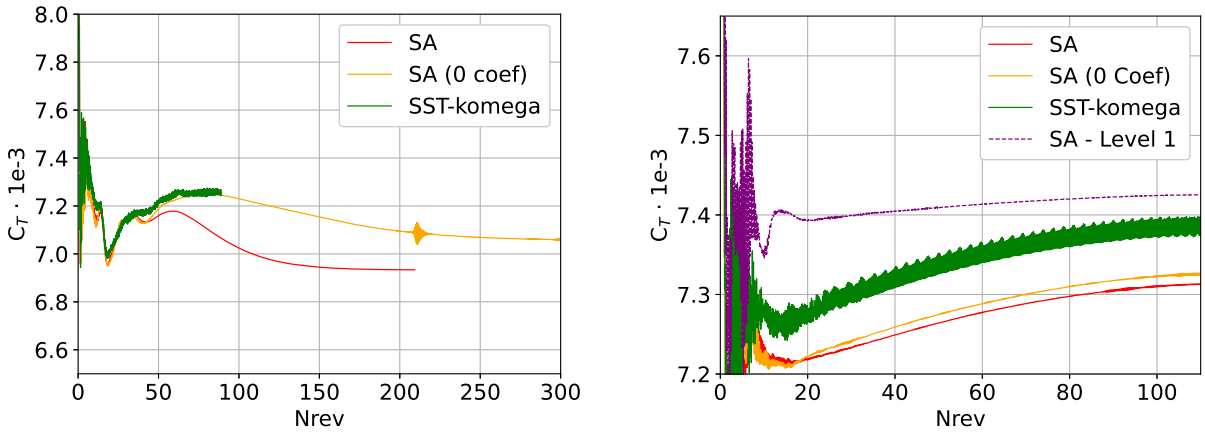

(a) M2 6R domain

(b) 25R domain

Figure 14: Coefficient of thrust against number of revolutions for different turbulence models

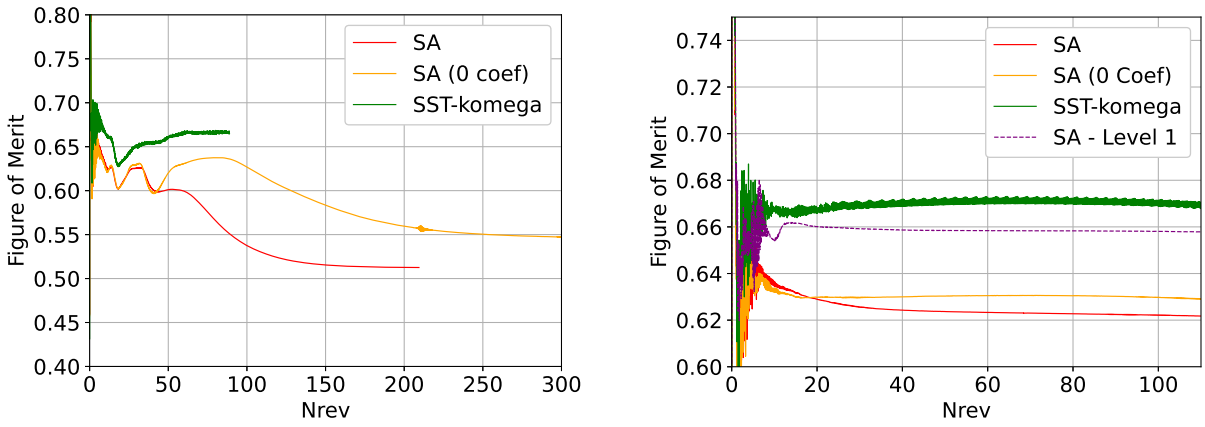

(a) M2 6R domain

(b) 25R domain

Figure 15: Figure of Merit against number of revolutions for different turbulence models

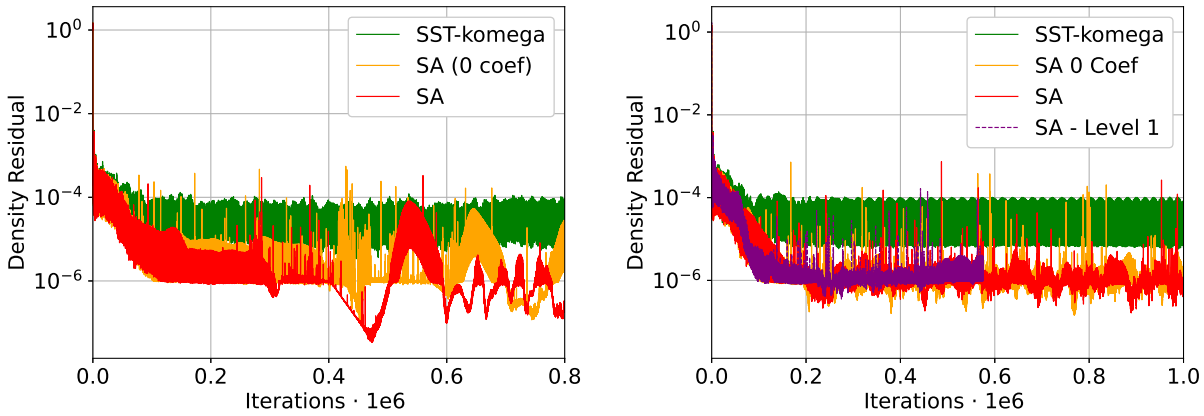

(a) 6R Domain

(b) 25R domain

Figure 16: Density residual plots for turbulence tests

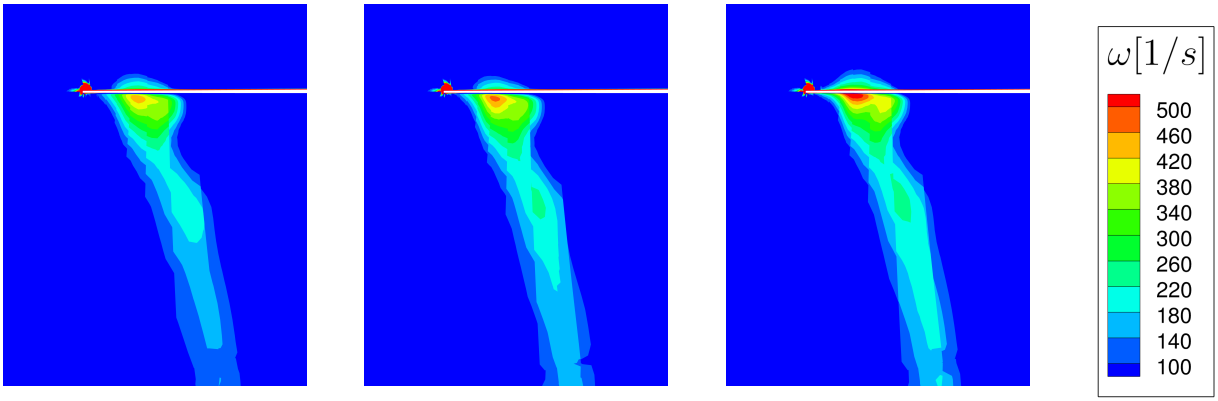

(a) SA

(b) SA (0 Coef)

(c) SST

Figure 17: Tip Vortex preservation comparison of different turbulence models on M2 25R domain

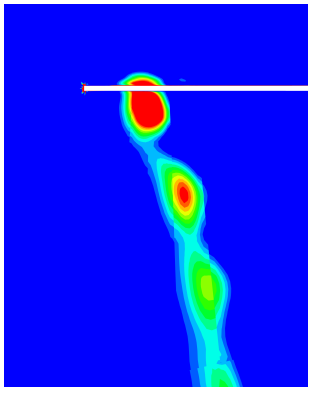

Figure 18: Evidence of stronger vortex preservation with SA model via finer M1 25R level mesh

4.3 Boundary condition investigation

In this chapter results will be presented from test cases 12 to 24 as seen in Table 3 which focus upon the three main boundary conditions and two initial conditions for hover simulations. For consistency, the chosen turbulence model from the turbulence model investigation is kept constant throughout these simulations, whilst different domain types and domain resolutions are used to test the boundary (BCs) and initial conditions (ICs). Analysis is presented with associated results and conclusions. Additionally speculations are drawn which open doors to further research studies. The three main groups which will be presented are the chimera vs monocoque simulations with the 6R downstream boundary location (M2 6R, and C2 6R domains), the finer mesh resolution chimera run as a comparison (C1 6R), and finally some interesting results found by pushing the larger monocoque domain (M2 25R) beyond 2500 rotor revolutions, which has not been recorded in any recent CFD literature.

4.3.1 Chimera vs monocoque

To begin the chapter, the results of the chimera and monocoque runs with the same farfield distance are presented. These results refer to test cases 15-21 in the test matrix Table 3 where tests 15-17 are performed with the M2 R6 domain, and tests 18-21 are performed with the C2 R6 domain. These six tests examine the influence of the different boundary conditions and initial conditions between the characteristic flow (Quiescent Flow), Froude source-sink, and Jia's new modified Spalart model based on the jet function. The line figures (Figures 19, 20, 21, 22) and associated analysis below contain an insight into the predicted Figure of Merit (FM), a rotor's chief performance parameter, the associated thrust coefficient (C_T), the accumulated sum of pseudo-iterations, and the density residual history. Additionally to these line plots, the contour plots (Figures 23, 24, 25, 26, 27, 28, 29, 30, 31, 32, 33) of the evolution of the flow fields in terms of axial velocity and eddy viscosity are provided at various timestamps in rotor revolutions of the simulation histories. Finally, to understand where the variations of the C_T values for the different simulations are coming from, the lift and torque distributions along the blade are plotted in Figures 34 and 35.

Looking at Figures 19 and 20 which present the coefficient of thrust and Figure of Merit history of the three boundary conditions on both computational domains, some interesting features appear. It is observed that the monocoque test cases require more than 150 revolutions for all the boundary condition tests to level out. The Standard characteristic flow BC reaching flatline first prior to 150 revolutions, followed closely by Froude and the New Model which flatline past 150 revolutions. The data shows that the Standard boundary condition is providing the worst Figure of Merit near 0.436, whilst the New Model and Froude BC provide higher FM values with a slight difference to one another, at 0.500 and 0.512 accordingly. It seems as the Froude model is still performing better compared to the new model with the best FM, but an insight into the sum of pseudo iterations Figure 21 may suggest otherwise. By looking

at this plot within the range of 150-200 revolutions where all monocoque test cases seem to level out on the other plots, it can be observed that the New Model takes less total amount of inner iterations compared to the Froude and Standard BCs. In fact, it takes a total of 1E+05 less inner iterations compared to the Froude BC and 3.2E+05 compared to the Standard BC, hinting at more efficient performance. The density residual plot of the monocoque runs in Figure 22 aid in the validation of the aforementioned statement, as the density residuals are observed to oscillate below the specified tolerance of 1E-06, hinting that the simulations are indeed properly converged. Further paragraphs to follow expand upon the flow fields of these monocoque meshes confirming whether this finding holds true.

Within the same figures, (19, 20, 21, 22), the corresponding line plots of the Chimera run are observed. In these plots, there is an additional dotted line in purple, labeled 'New Model (BC)', representing test case 21 from the test matrix Table 3. This additional plotted data represents the test where the New Model is imposed only as a BC, rather than both a BC and an IC. From these simulations in this C2 R6 domain, it is evident that the New Model as simply a BC and the New Model as both a BC and and IC are the only tests which converge properly and level out within 200 rotor revolutions. The Standard BC's FM history oscillates substantially between 50 and 100 revolutions whilst rapidly falling to a value of 0.436 where it seems to begin to settle out at around 250 revolutions. This low value of FM agrees with the monocoque counterpart test, but is less that the expected value that was interpolated from the experiment mentioned in the previous chapter of 0.678. This is likely due to the boundary location not being far enough from the source of disturbance, and will be looked at in the flow field analysis of the following paragraphs. In the meantime, the Froude BC's FM in this Chimera simulation has yet to settle out even at 200 rotor revolutions, and in fact is in a downwards trend, likely heading to settle into the same value recorded on the monocoque simulation of 0.512 with the aid of more revolutions. It can also be observed from the chimera sum of pseudo iterations plot, Figure 21, that the Standard BC is struggling to converge by needing a vast number of inner iterations for each revolution, while the other three tests are following similar trends to each other. The density residual plot of the chimera run in Figure 22, does indeed show that these simulations are being tightly converged with the specified low tolerance threshold.

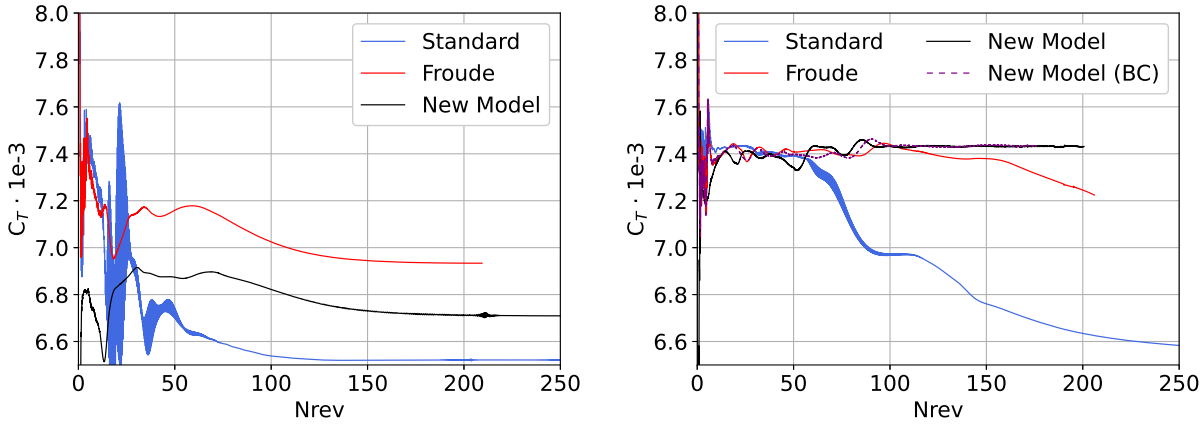

(a) Monocoque (b) Chimera

Figure 19: Coefficient of thrust against number of revolutions for three BCs in 6R domains

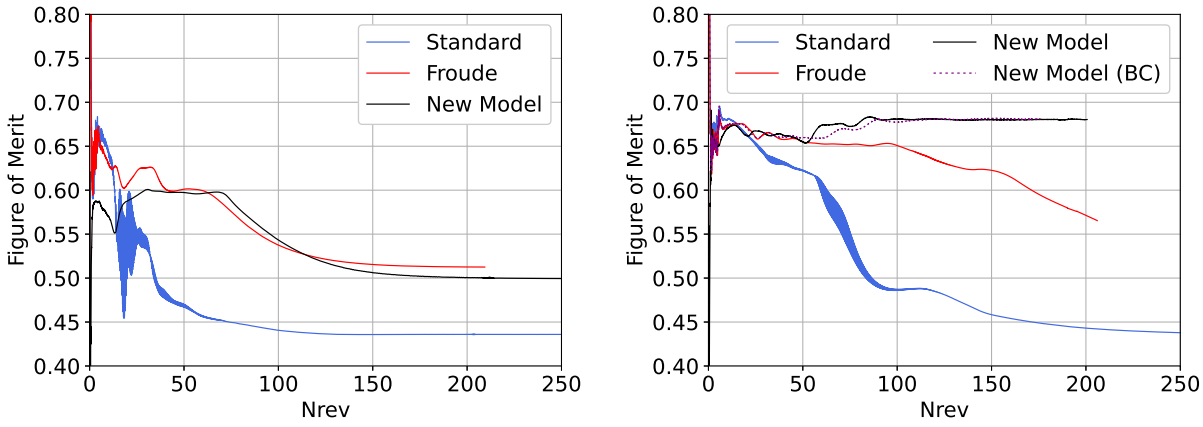

(a) Monocoque (b) Chimera

Figure 20: Figure of Merit against number of revolutions for three BCs in 6R domains

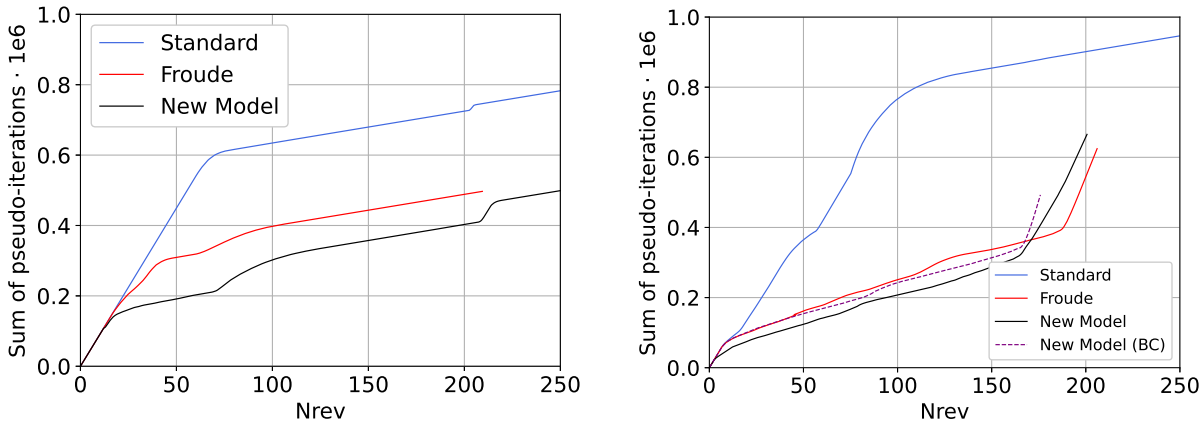

(a) Monocoque (b) Chimera

Figure 21: Accumulated sum of pseudo-iterations for the three BCs in 6R domains

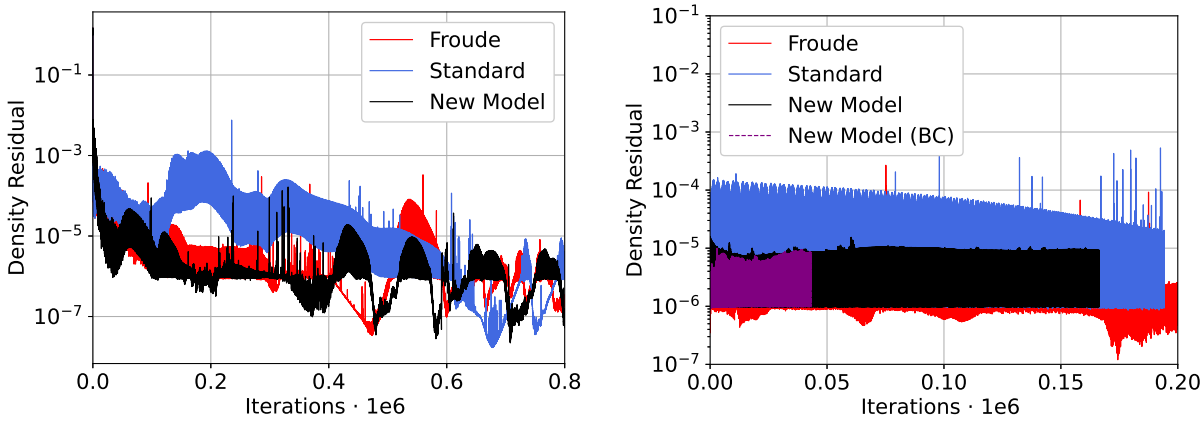

(a) Monocoque

(b) Chimera

Figure 22: Plot of Density Residual against iterations in 6R domains

To get a better insight into these value histories of the two computational domains with their different BCs, the contour plots are discussed in this paragraph. Figures 23, 24, 25, show the transient evolution of the axial velocity fields at every 10 revolutions from initialization to 40 revolutions (left to right), for the New Model, Froude, and Standard BCs in the monocoque domain (M2 6R). Then, Figure 26 shows the settled contour plots at 200 revolutions for each of the BC tests, and the associated legend for all aformentioned plots. From the first frame of the evolutionary Figures (23, 24, 25), it is evident that the New Model simulation has a substantially different initialization in comparison to the quiescent flow that the other two BCs tests are initialized with. In the first frame of Figure 23, there is a large region of downwards velocity. By looking at the following frame at 10 revolutions, it alludes that this large downwards velocity region is helping the initial chaotic vortex move through the domain, in comparison to the second frame of the other tests. In fact, it seems that the sense of rotation of the New Model IC is also helping reduce the magnitude of the starting vortex, as the region of highest velocity gradient where this vortex is expected is much less pronounced when comparing to the same frame of the other tests. In the second frame of the New Model test case, there is still a large downstream velocity region artifact left from the initialisation, and when looking at the further frames, it suggests that it manages to pull out the starting vortex completely by the 40 revolution mark. This can be observed by the smooth elongated region of downwards velocity converging and then diverging underneath the rotor.

On the other hand, observing the evolution of the Froude BC test, Figure 24, it is evident that at 40 revolutions, there is still a large pocket of quiescent flow in the bottom right corner of the computational domain, underneath the rotor. This direct comparison with the New Model BC test frame hints that the at least the initialization has aided in bringing the rotor's flow field to its hovering state. Looking at the upper light blue bubble of downwards velocity above the rotor for this frame comparison, it can be seen that the Froude's bubble has sharp changes in it's perimeter, while the New Model's has a much smoother expected contour line. This may imply

that due to the initialization of the New Model with the imposed downwards velocity above the rotor, the flow field is reaching its steady state at a faster rate.

Looking into the velocity evolution of the Standard BC test, Figure 25, it is evident that the flow field is struggling to both push out the starting vortex as seen in the first three frames, but also to reach a more steady state in its final frame of 40 revolutions compared to the evolution of the other two tests. In fact, when comparing directly the second frame of the Standard BC and the Froude BC test, it can be observed that the starting vortex not only is of larger strength as seen from the higher colour gradients, but is also closer to the rotor. By the third and fourth frame of the Standard BC test rather than evidence of the formation of the elongated blue downwards velocity region as seen in the other two test, there are more chaotic contours with regions of upwards and downwards velocity indicating that this boundary condition is having drastic effects on the evolution of the field. By 40 revolutions, the pocket of quiscent flow that was described in the Froude BC test now seen in the Standard BC test in the lower right corner now seems more pronounced with a large region of upwards velocity potentially indicating that this is a more distinguished feature in this test's flow field.

Investigating the evolution of the flow fields from the beginning can give a good indication of how well the boundary and initial conditions are performing. But in order to draw more legible conclusions regarding the BCs, the flow fields of the axial velocity and the eddy viscosity are plotted at 200 revolutions into the simulations, where all aforementioned FM history line plots have leveled out. These plots can be seen in Figures 26 and 27, accordingly. From the axial velocity plots, it is evident that the Standard BC has finally formed the elongated blue bubble below the rotor, but diverges substantially near the bottom of the domain. This bubble of varying gradient is also lower in magnitude compared to the other runs. Additionally, on the left hand side of the rotor near the rotor tip, there is a large light orange bubble of upwards velocity. This may suggest that this boundary condition is imposing a blocking effect on the flow. This is logical to expect, as the Standard BC based on characteristic flow should be allocated on a far-field region where the flow is thought to be stagnant or resembling free-stream conditions. With such a short downstream boundary condition location of 6 blade radii, clearly the source of disturbance is creating a region of non-free stream conditions at this downstream location. Furthermore, this is potentially leading to the large light orange bubble of upwards velocity as described. The associated plot of eddy viscosity at this instance for the Standard BC run as seen in Figure 27 indicates that near the bottom of the domain there is in fact a build up of eddy viscosity as seen by the light green bubble hinting at the aforementioned blocking effect.

When observing the axial velocity and eddy viscosity plots of the New Condition (New Model) and the Froude BC in the same Figures 26, 27 there are small differences between them compared to the Standard BC test. Firstly, it is evident that the Froude BC condition is not working as described in the aforementioned literature review. The blue region below the rotor which

exits the downstream domain is in fact not constrained to the $R/\sqrt{2}$ outflow area, but instead it is visible that it diverges outwards. This negative axial velocity bubble that connects to the perimeter of the downstream region implies that there the flow is escaping the domain where inflow is supposedly specified. This may be an issue of the overall downstream far field condition being allocated too close to the source of disturbance, meaning that in this short domain, this BC is not suitable for simulations. Alternatively, it may hint to a rather major assumption of the source sink model that there is no turbulence within the flow field. A look at the New Condition's BC plot provides a similar diverging downstream region which firstly converges before widening rapidly at the exit to a greater extent than that of the Froude BC test. The light blue regions above the rotors for New Condition and Froude BC tests also suggest that the New Condition simulation is experiencing a greater pull into its actuator disk with it's larger blue bubble. This is also hinted at, as the New Condition axial velocity plot has a larger light orange bubble of upwards velocity near it's blade tip compared to the Froude BC test. A look into the eddy viscosity plots of these two tests indicate similar levels of eddy viscosity, with the New Condition's test showing a slightly stronger region of internal fluid friction near the lower left region of the plots in comparing to the Froude. This may indicate that in this situation when the flow fields have settled, the Froude is still performing better than the New Condition, also alluded by the marginally larger FM it produces.

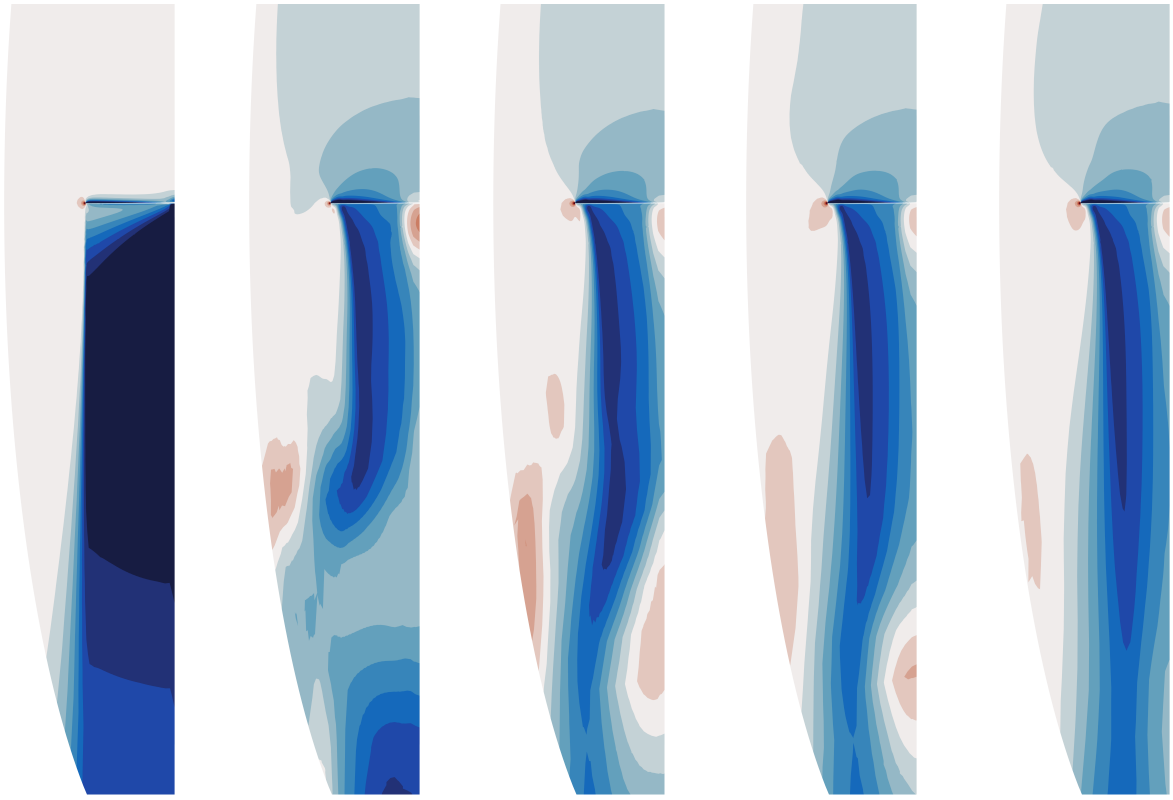

Figure 23: Axial velocity evolution in 6R domain with New Model BC and IC at every 10 revolutions from initialization

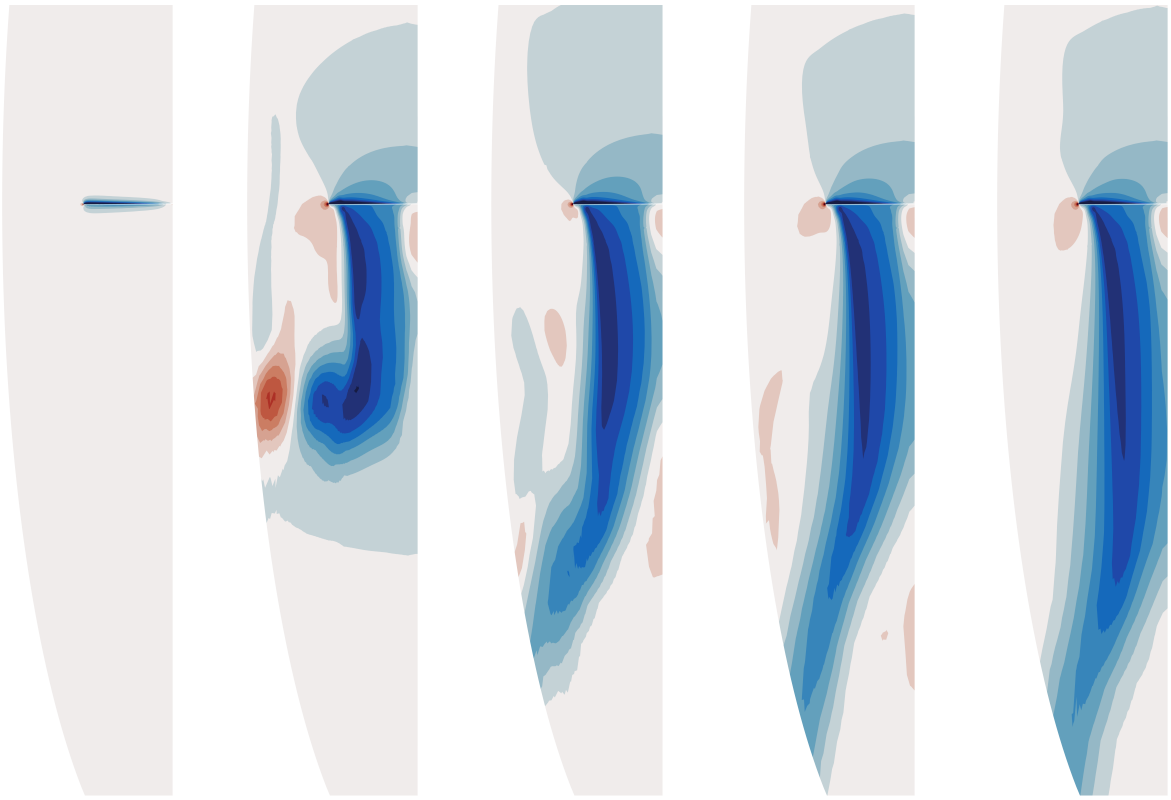

Figure 24: Axial velocity evolution in M2 6R domain with Froude BC at every 10 revolutions from initialization

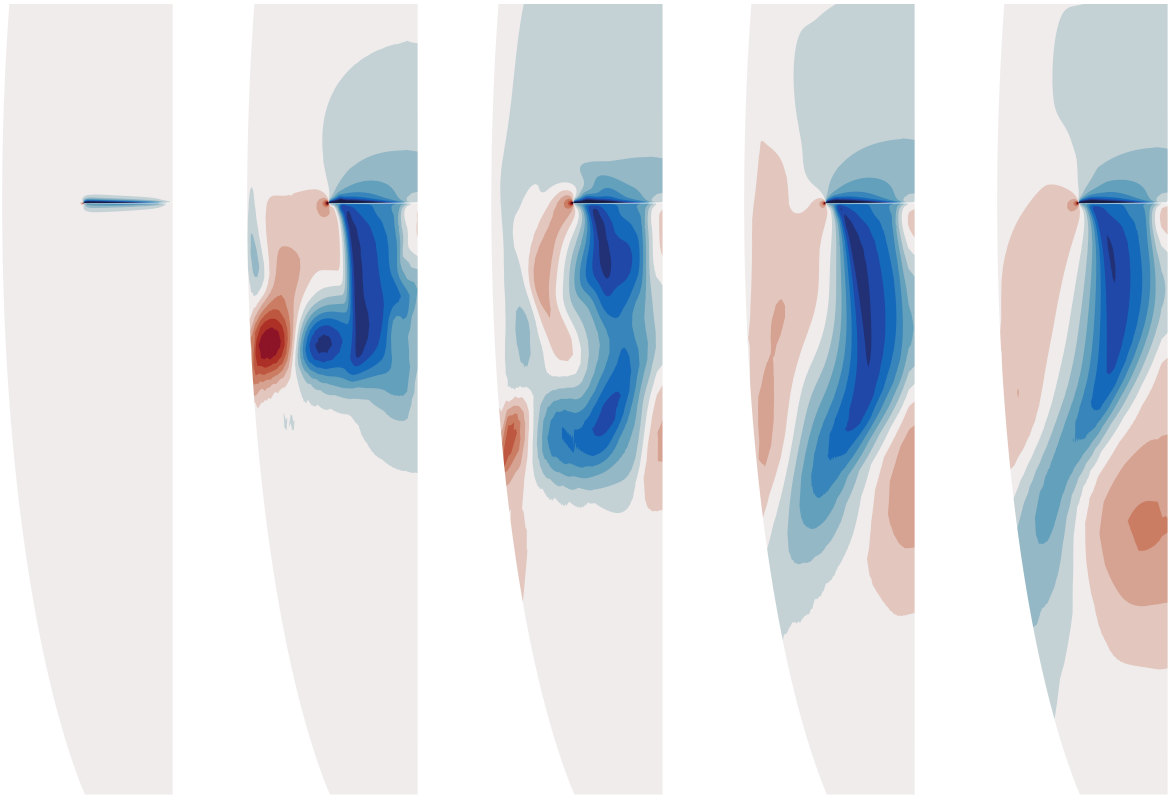

Figure 25: Axial velocity evolution in M2 6R domain with Standard BC at every 10 revolutions from initialization

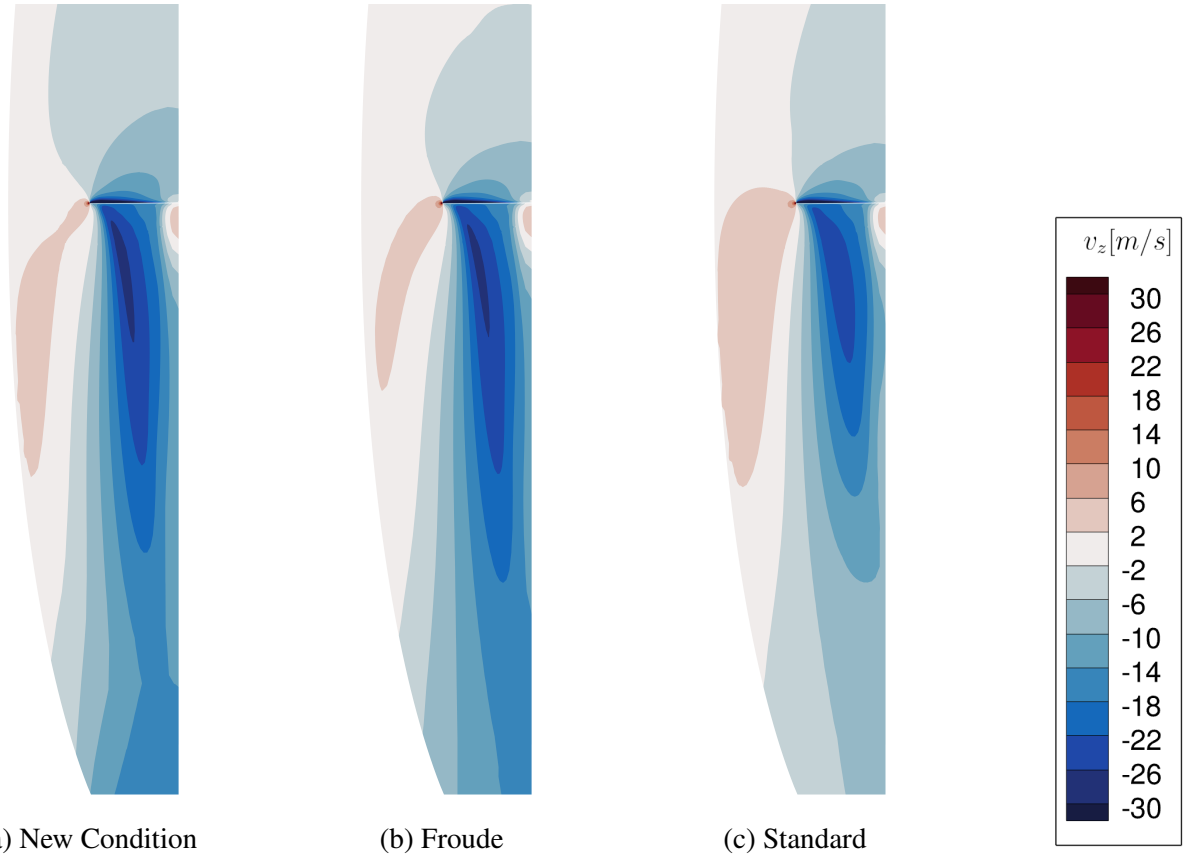

(a) New Condition (b) Froude (c) Standard

Figure 26: Axial velocity contour plots after 200 revolutions in M2 6R domain

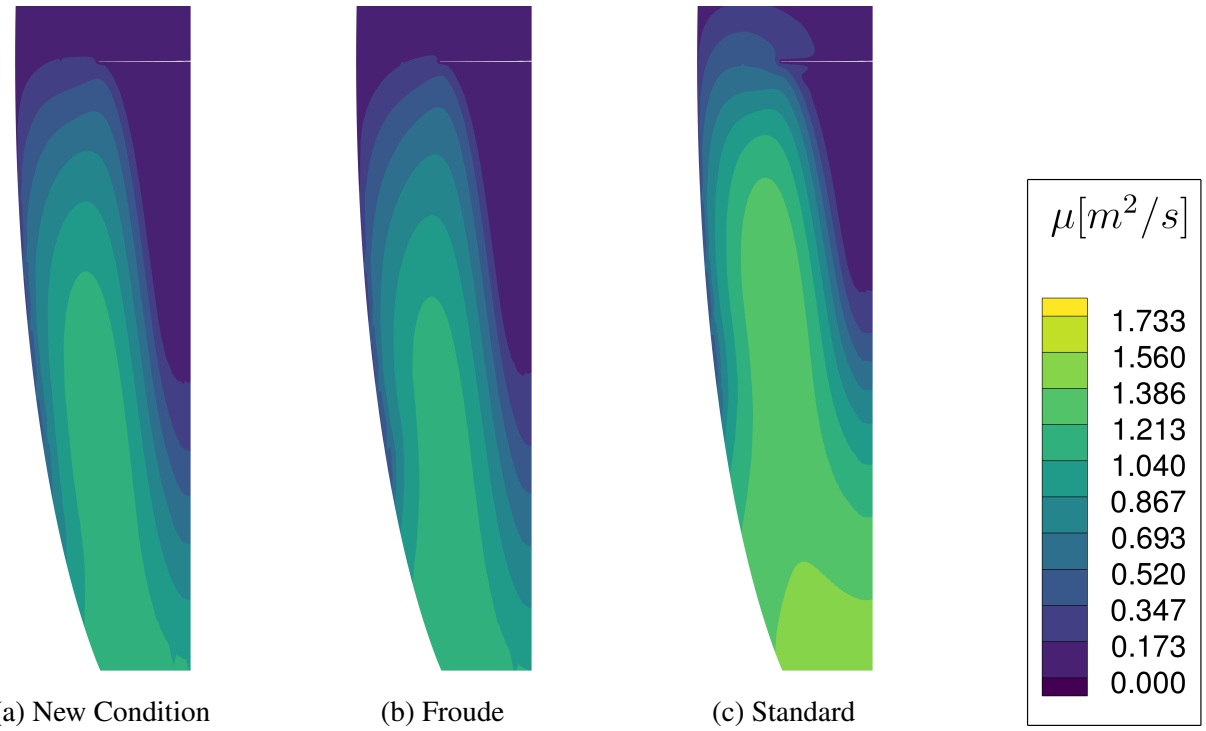

(a) New Condition (b) Froude (c) Standard

Figure 27: Eddy viscosity contour plots after 200 revolutions in M2 6R domain

Figures 28, 31, 29, 30, show the transient evolution of the axial velocity fields from initialization to 40 revolutions, for the New Model (IC and BC) , New Model (BC), Froude, and Standard BC tests in the chimera domain (C2 6R). These refer to tests 18-21 in the Test Matrix table (Table 3). This allows a direct comparison between the same time stamps between the two computational domains. It is important to note that this chimera mesh although labelled the same level as the monocoque mesh (M2 6R), contains an order of magnitude more cells (See mesh parameter Table 1). By investigating the flow fields of this finer mesh study, an insight can be granted as to why the FM history plot of the simulations vary substantially, and why the New Model as a BC may be preforming with more robustness. From these plots, it is observed that the three runs that were also attempted on the monocoque (M2 R6) domain are following similar trends. This means that the New Model test, Figure 28, with the initialized flow field, is outperforming the Standard and Froude runs when looking at the 40th revolution frame. Within the 40 revolution frames of the Standard and Froude runs in Figures 30, 29, accordingly, it is visible that the Standard BC's test contour plot is still congested with its starting vortex, while the Froude's plot is closer to its expected state, with artifacts of the vortex still visible in the flow field.

Interesting phenomena are observed in Figure 31, where the flow field evolution with the New Model BC test initialized with quiescent flow is presented. By the second frame at 10 revolutions, there is a blue bubble of negative velocity that begins in the lower right corner of the domain and decreases in strength as it grows towards the rotor. This region indicates that even without the initialisation of the New Model, the boundary condition is implying an adverse effect on the flow field as it attempts to pull the rotor down wash through the bottom if the domain. The starting vortex within this frame is in approximately the same down stream location in the flow field as the Froude's second frame in Figure 29, with similar gradients of axial velocities along their centers. In fact, by the 40th revolution frame, the flow field of the New model as only a BC and the Froude are showing similar flow fields that show artifacts of the starting vortex in the lower left region of the plot, but seem to be reaching their steady state. A slight difference here is the New Model test's 40th revolution frame indicates a stronger outflow on the lower right in dark blue in comparison to the Froude's field. This suggests that there is a stronger sink effect being created by this jet function based model.

To draw more rounded conclusions, the same axial velocity plots and the eddy viscosity contour plots at 200 revolutions for all cases with this domain are presented in Figures 32 and 33 accordingly. The contour plots of the Standard BC test are eye catching as they contain the largest differences compared to the other tests. In the axial velocity plot, there is clearly a blockage effect being imposed on the downstream outflow region beneath the rotor as can be seen from the blue velocity contour which is being suppressed. Additionally, there is the large positive axial velocity contour level accumulated on the left side of the domain which connects to the blade tip. This is potentially an artifact of the boundary condition failing in acting as a far field condition, and the associated plot of eddy viscosity in Figure 33 suggests the same outcome

with its regions of large turbulent eddies that are not able to escape the domain that even begin to engulf the rotor.

By doing a direct comparison of the settled contour plots of the New Model as simply a BC and as both a BC and IC, it is evident that at 200 revolutions the plots are almost identical for both tests. The elongated blue bubble of axial velocity contracts as it travels away from the rotor until approximately 3R downstream, where it shows evidence of divergence likely due to the build up of turbulent eddies seen in the corresponding eddy viscosity plot in Figure 33. The Froude BC's simulation follows a similar flowfield at this instance, with a slightly weaker outflow region most likely due to the supposedly imposed $R/\sqrt{2}$ contraction region. Interestingly, there is a small bubble of upwards axial velocity on the lower left region in the Froude BC's velocity plot, which when correlated to its eddy viscocity contour, it is evident that there is a small build up of eddies or tip vorticies trying to pass the BC which may be causing a recirculation effect of the oncoming flow back up towards the rotor tip. This phenomenon is less vivid in the New BC's eddy plots, hinting that the suction effect of the New Model is helping reduce any recirculation effects that the Froude BC may be inherently imposing on the flow evolution.

Isolating the results from the New Model simply as a BC and as a BC and IC, interesting results can be drawn. Firstly, referring to the FM history plot, Figure 20, it is evident that both simulations level out at approximately 90 to 100 revolutions, where the New Model as both a BC and an IC is performing marginally better. This is due to the graph leveling out at approximately 90 revolutions whilst the test with the New Model as just a BC is still dampening out it's final oscillations. An early stage indicating that the New Model condition as both an IC and a BC is performing better than simply being a BC is in the final frames (40 revolutions) of the evolutionary axial velocity contour plots, Figures 28 and 31. Here it is clear that the initial starting vortex is already flushed with the imposed IC while when observing the New Model simply as a BC, there are still remaining starting vortex artifacts within the flow field. In Jia's work [10], it was noted that the IC has a substantial effect on the evolution of the field greater than imposing the condition as a BC, and similar results are seen here. Additionally from his work, it was concluded that the new BC does not show any evident speedup in convergence of the flow solution in comparison to the Standard freestream condition, but the wake can indeed be developed at a faster rate because of the imposed velocity field at the boundary. In the case of this investigation results suggest that the new model is more robust and can perform well on both domains tested in this section (M2 6R, C2 6R). Particularly for the M2 6R domain, it was concluded that the New Model is requiring less total number of inner iterations and hence computational costs to achieve convergence whilst still providing similar results to the Froude test.

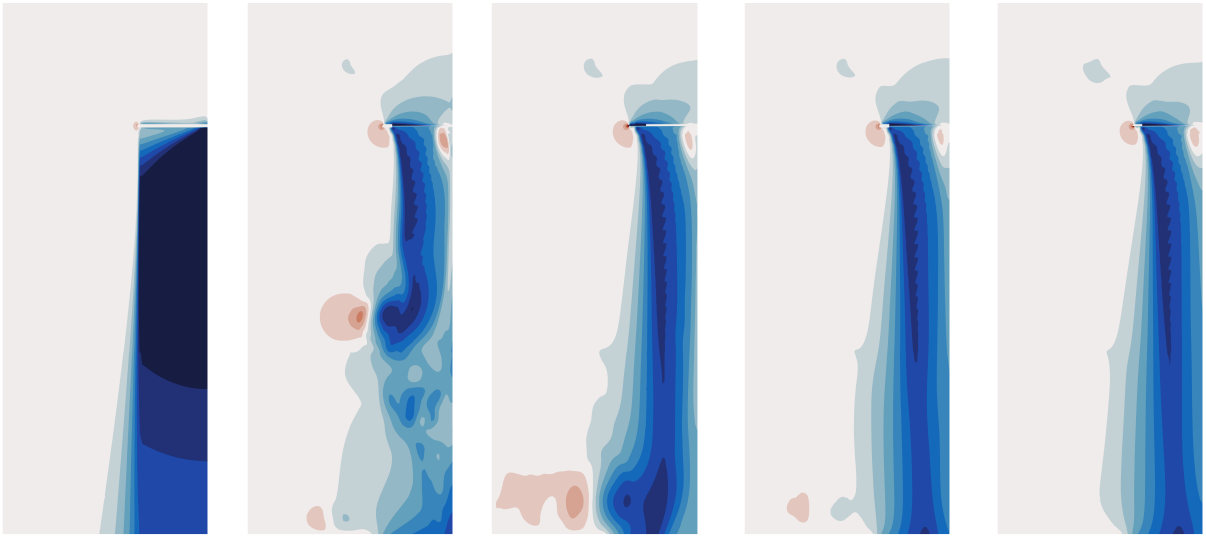

Figure 28: Axial velocity evolution in C2 6R domain with New Model BC and IC at every 10 revolutions from initialization

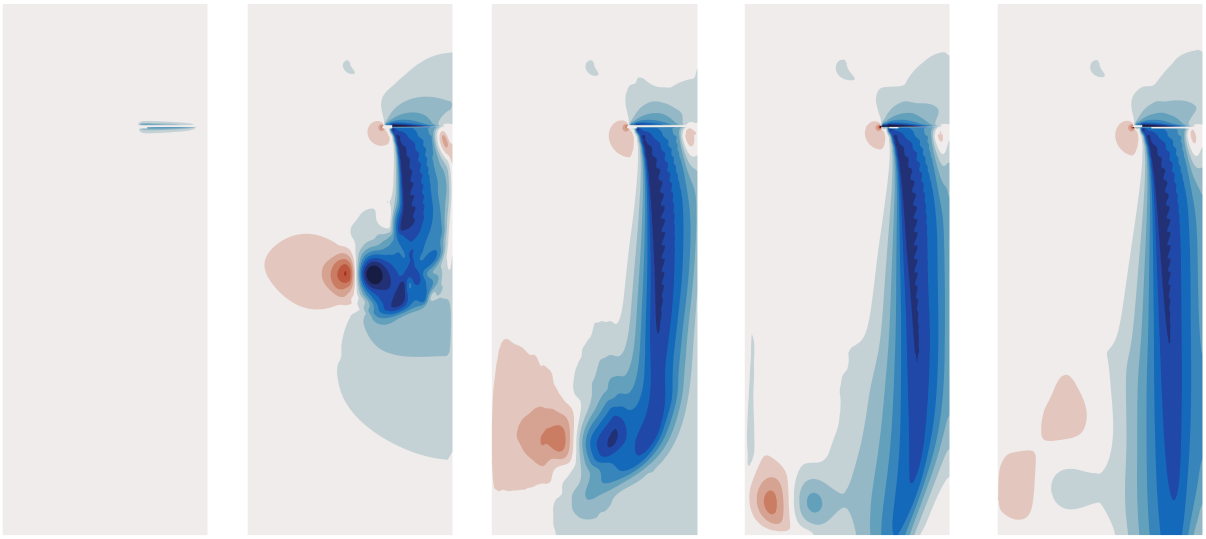

Figure 29: Axial velocity evolution in C2 6R domain with Froude BC at every 10 revolutions from initialization

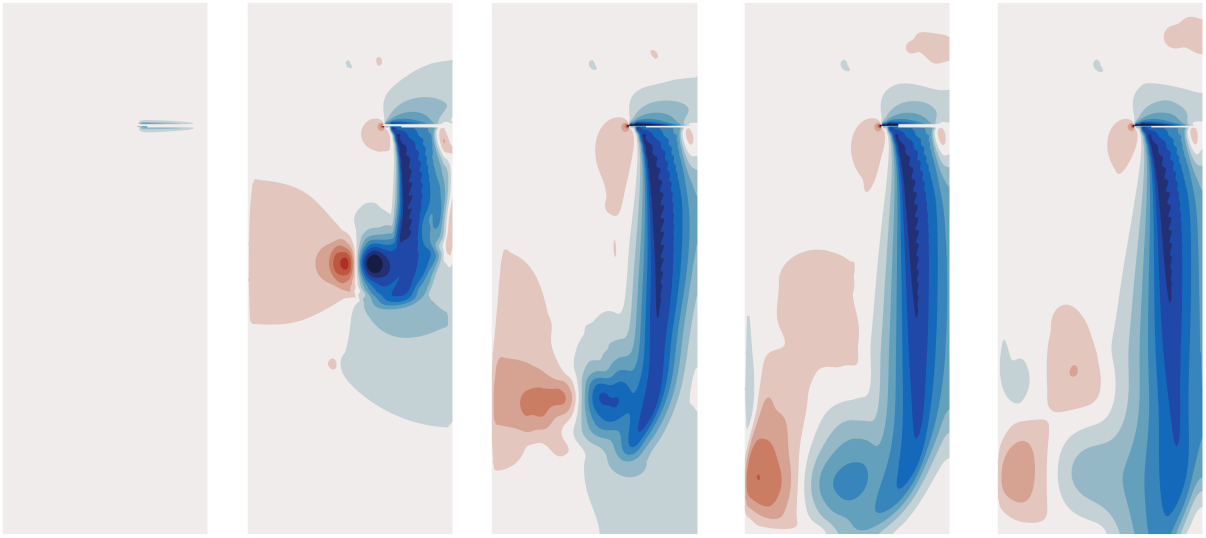

Figure 30: Axial velocity evolution in C2 6R domain with Standard BC at every 10 revolutions from initialization

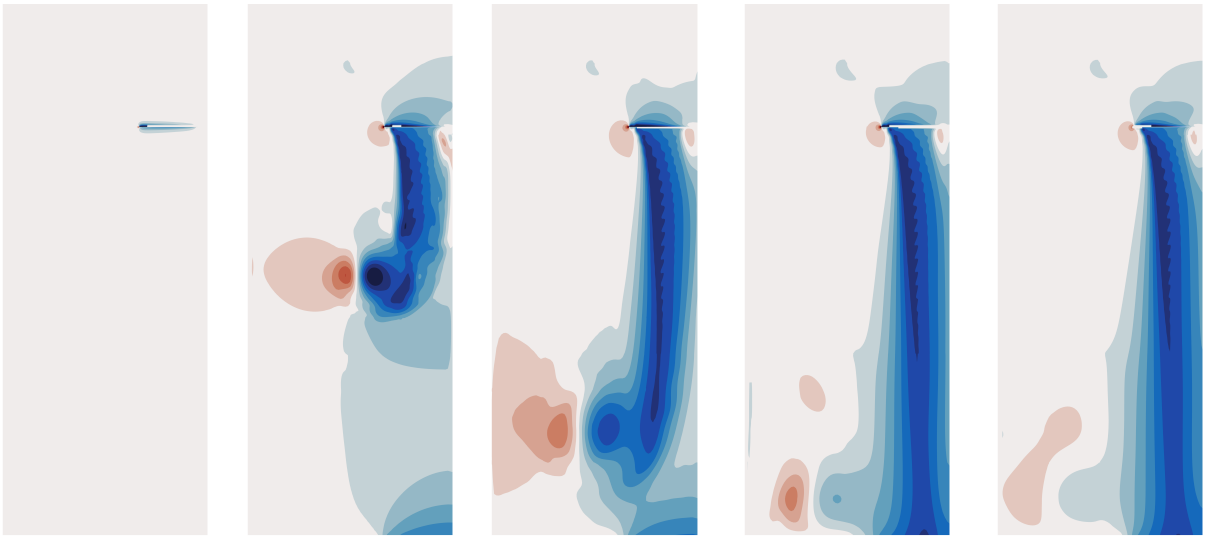

Figure 31: Axial velocity evolution in C2 6R domain with New Model BC at every 10 revolutions from initialization

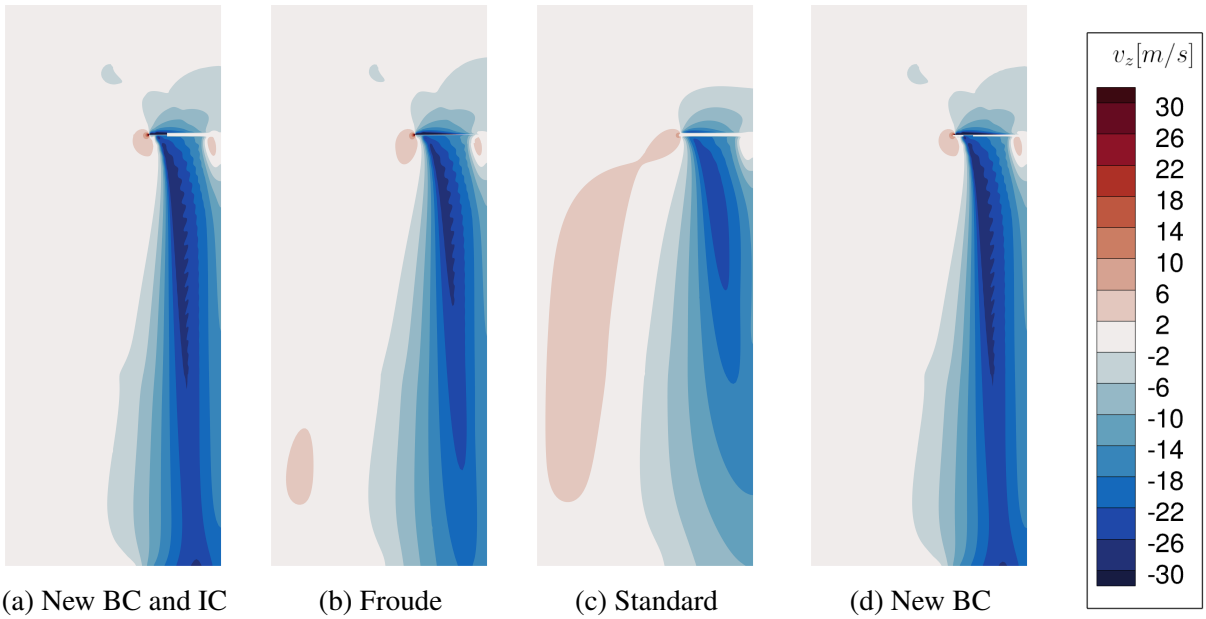

(a) New BC and IC (b) Froude (c) Standard (d) New BC

Figure 32: Axial velocity contour plots after 200 revolutions in C2 6R domain

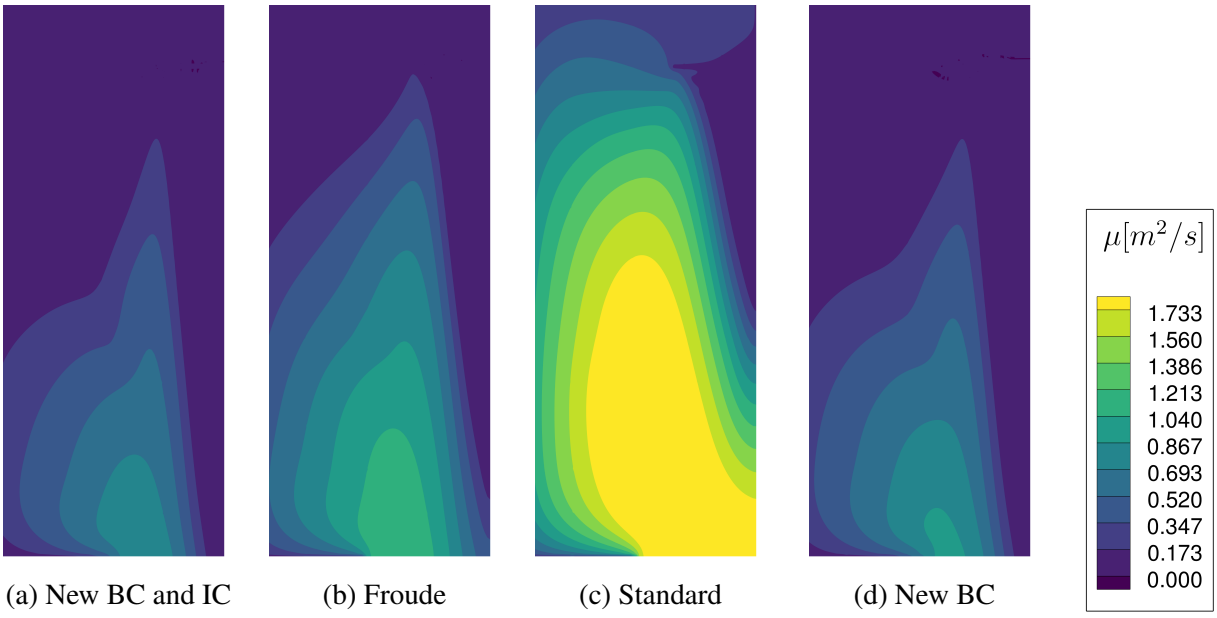

(a) New BC and IC (b) Froude (c) Standard (d) New BC

Figure 33: Eddy viscosity contour plots after 200 revolutions in C2 6R domain

To obtain a more detailed insight into why the values of FM for the different tests are varying, the spanwise distributions of lift and torque along the length of the rotor blade are plotted in Figures 34 and 35 for both monocoque and chimera 6R domains after 200 revolutions. Understanding these distributions can aid in attempting to pinpoint the flow phenomena such as the aging vortex of the previous rotation that are occurring near the blade which can have a substantial dependency on the functioning BC, mesh, and turbulence model used. By comparing the lift distributions of the monocoque and the chimera simulations in Figure 34, it is evident that the chimera tests have a greater overall area underneath their lift distribution curves. This explains the higher coefficients of thrust of the chimera tests over the monocoque tests as seen in Figure 19. A potential cause of this difference may be due to the higher mesh density of the chimera C2 6R domain preserving the flow field particularly in the regions of high velocity gradients in higher resolution. In other words, the high gradient regions of the flow field do not smear out by the inherent numerical dissipation of the computational domain as intensely as with the lower mesh density of the M2 6R domain. Additionally, the chimera domain contains more uniform cells due to its systematic cube based background mesh compared to the high aspect ratio skewed cells in certain regions of the M2 6R domain.

A point of interest on the lift distribution plots which also correlate to the torque distribution plots is the steep positive gradient, peak, and steep negative gradient hump near the blade tip, approximately at $r/R = 0.9$. After an inspection of the 3D flow fields, it was found that this artifact is caused by the trailing tip vortex of the previous blade rotation interacting with the blade. On the monocoque lift plot, all BC tests follow similar trends with Froude's plot peaking slightly above the other BC tests. This inconsistency may be occurring due to the imposed inflow velocity at the boundary which is attracted towards the sink at the center of the rotor. As the inflow comes into the domain from the boundary slightly below the blade's plane of rotation, it may be possible that direction of the flow aligns with the tip vortex outer upwards pointing velocity vector. Obtaining the magnitude of these velocities together can lead to a greater overall upwards velocity region on the blade tip side of the trailing vortex causing greater lift. It is also visible that the standard BC test plot is slightly lower than the other tests between the range of $0.50 < r/R < 0.85$ for both monocoque and chimera domains. To explain the phenomena, the eddy viscosity plot (Figure 27) was re-examined, and a hypothesis was formed. Due to the blocking effect caused by the Standard BC, there is a region of eddy viscocity that engulfs the area near the rotor tip seen in light blue. There is a possibility that this turbulent region is disrupting the oncoming flow onto the rotor, causing the blade to generate less lift in this region.

Observing the chimera domain blade distribution plots, similar trends emerge for the Froude and Standard BC tests. The New Model BC test lift plots on the other hand are peaking substantially higher than the rest, in turn giving higher thrust values. It is important to note that at 200 revolutions into the simulation, the New Model as only a BC and as both a BC and an IC are displaying the same lift distribution plots, meaning that the IC no longer having an influence on

the transient flow field, but has aided it in reaching this steady state faster. The lift peak due to the trailing vortex's upwash side interacting with the oncoming blade is an interesting phenomena. A examination of the 3D flow field in this case showed that the oncoming tip vortex was shifted, such that it's core center was marginally closer to the blade's plane of rotation. As such, the blade interacts with the velocity peak at the vortex core radius which has a higher upwards component. This in turn leads to the heightened peak seen in the plot. With the New Model as a BC, it seems as if either this trailing vortex is hesitant to move down the domain due to the imposed condition on the boundary, or it is potentially being reinforced by it, causing a more adverse affect on the blade.

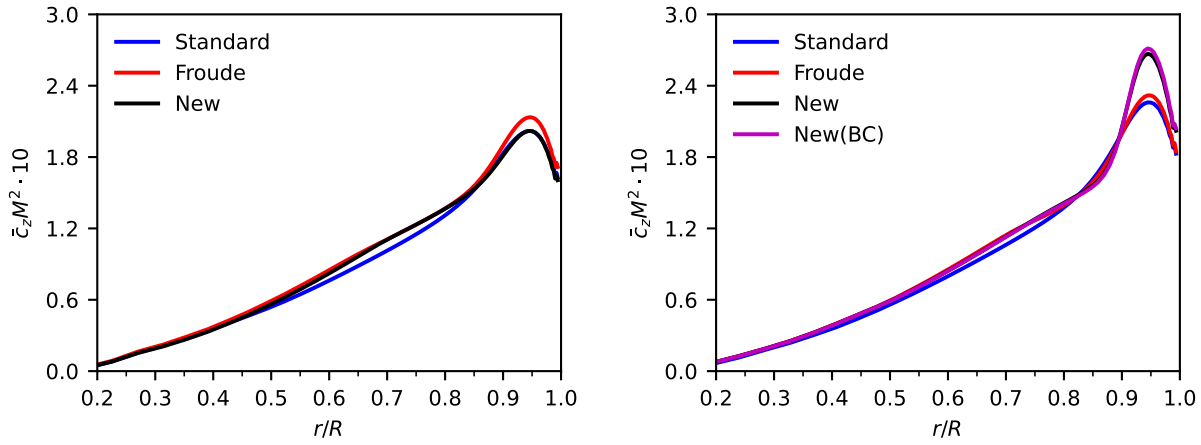

(a) Monocoque (b) Chimera

Figure 34: Lift distribution with 6R domains for three BCs beyond 200 Revolutions

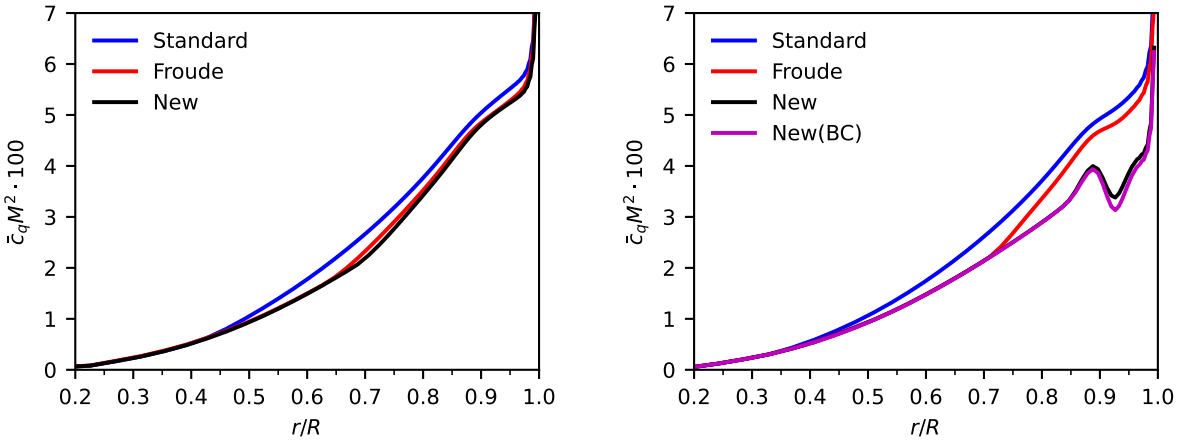

(a) Monocoque (b) Chimera

Figure 35: Torque distribution with 6R domains for three BCs beyond 200 Revolutions

4.3.2 Chimera domain finest mesh comparison

In order to comprehend some of the inconsistencies of previously discussed results, a fine mesh study was performed using the chimera technique for the three BCs. These tests correspond to cases 22-24 in the test matrix Table 3. This mesh C1 6R had the same shape as the C2 6R but with a much higher resolution as expected from a level 1 mesh. In fact, the C1 6R domain has an order of magnitude more grid points in comparison to the C2 6R domain (see Table 1). Even on DLR's CARA HPC cluster, this simulation was very computationally demanding and required a substantially longer time to simulate. Due to the shortage of time of the placement, data only up to 20 revolutions was able to be collected and is presented here. The plots of CT, FM, accumulated sum of pseudo iterations, density residual and axial velocity contours are discussed as done in the previous chapter. Additionally, the Y-vorticity contours are also displayed. Supporting plots in this section can also be found in the Appendix.

Firstly, referring to Figure 36 which shows the plots of CT and FM, a consistent leveling of the values is observed, all within close proximity of each other. This was also partially observed in the C2 6R domain simulations approximately around the 15-25 revolution band (Figures 19, 20 for reference). But in the C2 6R domain, this time frame region is seen as more of a coefficient plateau which soon ends and takes at least 70 more revolutions before settling again. These C1 6R domain simulations although may seem settled in their coefficient plots, are still developing. An insight into the axial velocity plots 20 revolutions into the simulation seen in Figure 38 proves this, as the steep velocity gradients representing the initial starting vorticies are still visible in all flow fields. These axial velocity plots show more detailed but similar flow mechanics to the coarser mesh chimera runs, supporting that the New Model IC is helping reduce the strength of the starting vortex and helping expel it out of the domain at a faster rate compared to the quiescent flow IC.

Secondly, looking directly at the Y-vorticity plots of the three BCs 20 revolutions into the transient simulations in Figure 39, the aforementioned vorticies can be seen. Displaying the vorticity plot can give a better representation of the vorticies rather than the examination of the axial velocity plot. In the New Model IC and BC test plot, it is evident that the initial vortex is on such a downwards dominated trajectory that it will escape near the middle of the domain. In comparison, the Froude BC test's starting vortex seems to be on a downwards trajectory with a component to the left of the domain. The Standard BC test's starting vortex trajectory with an even stronger component to the left. This hints that the New Model BC is having an adverse pulling effect on the rotor downwash, whilst the Froude and the Standard BCs may already be imposing a blocking effect of increasing strength accordingly.

Finally, it is interesting to observe the similarities of the load distribution plots as seen in Figure 40. In these plots, there are no strong inconsistencies depending on which BC has been used as previously seen on the coarser C2 6R mesh. This means that the blade's oncoming aging vortex

is similar on all tests within this 20th revolution. This leads to the hypothesis that since the flow fields are still developing, the full effect of the BC has yet to be witnessed. Particularly, the regions of re-circulation that have been previously seen as the light orange bubbles of upwards axial velocity in plots such as Figure 32 have yet to form which may be the culprit of the inconsistencies seen in the previous chapter's blade distribution plots. From the higher peaks and lowwer troughts of the Standard BC's plot, better performance is suggested, but this may be due to the rotor being in a more in-ground-effect state due to the blockage at the farfield boundary.

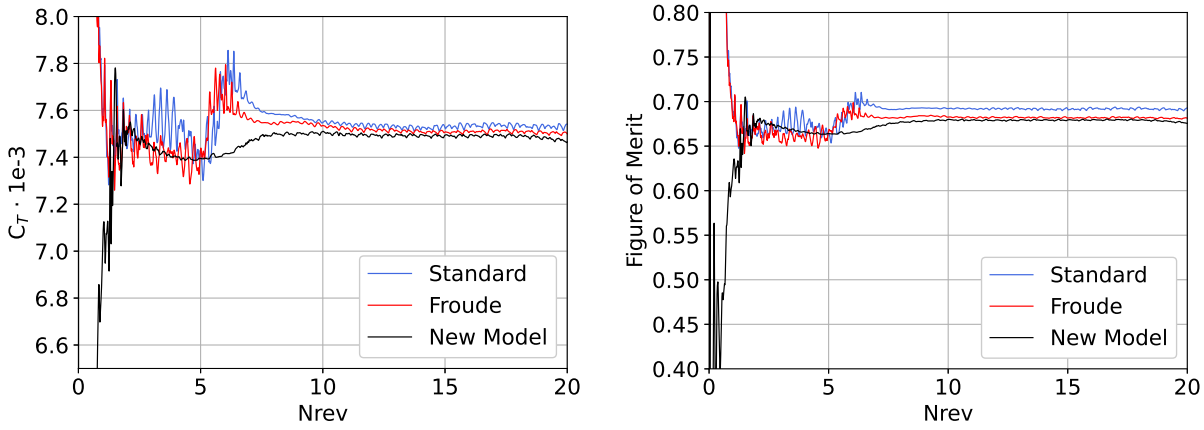

(a) Coefficient of thrust

(b) Figure of Merit

Figure 36: Finest mesh study C1 R6 coefficients for three BC tests

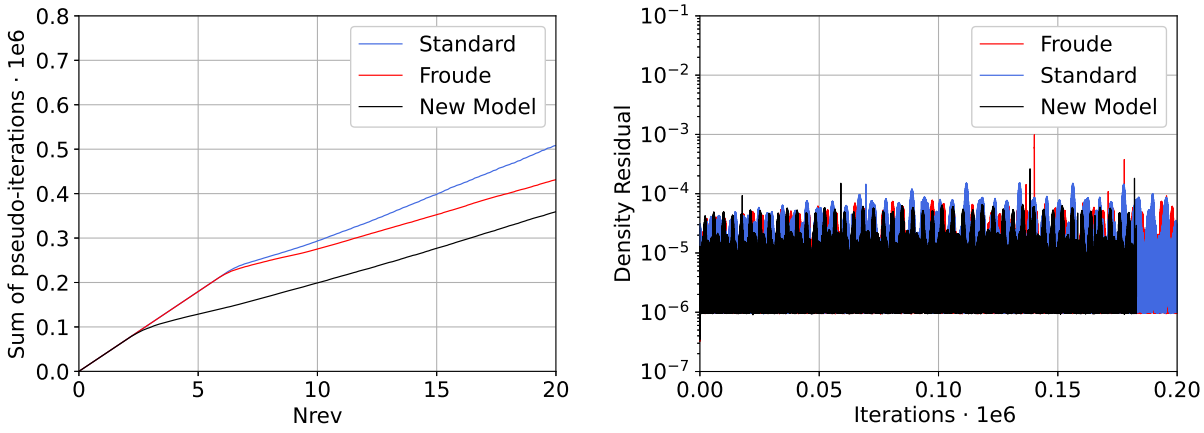

(a) Sum of pseudo iterations

(b) Density Residual

Figure 37: Finest mesh study C1 R6 results for three BC tests

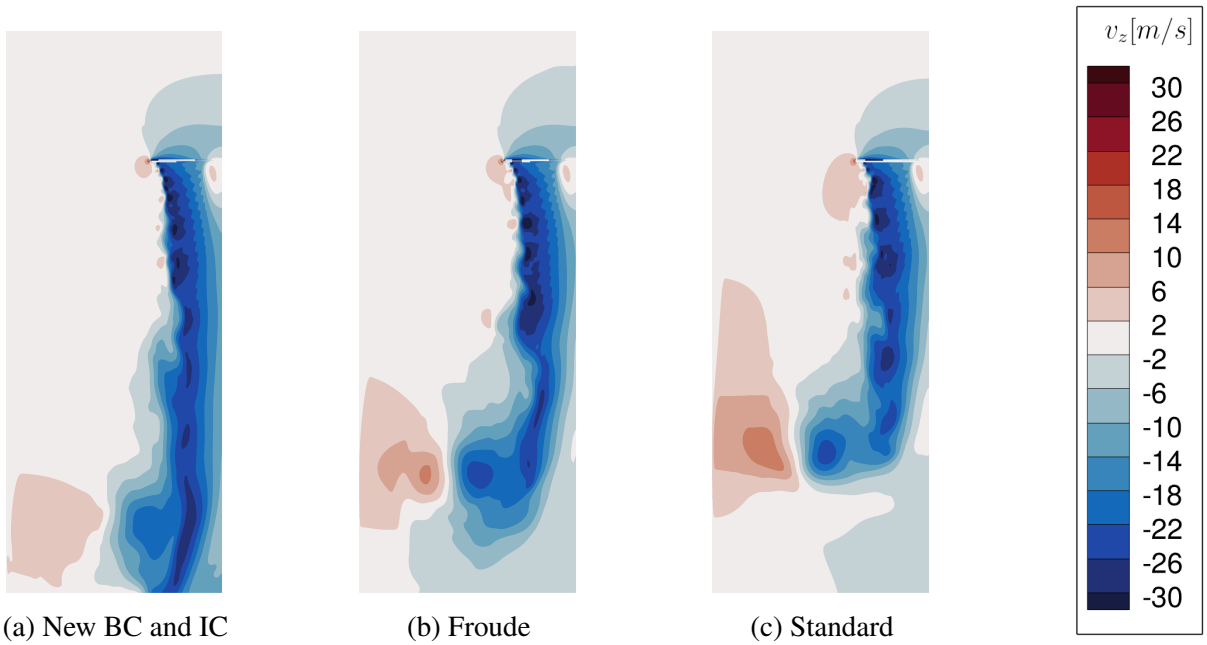

(a) New BC and IC (b) Froude (c) Standard

Figure 38: Axial velocity contour plots after 20 revolutions in C1 6R domain

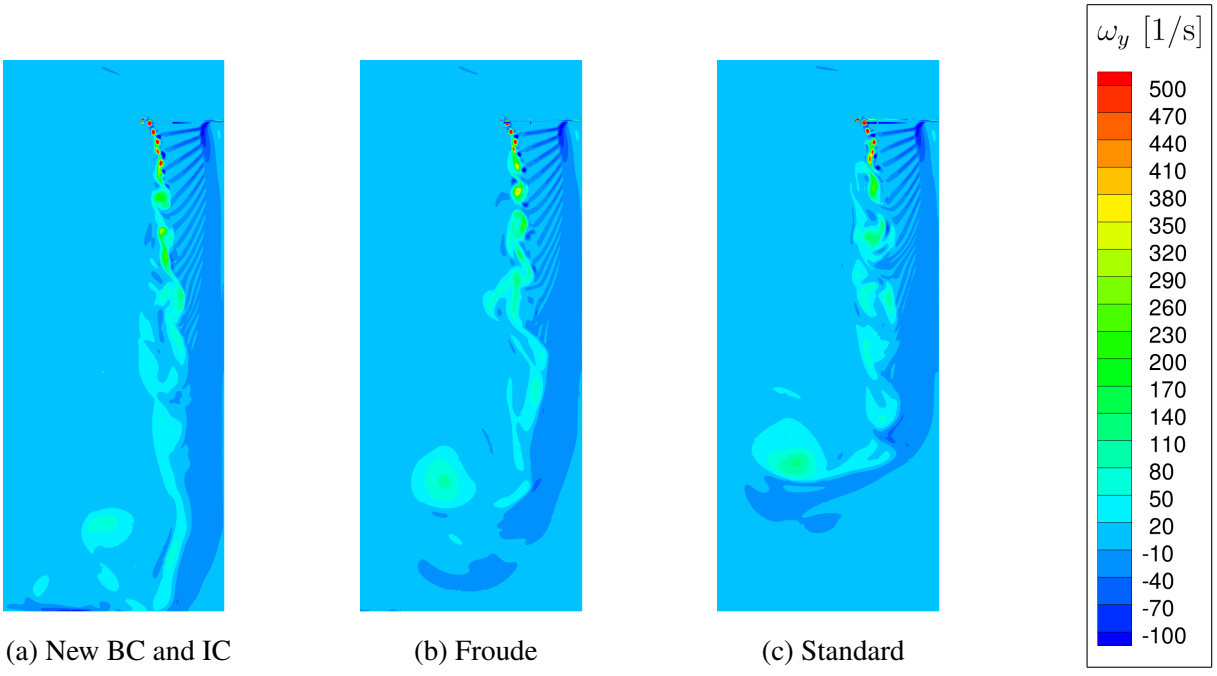

(a) New BC and IC (b) Froude (c) Standard

Figure 39: Y-vorticity contour plots after 20 revolutions in C1 6R domain

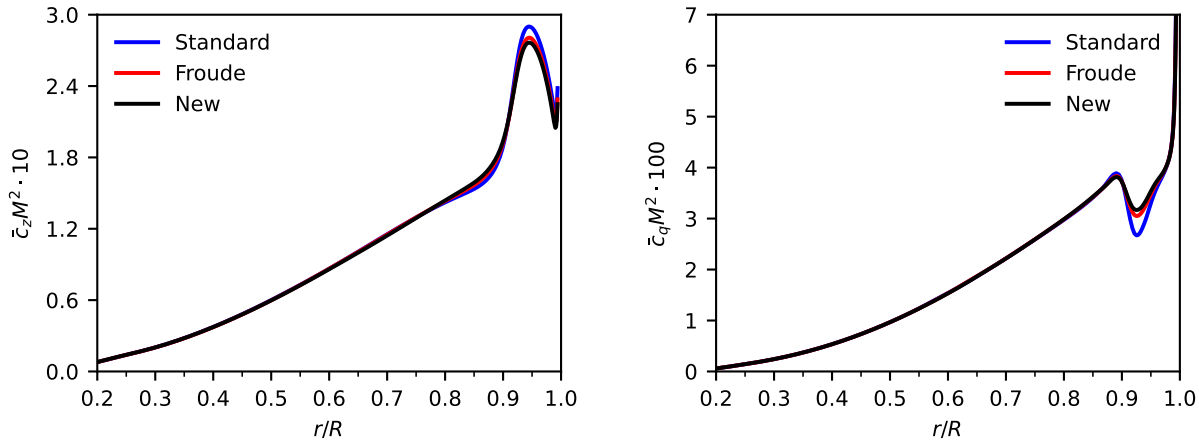

(a) Lift

(b) Torque

Figure 40: Lift and Torque distribution with C1 6R domain for three BCs at 20 Revolutions

4.3.3 Discoveries using the monocoque 25R domain

In this final chapter, the results from the larger monocoque domain (M2 25R) are analysed. The simulations described here are in reference to test cases 12 to 14 in the test matrix (Table 3), where the three BC's are investigated. Froude and Standard BC tests initialised with quiescent flow, and the New Model BC test with it's own IC similarly to the shorter monocoque domain (M2 6R) tests described in the previous chapter. An important remark about these tests is the amount of revolutions they were simulated for. As will be seen in the following plots, the tests were run for more than 2500 revolutions. This has not been found recorded in any CFD literature regarding helicopter rotors. To elaborate as to why this was done, two key points are noted. Firstly, in any wind tunnel study, it is common practice to allow a rotor spin for a minimum of at least 100 revolutions before measuring any forces or moments [4]. In fact, DLR's wind tunnel experimentation practice for the HART II rotor which spins at 1041RPM is to allow the rotor to spin 60 seconds before taking measurements. By allowing these simulations to run for over 1000 revolutions, a more accurate representation of a wind tunnel simulation may be observed. Secondly, as will be seen in the initial FM plot up to 200 revolutions, Figure 41b, there is a noticeable drift in the values of all tests. This was also commented upon by senior research scientist, Chaderjian [4], in his recent 2023 publication regrading CFD simulations of a rotor in hover with a strong emphasis on the lessons learned over the last decade of his research endeavours. As such, the study aims to witness for how long these values drift, and if not, how they evolve in time.

As noted in the introduction of this chapter, the initial evolutionary plots of theFM (Figure 41b) and of the CT (Figure 42b) seem to level off with only slight drifts in their values after approximately 100 revolutions. Although the values of FM for the three different BC tests are observed to be within close proximity of one another, an examination of the CT plots show that the New Model BC test is showing a lower CT compared to the rest of the BC tests. This means

that its coefficient of power is settling lower than the other two BC tests and hence providing an overall similar FM to the other tests. A look into the density residual plot and the sum of pseudo iterations plot in Figure 43, show that in fact the simulations on this domain are being tightly converged below 1E-06. Additionally after 30 revolutions, roughly when the initial chaotic starting vortex escapes the domain, the New Model BC is requiring a smaller number of total inner iterations to reach convergence hinting at more efficient performance.

Since there was still evident drift in these values at 200 revolutions, the simulations were continued and monitored beyond 2500 revolutions as seen in the coefficient plots. Unexpectedly, there is a continuation in the decrease of the FM with the same gradient of all plots up to roughly 1000 revolutions, where each BC test takes its own trend. At this point, the Standard BC test drops substantially before leveling out around 2000 revolutions with an FM of 0.43, a much lower value than that expected from the experimental interpolated data. Froude's BC test on the other hand continues with the initial downwards trend up until 1300 revolutions when it similarly drops at a fast rate before beginning to level off near the same value of the Standard BC's test. The New Model BC's test stays on the same initial downwards trend before leveling off and increasing slightly, and finally dropping with a steep gradient. Although flows seem to still be developing, at this point the New Model BC test is showing the best FM. To gain an insight as to why these value histories were varying so substantially, the transient flow fields were investigated and conclusions were drawn.

The axial velocity plots and the eddy viscosity plots of the three tests after 2500 revolutions can be seen in Figures 44 and 45. Through a time dependent animation up until this timestamp, all BC tests showed the blue axial velocity region indicating the downwash of the rotor shrinking, whilst the blue bubble of inflow above the rotor oscillating in shape and in strength. This phenomenon may be occurring due to recirculation within the domain due to all BC's not performing sufficiently as previously mentioned in other chapters, but an additional reason was hypothesized here. As seen in the axial velocity contour plots of Figure 44, it is clear that the velocities that are escaping at the bottom of the domain are very low, no more than roughly Mach 0.02. This flow velocity classifies it almost incompressible whilst the FLOWer CFD solver used is formulated for compressible flow. In particular, the numerical boundary condition used as standard practice in FLOWer is a compressible explicit upwind second-order scheme developed by Whitfield [24]. It is possible that this numerical boundary condition may be causing growing errors from the low mach numbers it is interacting with, which in turn can cause the flow field to develop in abstract ways.

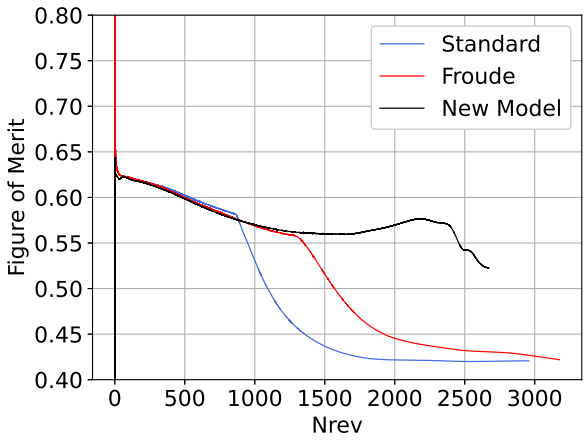

(a) Complete Figure of Merit Plot

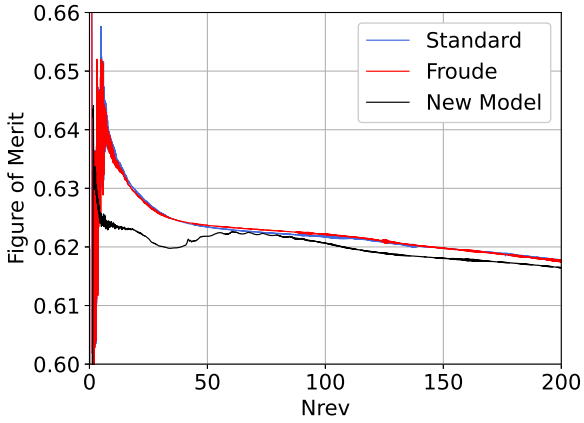

(b) Figure of Merit plot limited to 200 Rev

Figure 41: Figure of Merit plots with M2 25R domain for three BC tests

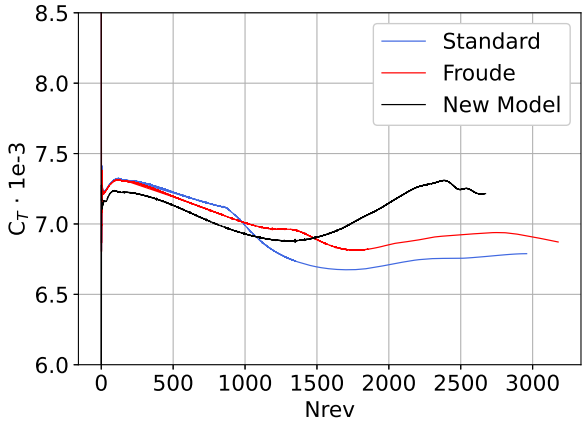

(a) Complete Coefficient of Thrust plot

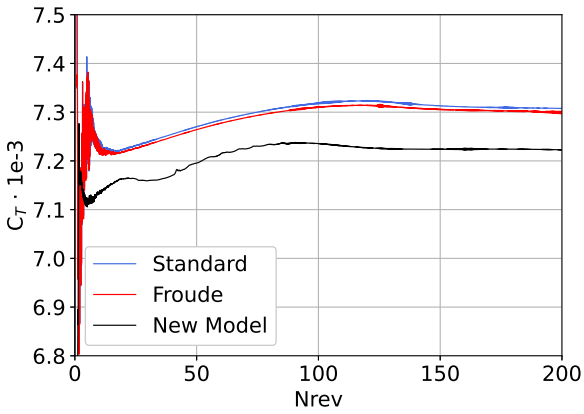

(b) Coefficient of Thrust plot limited to 200 Rev

Figure 42: Coefficient of Thrust plots with M2 25R domain for three BC tests

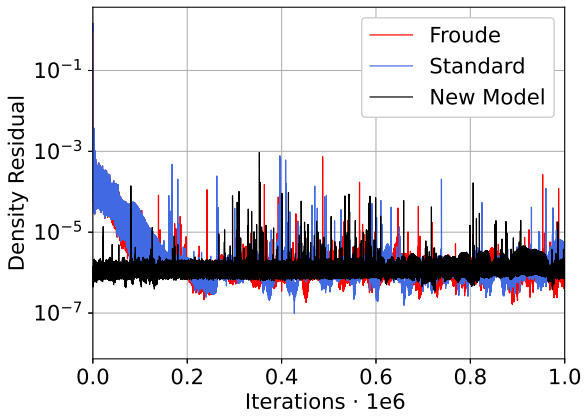

(a) Density Residual Plot

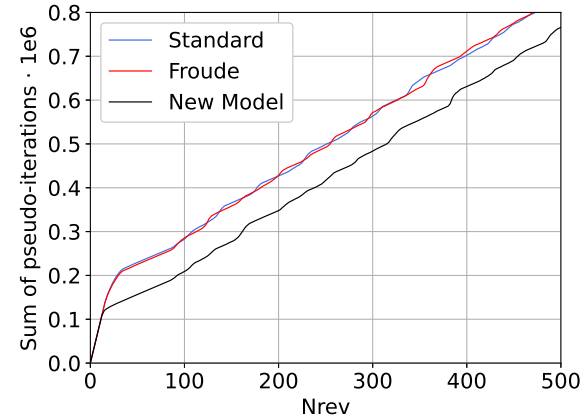

(b) Sum of pseudo-iterations vs revolutions

Figure 43: Results with M2 25R domain for three BC tests

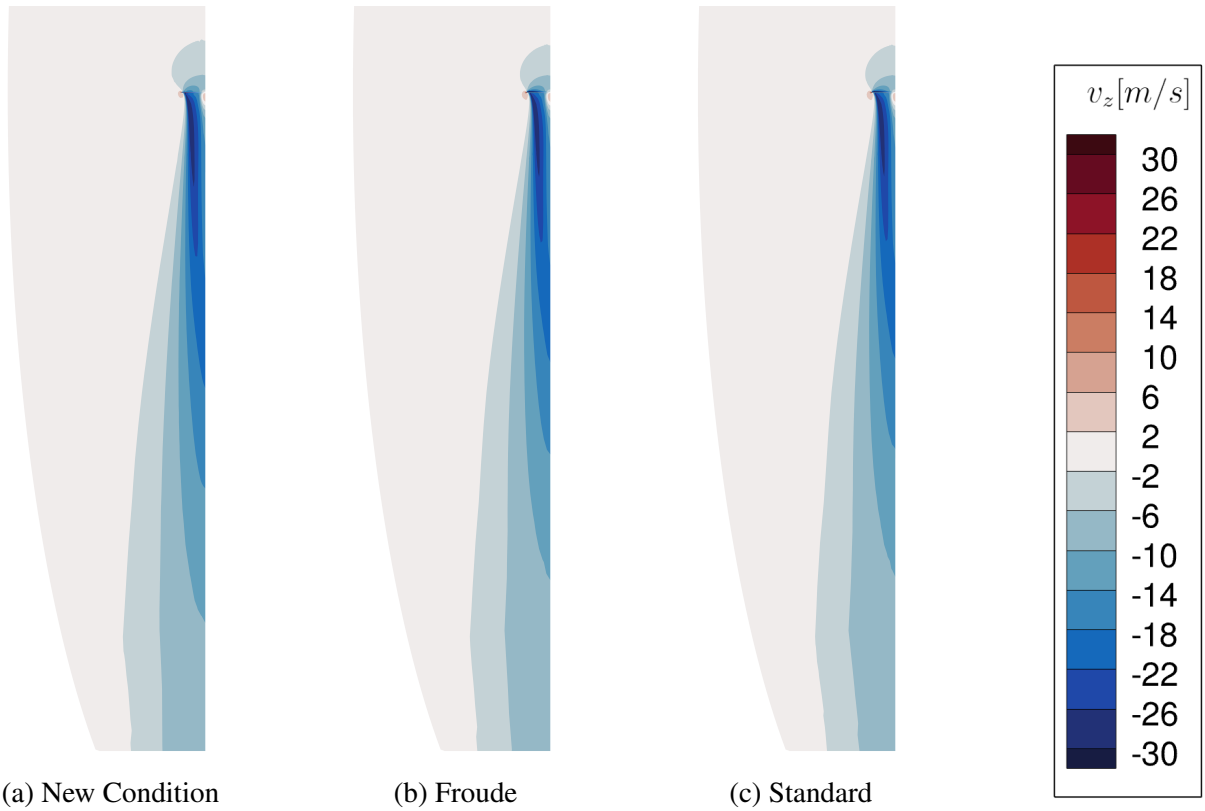

(a) New Condition (b) Froude (c) Standard

Figure 44: Axial velocity contour plots beyond 2500 revolutions in M2 25R domain

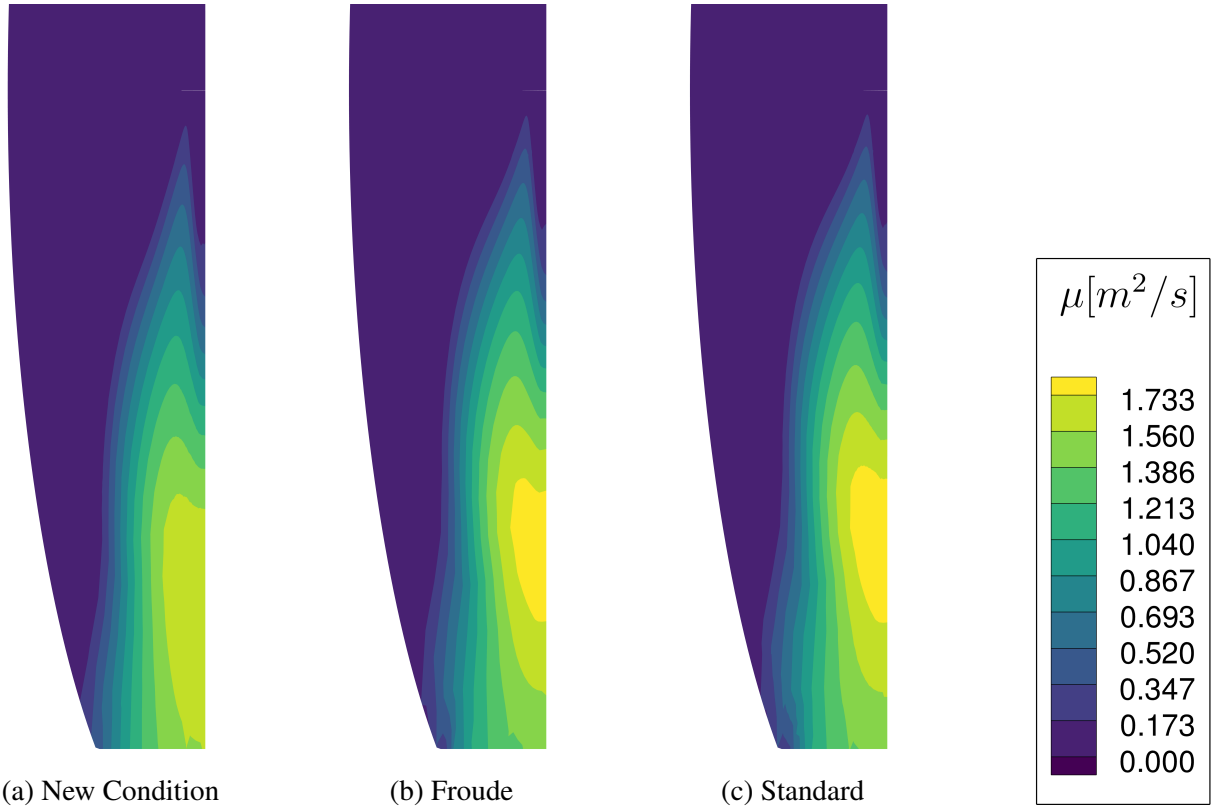

(a) New Condition (b) Froude (c) Standard

Figure 45: Eddy viscosity contour plots beyond 2500 revolutions in M2 25R domain

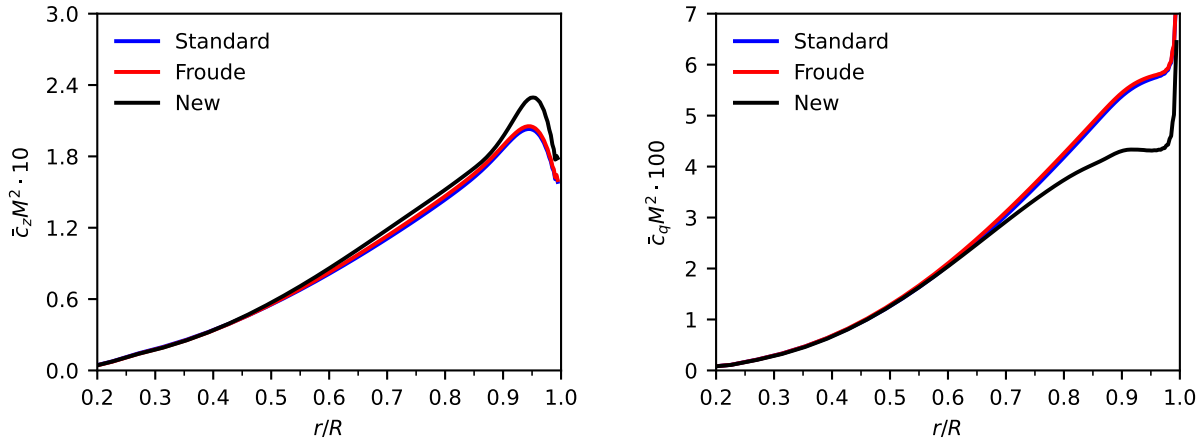

(a) Lift (b) Torque

Figure 46: Lift and Torque distribution with M2 25R domain for three BCs beyond 2500 revolutions

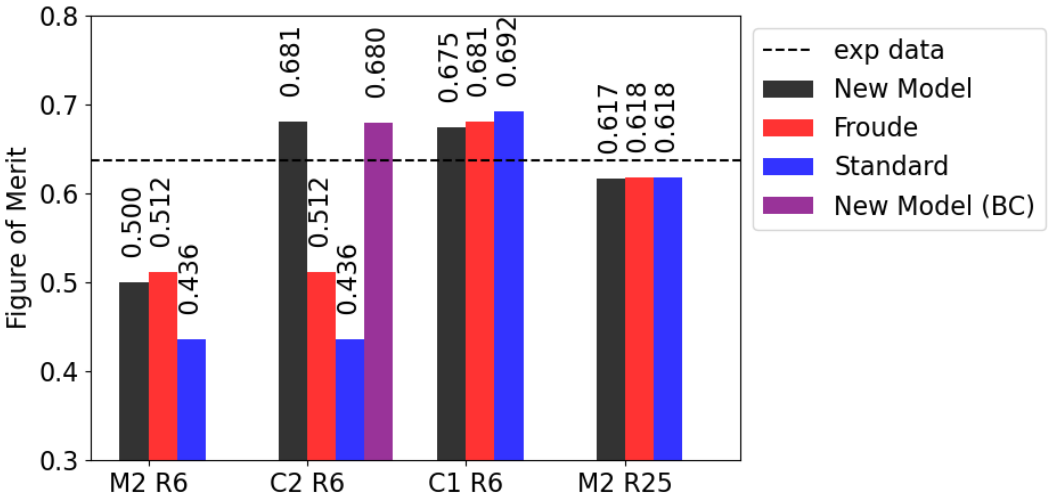

Figure 47: Figure of Merit comparison from different tests

5 Conclusions

An array of time-depended helicopter HART II rotor simulations seen in Table 3 have been carried out with the settings of Table 2 with the purpose of investigating the effect of varying far field and initial conditions in different stages of the evolutionary flow using DLR's block-structured FLOWer CFD solver. Justification of the rotor chosen and the solver settings used are presented in chapters 3.2, 3.4 accordingly. Side studies were also done to investigate the effect of the density residual tolerance convergence criteria as well as the effect of the turbulence model chosen. Both these parametric studies shed light into the compromises between accuracy and computational efficiency, paving the path for the boundary condition simulations that followed. From these two studies, a density residual convergence tolerance value of 1E-06, and the Spalart-Allmaras 1-equation turbulence model were chosen. These boundary condition investigations were executed on both chimera and monocoque domains with both coarser and finer meshes.

Key findings from the convergence criteria and turbulence model investigations summarised are presented in this paragraph. It was concluded that a density residual tolerance value of 1E-03 and 1E-04 do not suffice in accurate convergence of the developing flow field and the associated coefficients despite their computational efficiency, whilst tolerance values of 1E-06 and 1E-05 show much more stability and accuracy. Additionally, turbulence models employed can have substantial effects on the developing wakes of complex vortex-dominated helicopter flow fields. This is due to the vast amount of regions which have adverse pressure and velocity gradients of the vorticies that are trailing off and interacting with one another. Two equation models such as the SST-k ω are found to be much more computationally demanding although preserve flow fields more accurately and tweaks of the Spalart-Allmaras 1-equation turbulence model's constants also may provide a more accurate representation of a helicopter rotor's physical flow field. Lastly, there is evidence that higher mesh quality and mesh resolution can give better results using turbulence models which were observed to give worse results on coarser meshes.

With the focal point of this investigation being the boundary and initial conditions employed on the computational domains, the key goals which were aimed for are summarised in this paragraph. Recent published literature describe new ways to prescribe the far field boundary conditions on CFD domains for helicopter rotors particularly in hover, which are different than the more traditional Froude source sink and standard quiescent flow conditions. Ideas vary from truncated vortex tubes of finite length to models based on empirical jet functions which all aim to create an approximation of the physical flow field. This is done in order to potentially bring the far field boundaries closer to the source of disturbance, i.e. the rotating rotor blade. By doing so, the overall computational domain can shrink and the flow field would be solved on a much smaller domain increasing computational efficiency and therefore taking less time to solve these complex flow fields. The initial conditions described also have the same goal in mind to reach

the hovering flow field at a faster rate, reducing the effect of the initial chaotic starting vortex which is seen when initializing with quiescent flow. As such, DLR wanted to implement and test these models against their implemented models on their block-structured FLOWer CFD solver.

Post-implementation of the Jia's modified Spalart model based on the empirical jet function in the FORTRAN FLOWer source code, simulations were run on different domains of varying mesh density, type, and most importantly downstream far field boundary location. The details of the different meshes used can be found in Table 1. It was found that the boundary condition had a substantial effect on the development of the flow field, with Jia's model providing more robust performance with the shorter 6 radii downstream boundary location domains. Additionally, transient flow field analysis and coefficient histories suggested that Jia's model as a boundary condition and as an initial condition aids in expelling the initial starting vortex out of the domain at a faster rate compared to the other boundary condition tests. Jia's model simply as a boundary condition, shows similar flow field evolution with the Froude boundary condition. Finer chimera mesh studies showed similar results in more detail, both alluding that the new model is requiring less inner-iterations and therefore computational costs to reach a similar flow field to the Froude boundary condition test. The bar chart in Figure 47 compares the Figure of Merit of all boundary conditions tests on all the computational domains considered against the experimental expected value. From this data, it is evident that the new model proposed by Jia is providing the most robustness when tested on all computational domains

A study that opened doors to more investigations was when the boundary conditions were tested on a larger domain and allowed to simulate beyond 2500 revolutions which has not been recorded in any recent CFD literature. It was found that beyond the 200 revolution mark where coefficients have a slight drift to their values, they begin to take their own trends for different boundary condition tests. A look into the flow fields show evidence of recirculation and a sense of instability. Another hypothesis of this phenomenon was the Whitfield numerical boundary condition is not able to deal with the low Mach number flows it is interacting with, and as such errors begin to radiate into the domain. A similar study to this one, where the numerical boundary condition is investigated rather than the physical may be important to understand the phenomena observed.

In broader context, this study has aimed to expedite CFD solution times and reduce computational costs by exploiting boundary condition models recorded in recent literature. It was found that the new model saves 0.8E+05 inner iterations to reach the same state of the other models (for example see Figure 37b). By proving robustness of Jia's model the German Aerospace Center (DLR) can now employ the boundary condition in their simulations of helicopter rotors in hover, a particularly computationally demanding task, enabling them to produce results faster and more reliably. However, the boundary condition can be further tested on more domains of varying characteristics to further reassure this statement.

A Appendix

A.1 Section 4.2 complimentary plots

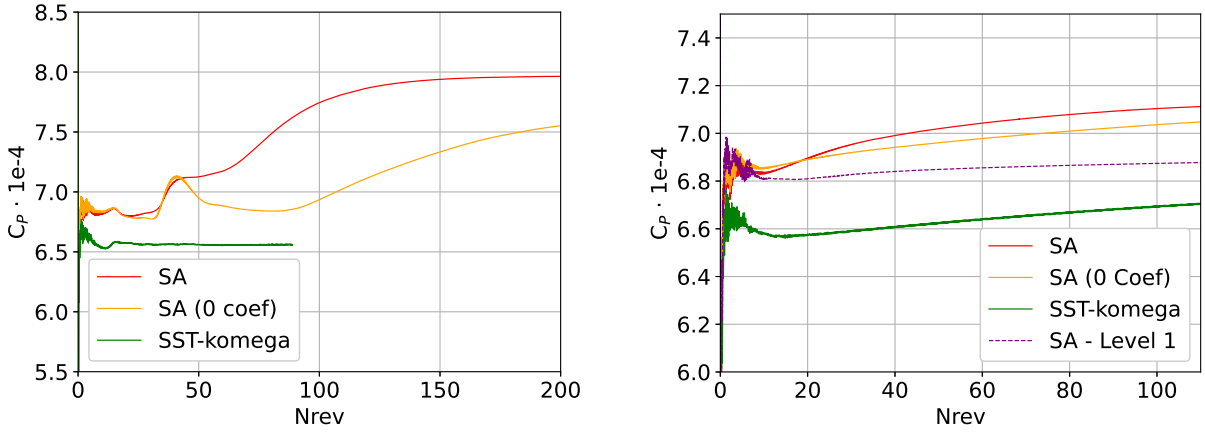

(a) 6R domain

(b) 25R domain

Figure 48: Coefficient of power against number of revolutions for different turbulence models

A.2 Section 4.3.1 complimentary plots

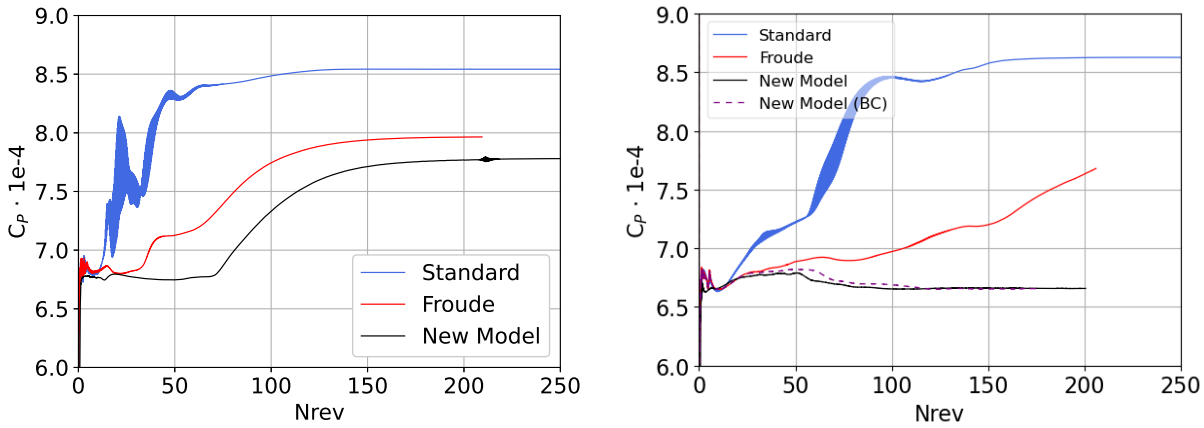

(a) Monocoque

(b) Chimera

Figure 49: Coefficient of power against number of revolutions for three BC tests in 6R domains

A.3 Section 4.3.2 complimentary plots

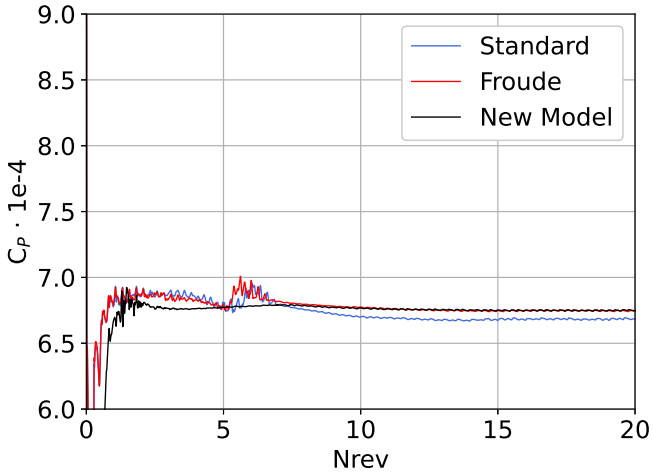

Figure 50: Coefficient of Power for C1 R6 domain

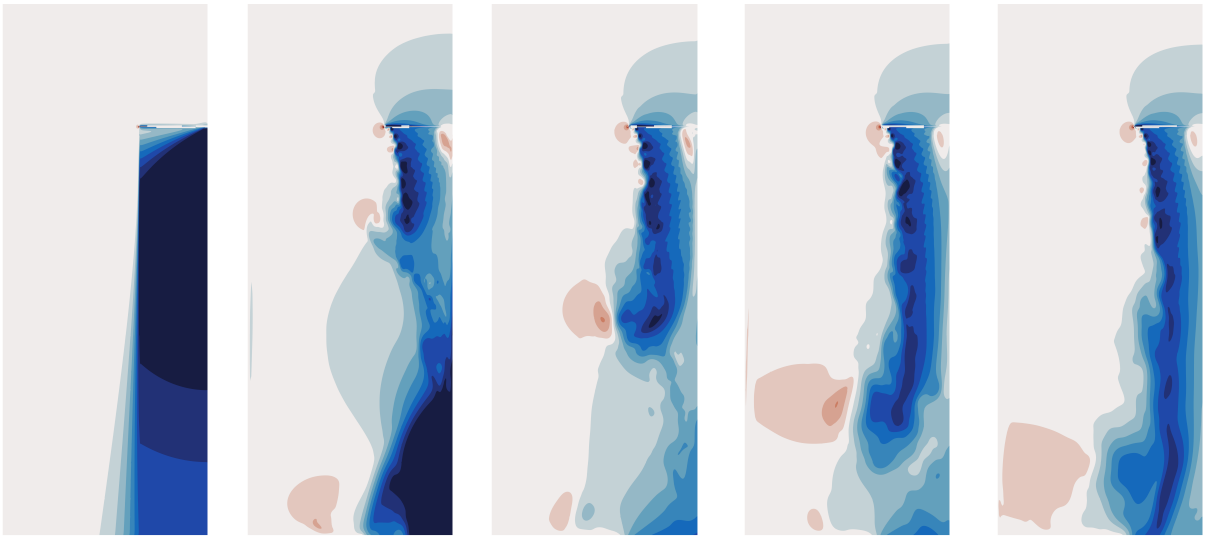

Figure 51: Axial velocity evolution in C1 6R domain with New Model BC and IC at every 5 revolutions from initialization

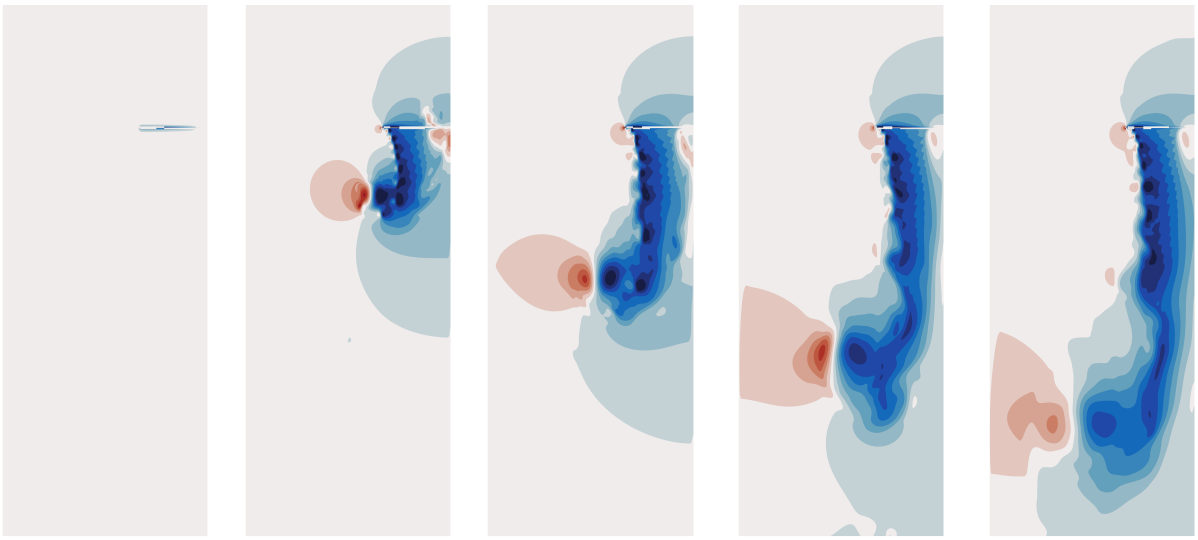

Figure 52: Axial veolicty evolution in C1 6R domain with Froude BC at every 5 revolutions from initialization

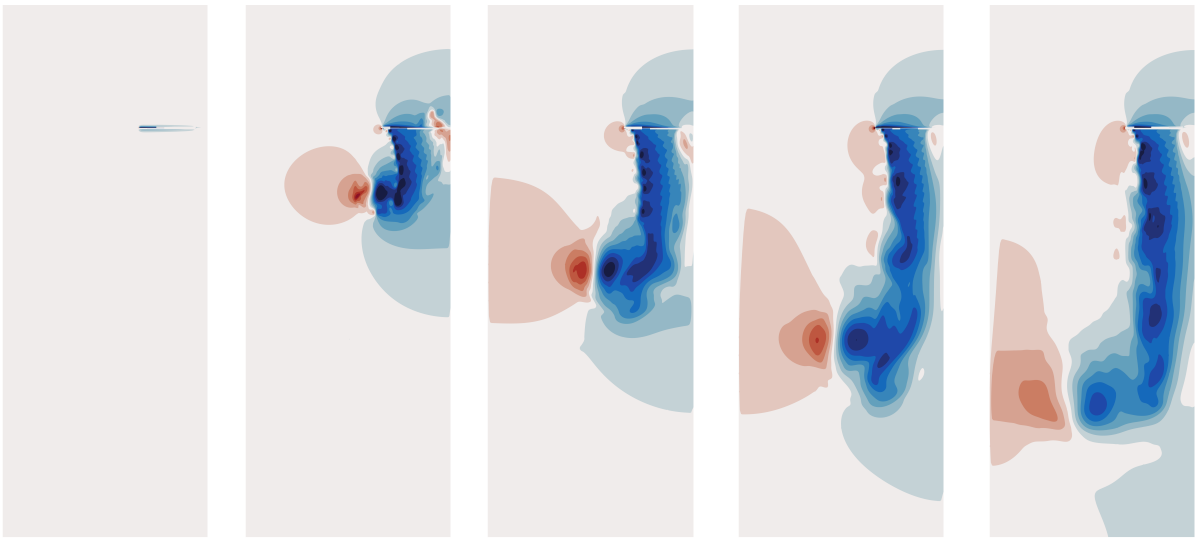

Figure 53: Axial velocity evolution in C1 6R domain with Standard BC at every 5 revolutions from initialization

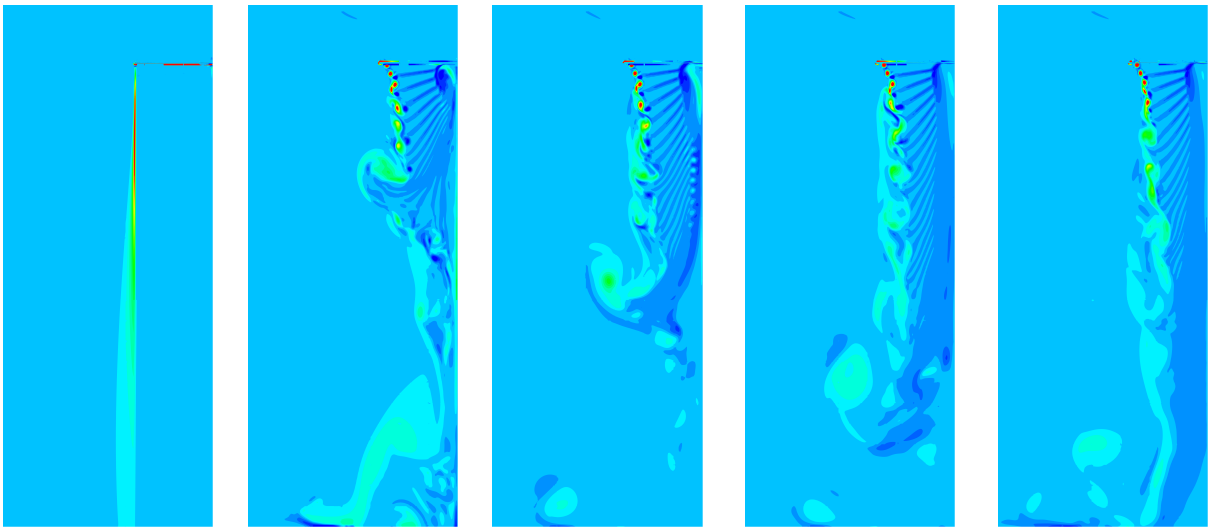

Figure 54: Y-vorticity evolution in C1 6R domain with New Model BC and IC at every 5 revolutions from initialization

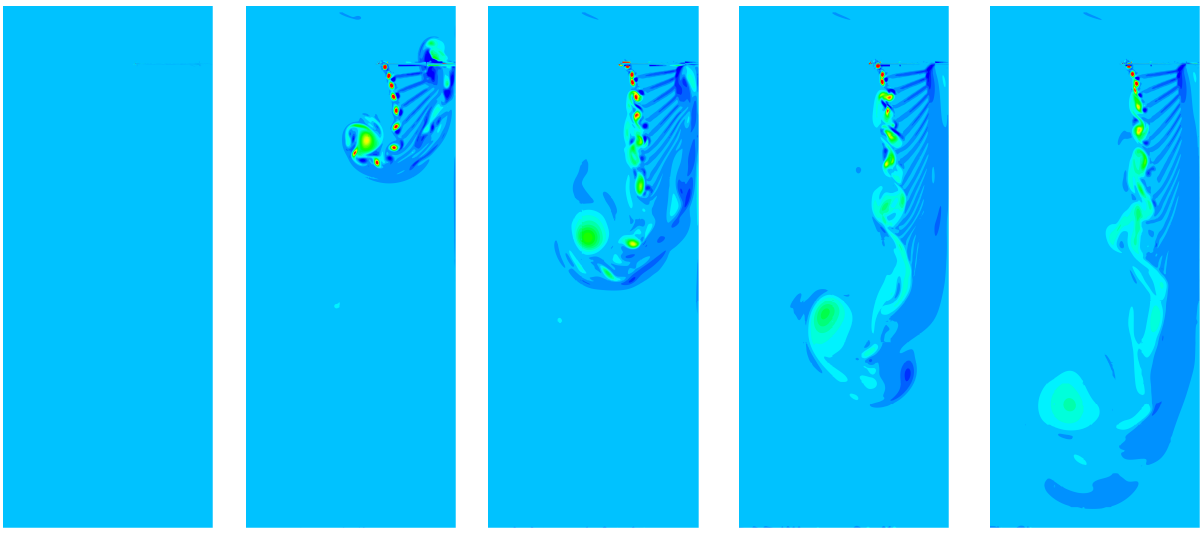

Figure 55: Y-vorticity evolution in C1 6R domain with Froude BC at every 5 revolutions from initialization

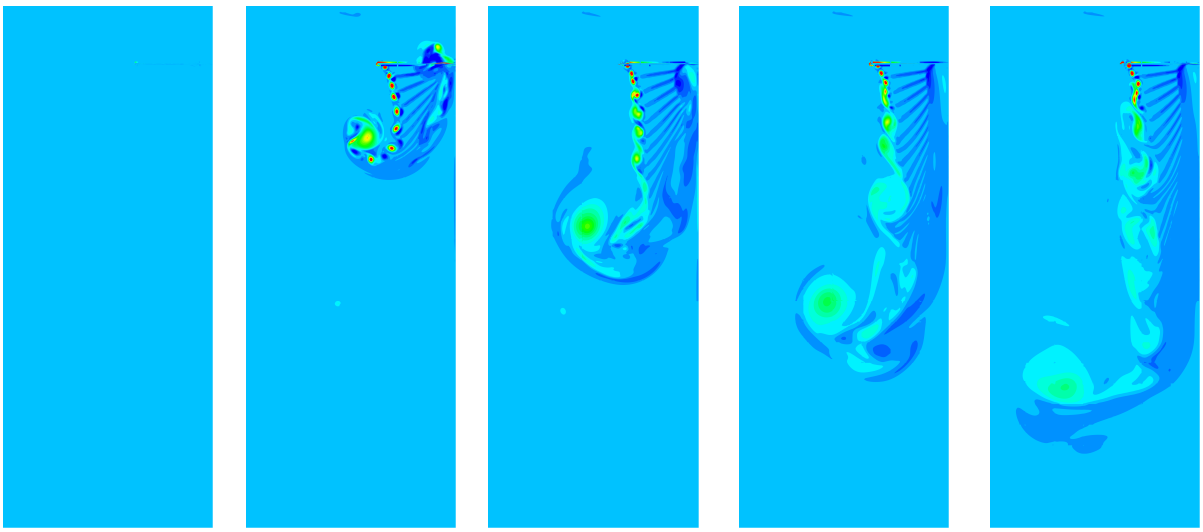

Figure 56: Y-vorticity evolution in C1 6R domain with Standard BC at every 5 revolutions from initialization

A.4 Section 4.3.3 complimentary plots

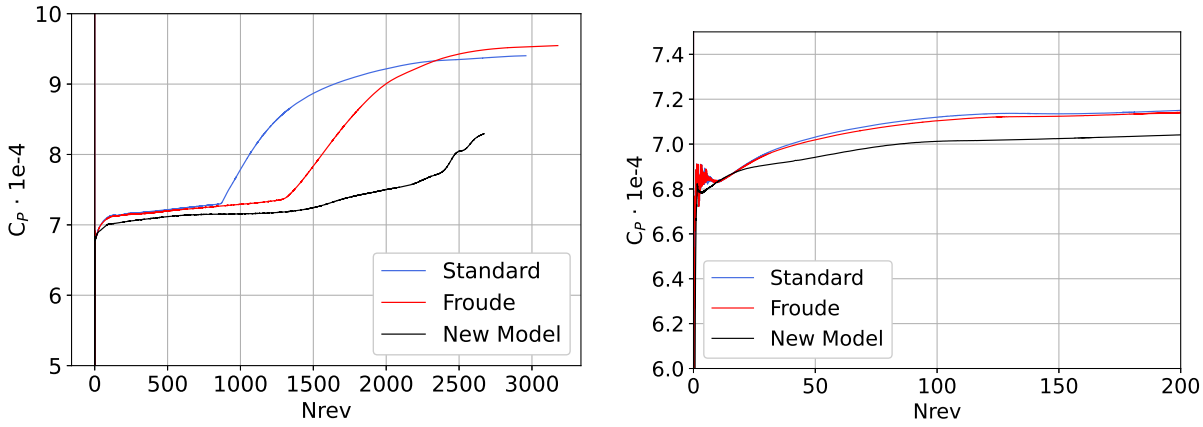

(a) Complete Coefficient of Power plot

(b) Coefficient of Power zoomed to 200 Rev

Figure 57: Results with M2 25R domain for three BC tests

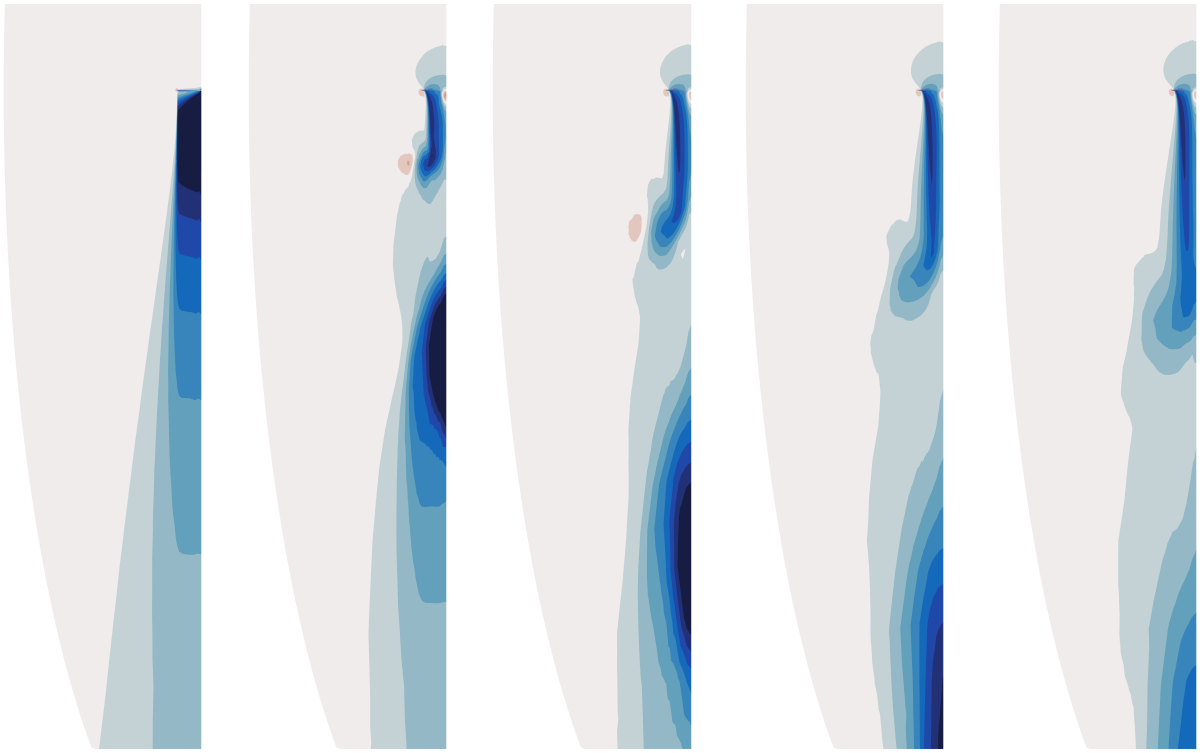

Figure 58: Axial velocity evolution in M2 25R domain with New Model BC and IC at every 10 revolutions from initialization

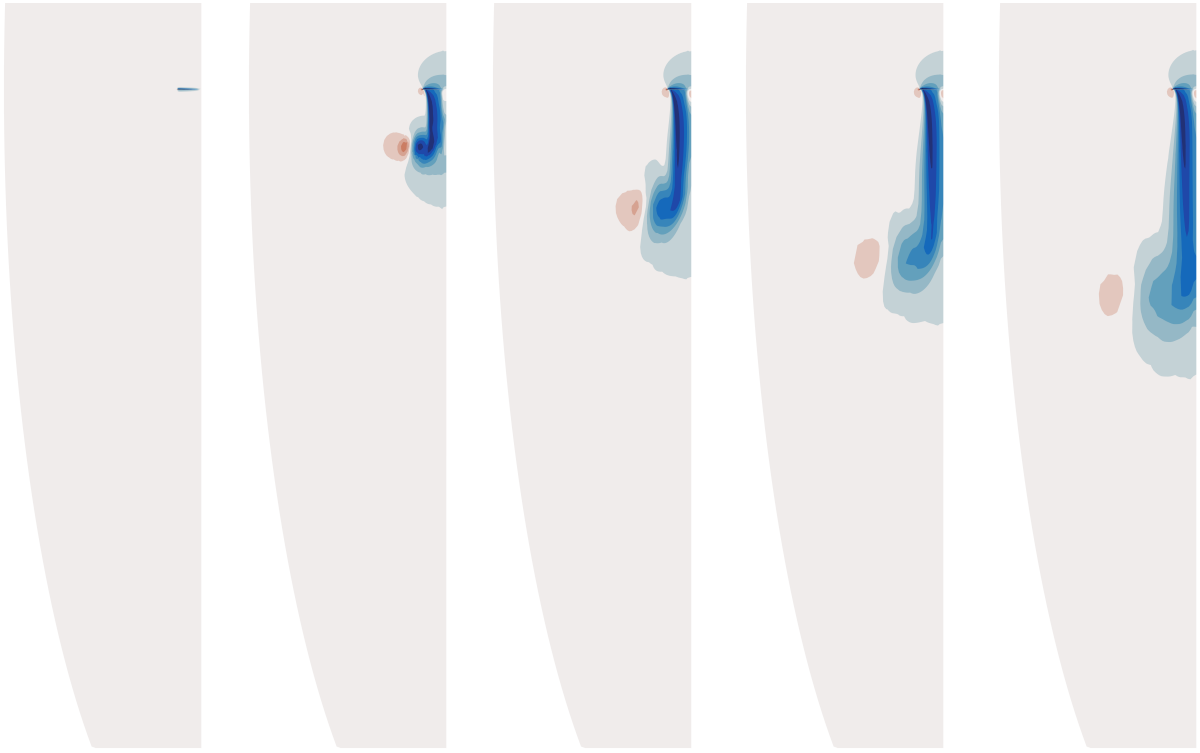

Figure 59: Axial velocity evolution in M2 25R domain with Froude BC at every 10 revolutions from initialization

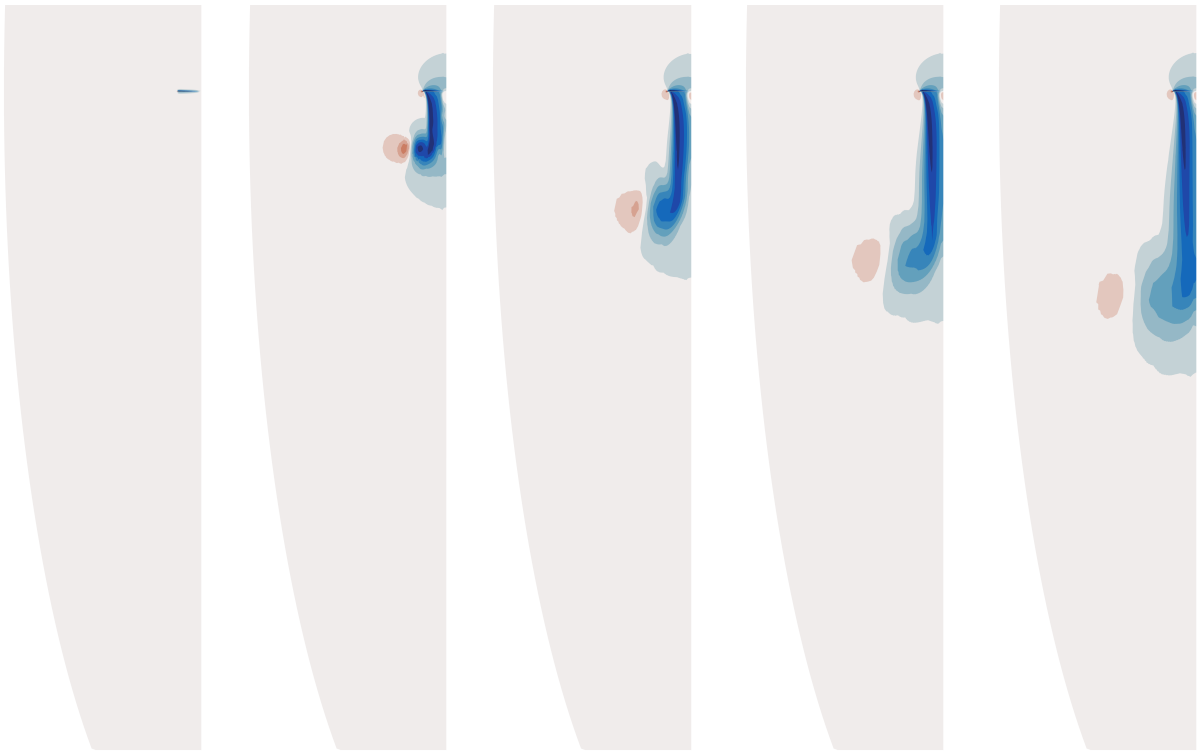

Figure 60: Axial velocity evolution in M2 25R domain with Standard BC at every 10 revolutions from initialization

A.5 Adjustment of Jia's modified equations of the Spalart model

The DLR's CFD solver, FLOWer which was employed for this research, works entirely with non-dimensional parameters. As such, the equations presented in Jia's work need to be adjusted before implemented into the source code of the CFD solver. Presented below is the procedure of non-dimensionalizing the equations for the tangential and spherical velocities which are then translated into a Cartesian coordinate system. Both equations here for the tangential and spherical velocities contain the same parameters and constants which are then multiplied by their according term in square brackets. the only difference between the terms outside the brackets between the two velocities is the negative sign:

$$u_r = -\frac{A_c}{r_m}\sqrt{\frac{T}{\rho}}\left[f_m(\theta_m) + \tan\left(\frac{\theta_m}{2}\right)\left.\frac{\mathrm{d}\theta_m}{\mathrm{d}\theta}\right|_{\theta_m}\right] \tag{20}$$

$$u_\theta = \frac{A}{r_m}\sqrt{\frac{T}{\rho}}\left[\tan\left(\frac{\theta_m}{2}\right) f_m(\theta_m)\right] \tag{21}$$

It is evident from **Jia's paper** that the constant A_c is dimensionless. The value of r_m is dimensional with the SI units of meters. Thrust, T, is dimensional with the SI units of Newtons, and density, ρ, is dimensional with SI units of kg/m^3. The square bracket parts of both equations return a non-dimensional value. As such, by using SI units in these equations, the values of velocities result in SI units as well of m/s. Remembering that the coefficient of thrust is:

$$C_T = \frac{T}{\rho\,\pi\,R_{tip}^2\,V_{tip}^2}$$

Re-arranged for thrust, it can be substituted into the equations. For sake of keeping things concise, the non-dimensionalisation of just one of the two components of velocities is shown. This is acceptable as the terms that determine their units are outside of their square brackets. These terms for both equations are the same. Substituting thrust into the equation for u_r and canceling appropriately:

$$u_r = \frac{-A_c}{r_m}\sqrt{\frac{T}{\rho}}[...] = \frac{-A_c}{r_m}\sqrt{\frac{C_T\,\rho\,\pi\,R_{tip}^2\,V_{tip}^2}{\rho}}[...] = \frac{-A_c}{r_m}\sqrt{C_T\,\pi\,R_{tip}^2\,V_{tip}^2}[...]$$

Then, remembering the equation for the Mach number:

$$M_{tip} = \frac{V_{tip}}{\alpha} = \frac{V_{tip}}{\sqrt{\gamma RT}}$$

Rearranging for V_{tip} and substituted into the equation:

$$u_r = \frac{-A_c}{r_m}\sqrt{C_T\,\pi\,R_{tip}^2 M_{tip}^2 \gamma RT}\,[...] = \frac{-A_c}{r_m} R_{tip}\,M_{tip}\sqrt{C_T\,\pi\,\gamma RT}\,[...]$$

And finally, dividing the velocity by $\sqrt{RT}$ the equation arrives at its non-dimensional state:

$$\hat{u}_r = \frac{u_r}{\sqrt{RT}} = \frac{-A_c}{r_m} R_{tip}\,M_{tip}\frac{\sqrt{C_T\,\pi\,\gamma RT}}{\sqrt{RT}}\,[...] = \frac{-A_c}{r_m} R_{tip}\,M_{tip}\sqrt{C_T\,\pi\,\gamma}\,[...]$$

All FLOWer CFD solver velocities are non-dimensionilized with the factor $\sqrt{RT}$, and in a similar way, this derivation arrives to a non-dimensional form of the original equations that have been implemented into the FLOWer source code.

References

[1] S. Y. et. al. "An efficient CFD approach for simulating unsteady hypersonic shock–shock interference flows". In: *Computers and Fluids* 27.5 (1998), pp. 571–580. ISSN: 0045-7930. DOI: https://doi.org/10.1016/S0045-7930(97)00061-3.

[2] M. Athadkar and S. Desai. "Importance Of The Extent Of Far-Field Boundaries And Of The Grid Topology In The CFD Simulation Of External Flows". In: *International Journal of Mechanical And Production Engineering, ISSN: 2320-2092* (Sept. 2014).

[3] P. Beaumier, E. Chelli, and K. Pahlke. "Navier-Stokes Prediction of Helicopter Rotor Performance Including Aero-Elastic Effects". In: *56th AHS Forum* (Jan. 2000).

[4] N. M. Chaderjian. "A Quantitative Approach for the Accurate CFD Simulation of Hover in Turbulent Flow". In: *Journal of the American Helicopter Society* 68.4 (2023), pp. 42009–42028. ISSN: 2161-6027. DOI: doi:10.4050/JAHS.68.042009.

[5] W. Choi, S. Lee, J. Jung, et al. "New FarField Boundary and Initial Conditions for Computation of Rotors in Vertical Flight Using Vortex Tube Model". In: *Journal of the American Helicopter Society* 53.4 (2008), pp. 382–397. ISSN: 2161-6027.

[6] J. Dacles-Mariani, J. Dacles-Mariani, D. Kwak, et al. "On numerical errors and turbulence modeling in tip vortex flow prediction". In: *International Journal for Numerical Methods in Fluids* 30 (1999), pp. 65–82.

[7] J. Dacles-Mariani, G. G. Zilliac, J. S. Chow, et al. "Numerical/experimental study of a wingtip vortex in the near field". In: *AIAA Journal* 33.9 (1995), pp. 1561–1568. DOI: 10.2514/3.12826.

[8] DLR. "Computer for Advanced Research in Aerospace (CARA)". In: *German Aerospace Center Website* (). eprint: https://www.dlr.de/en/research-and-transfer/research-infrastructure/hpc-cluster/cara.

[9] R. Froude. "On the part played in propulsion by differences of fluid pressure". In: *13th Session of the Institution of Naval Architects* 30 (1889), pp. 390–405.

[10] F. Jia, Q. Wang, and P. Spalart. "Improved Initial and Boundary Conditions for Hovering Rotor CFD Simulations". In: *Vertical Flight Society's 78th Annual Forum* (June 2022). DOI: 10.4050/F-0078-2022-17474.

[11] K. Kitamura and E. Shima. "Towards shock-stable and accurate hypersonic heating computations: A new pressure flux for AUSM-family schemes". In: *Journal of Computational Physics* 245 (2013), pp. 62–83. ISSN: 0021-9991. DOI: https://doi.org/10.1016/j.jcp.2013.02.046.

[12] F. Menter, M. Kuntz, and R. Langtry. "Ten years of industrial experience with the SST turbulence model". In: *Heat and Mass Transfer* 4 (Jan. 2003).

[13] F. J. Perry, W. Y. F. Chan, I. A. Simons, et al. “Modeling the Mean Flow Through a Rotor in Axial Flight Including Vortex Ring Conditions”. In: *Journal of the American Helicopter Society, Volume 52, Number 3, 1 July 2007, pp. 224-238(15)* (2007).

[14] J. Raddatz and J. Fassbender. “Block Structured Navier-Stokes Solver FLOWer”. In: Notes on Numerical Fluid Mechanics and Multidisciplinary Design (NNFM) 89 (2005). Ed. by N. Kroll and J. Fassbender, pp. 27–44.

[15] E. Shima and K. Kitamura. “On New Simple Low-Dissipation Scheme of AUSM-Family for All Speeds”. In: *47th AIAA Aerospace Sciences Meeting including The New Horizons Forum and Aerospace Exposition* (). DOI: 10.2514/6.2009-136. eprint: https://arc.aiaa.org/doi/pdf/10.2514/6.2009-136.

[16] M. Smith, J. Lim, B. Wall, et al. “An assessment of CFD/CSD prediction state-of-the-art using the HART II International Workshop data”. In: *Annual Forum Proceedings - AHS International* 1 (May 2012), pp. 1–41.

[17] P. Spalart. “On the simple actuator disk”. In: *Journal of Fluid Mechanics* 494 (2003), pp. 399–405. DOI: 10.1017/S0022112003006128.

[18] P. Spalart and S. Allmaras. “A One-Equation Turbulence Model for Aerodynamic Flows”. In: *AIAA* 439 (Jan. 1992). DOI: 10.2514/6.1992-439.

[19] P. R. Spalart. “On the flow field induced by a hovering rotor or a static jet”. In: *Journal of Fluid Mechanics* 701 (2012), pp. 473–481. DOI: 10.1017/jfm.2012.188.

[20] G. Srinivasan. “A Free-Wake Euler and Navier-Stokes CFD Method and Its Application to Helicopter Rotors Including Dynamic Stall”. In: *Associates, Inc. Technical Report 93-01* (1993).

[21] R. W. Stewart. “Irrotational motion associated with free turbulent flows”. In: *Journal of Fluid Mechanics* 1.6 (1956), pp. 593–606. DOI: 10.1017/S0022112056000391.

[22] P. K. Sweby. “High Resolution Schemes Using Flux Limiters for Hyperbolic Conservation Laws”. In: *SIAM J. Numer. Anal.* 21.5 (Oct. 1984), pp. 995–1011. ISSN: 0036-1429. DOI: 10.1137/0721062.

[23] S.-C. Wang. “Analytical Approach to the Induced Flow of a Helicopter Rotor in Vertical Descent”. In: *Journal of the American Helicopter Society, Volume 35, Number 1, 1 January 1990, pp. 92-98(7)* (1990).

[24] D. Whitfield and J. Janus. “Three-dimensional unsteady Euler equations solution using flux vector splitting”. In: *AIAA Paper* 84 (1984).

[25] G. Wilke. “Comparisons of Different Spatial Schemes and Limiters for Helicopter Flows”. In: *New Results in Numerical and Experimental Fluid Mechanics XIII* (July 2021), pp. 418–427. DOI: 10.1007/978-3-030-79561-0_40.

[26] G. Wilke. “Quieter and Greener rotorcraft: concurrent aerodynamic and acoustic optimization”. In: *CEAS Aeronautical Journal* 12 (Apr. 2021). DOI: 10.1007/s13272-021-00513-x.

[27] G. Wilke, H. Sugawara, Y. Tanabe, et al. “Investigations of a boxed rotor: The STAR II rotor in DLR’s test hall”. In: *49th European Rotorcraft Forum (ERF)* (Sept. 2023).

[28] S. YOON, L. CHANG, and D. KWAK. “LU-SGS implicit algorithm for three-dimensional incompressible Navier-Stokes equations with source term”. In: *9th Computational Fluid Dynamics Conference*. DOI: 10.2514/6.1989-1964.

[29] D.-M. Zimmermann, R. Mayer, T. Lutz, et al. “Impact of Model Parameters of SALSA Turbulence Model on Transonic Buffet Prediction”. In: *AIAA Journal* 56 (Dec. 2017), pp. 1–4. DOI: 10.2514/1.J056193.